ABSTRACT

Title of dissertation: NOVEL PRECISION MEASUREMENT METHODS FOR PROBING DARK MATTER

Reza Ebadi, Doctor of Philosophy, 2025

Dissertation directed by: Professor Ronald L. Walsworth
Department of Physics

The nature of dark matter (DM) remains one of the most profound open questions in fundamental physics. In this thesis, we develop and apply novel precision measurement techniques to probe DM across a broad range of candidate masses and interaction strengths. For weakly interacting massive particle (WIMP) DM, we present a new directional detection scheme based on solid-state quantum sensing in diamond. For ultralight bosonic DM, we introduce a novel experimental concept–GALILEO–which employs electro-optics and resonant interferometry to search for DM–induced oscillating electric fields. To probe ultra-heavy DM, we develop a geological detection method that maps extended damage tracks in ancient quartz using electron microscopy, leveraging billion-year exposure times for enhanced sensitivity. Finally, we analyze gravitational wave signals from double white dwarf binaries, treating them as a distributed array of galactic accelerometers capable of dynamically measuring the Milky Way's gravitational potential. Together, these complementary approaches demonstrate the potential of precision measurement science to expand the search for DM. They highlight the powerful interplay between quantum technologies, materials science, and astrophysics in tackling some of the most fundamental mysteries of the universe.

NOVEL PRECISION MEASUREMENT METHODS FOR PROBING DARK MATTER

by

Reza Ebadi

Dissertation submitted to the Faculty of the Graduate School of the
University of Maryland, College Park in partial fulfillment
of the requirements for the degree of
Doctor of Philosophy
2025

Advisory Committee:
Professor Ronald L. Walsworth, Chair/Advisor
Professor Raman Sundrum
Professor Alexey V. Gorshkov
Professor Peter Shawhan
Professor John Cumings

Dedication

To my beloved family, miles apart yet ever present in my journey.

Acknowledgments

It was the spring of 2020, during my first year of graduate school, when I reached out to Ron to join his group. Looking back, that was the single most important decision I made in my early graduate school–one that filled my time here with purpose, joy, and fulfillment, even amid the hard work and occasional frustrations that anyone who has gone through this journey knows well. To me, Ron exemplifies the ideal of a supportive, thoughtful, and inspiring mentor. From the very beginning, he encouraged me to do meaningful science and to follow my passion. He supported me in finding my own approach to research, trusted my academic independence, and connected me with an exceptional network of collaborators with whom I still work today. He was also understanding and kind when I needed time to recover from burnout in the final year of my PhD. Thank you, Ron—for everything mentioned here, and for all the rest that cannot be captured in a short paragraph.

There are other people whose impact on my academic growth, while perhaps different in kind, has been no less significant than Ron's. First and foremost, I want to thank Hassan Firouzjahi, my undergraduate research supervisor. It was under his guidance that I took my first real steps into research. He taught me how to think like a scientist at a young age, and thanks to him, I entered graduate school with a familiarity and confidence in doing research that most starting PhD students don't yet have. Throughout graduate school, I was also fortunate to learn from and be mentored by Surjeet Rajendran, Xingang Chen, David Phillips, Emanuele Berti, David Kaplan, and Lian-Tao Wang. Each of them has profoundly shaped my scientific approach, and their influence continues to ripple through my career. I consider them mentors as well, and I am deeply grateful for their time, insight, and inspiration.

I'm also grateful to my thesis committee—Raman Sundrum, Alexey Gorshkov, Peter Shawhan, and John Cumings—for generously agreeing to serve, and for their time, and

thoughtful feedback. I am also grateful for the efficient and exceptional administrative support of Josiland Chambers throughout graduate school. She consistently went above and beyond in assisting students. I would also like to extend my gratitude to members of the UMD EPT group–Kaustubh Agashe, Zackaria Chacko, Anson Hook, and Raman Sundrum–for their excellent teaching, encouragement, and the many insightful physics conversations over the years.

It would be impossible to name all my collaborators here, and I fear forgetting someone, so I will only try to highlight a few. I am especially grateful to my senior mentors in the Walsworth group—including, but not limited to, Aakash Ravi, Mason Marshall, Connor Hart, Matthew Turner, and Daniel Ang—who introduced me to the world of experimental physics with extraordinary patience. I'm also thankful for the opportunity to collaborate with colleagues from other institutions on theoretical projects, including (but again not limited to) Erwin Tanin, Soubhik Kumar, Jae Hyeok Chang, Vladimir Strokov, and Jerome Quintin. As I now move into a new chapter as a postdoctoral fellow, I'm excited about the new collaborations I've begun with incredible scientists such as Hari Ramani, Yikun Wang, Francesco Serra, Loris Del Grosso, and Abhishek Banerjee at Johns Hopkins University and the University of Delaware.

PhD life—far from home, family, and lifelong friends—is never easy, and I'm afraid it wouldn't have been possible without the support of sincere and caring friends. I've been incredibly lucky to have such a group by my side. I want to especially thank JJ Oon, Lakshmi Kumar, Sebastian Carrasco, Sohyoun Yun-Cárcamo, Cameron Lee, Jonathan Fernandes, Anubhav Gupta, Duong Le, Aakash Ravi, David Barbehenn, and Vivian Nguyen. I also want to thank the wonderful Iranian community here for their friendship and the deep sense of belonging they offered: Majid Ekhterachian, Ali Lavasani, Masoud Mohammadi, Alireza Parhizkar, Ali Fahimniya, Batoul Banihashemi, Erfan Abbasgholinejad, Saba Etezad-Razavi, and many more.

Last but certainly not least, I want to express my deepest gratitude to my family. I can't begin to imagine how difficult it must have been for my parents to see me only through a phone screen for six long years–yet they supported me in every way they could. I'm also incredibly thankful to my brother and sister-in-law, Javad and Haleh, for being a constant source of strength and support throughout this journey. I hope to see you all very soon.

Reza Ebadi

June 17, 2025

Table of Contents

List of Tables

List of Figures

Chapter 1: Introduction

The Standard Model of particle physics has proven highly effective in describing fundamental interactions across a vast range of scales, from the subatomic to the cosmological. However, it remains an incomplete theory. It does not account for astrophysical and cosmological evidence pointing to the existence of dark matter and dark energy, and it leaves unresolved theoretical issues, such as the Strong CP problem. As a result, exploring physics beyond the Standard Model is a major frontier in our quest to understand the fundamental nature of the universe.

Dark matter (DM) offers a crucial window into physics beyond the Standard Model. Although its gravitational influence on galactic and cosmological scales is well-established, the fundamental particle nature and non-gravitational interactions of DM remain undetected. Understanding these properties is among the most profound open questions in modern physics and forms the core focus of this thesis. Theoretical models propose a diverse range of DM candidates, spanning an extraordinary spectrum from ultra-heavy composite states to ultralight bosonic fields; see Figure 1.1. Exploring this vast landscape requires the development of novel precision measurement methods capable of pushing experimental sensitivities into previously inaccessible regimes.

This thesis focuses on advancing and applying innovative precision measurement techniques to probe dark matter, leveraging quantum sensing, optical interferometry, and astrophysical observations. The research spans multiple frontiers, from laboratory-scale solid-state detectors to galactic-scale observations, unified by a common goal: to open new win-

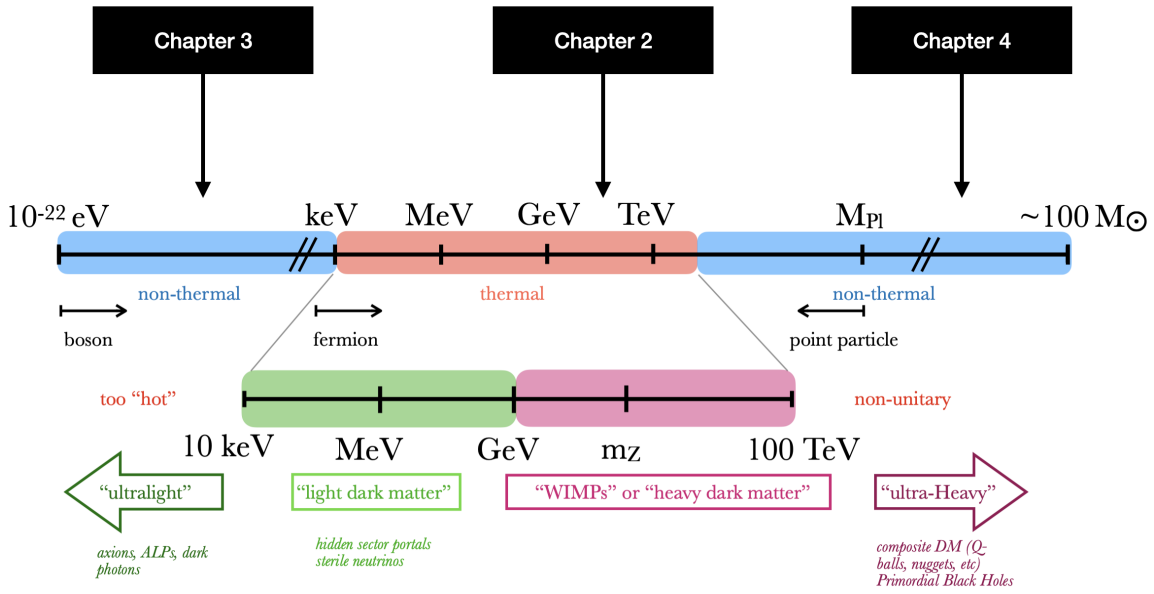

Figure 1.1: The dark matter landscape spans many orders of magnitude in mass. This illustration highlights the regions of parameter space explored in Chapters 2, 3, and 4 of this thesis. Adapted from Ref. [491].

dows into the dark sector through precision experimental tools.

Chapter 2 introduces a next-generation directional detection concept for weakly interacting massive particles (WIMPs) utilizing solid-state quantum sensing in wide-bandgap semiconductors such as diamond. Directional detection is a critical requirement for overcoming neutrino background limitations in future dark matter searches. By encoding nuclear recoil directions (correlated with the incoming particle's directions) as durable nanoscale damage tracks readable by atomic-scale quantum sensors and/or advanced microscopy techniques, this approach offers a promising path toward background discrimination and improved WIMP sensitivity.

Chapter 3 proposes the GALILEO experiment, a novel dark matter detection scheme exploiting electro-optical materials whose refractive index oscillates in the presence of coherently oscillating light dark matter fields such as axions or axion-like particles. Using a resonant Michelson interferometer, GALILEO aims to access an unexplored mass range

beyond the reach of traditional microwave cavity haloscopes. This method offers a complementary and scalable approach to search for ultralight bosonic dark matter candidates.

Chapter 4 explores a novel search strategy for ultra-heavy dark matter (UHDM) through geological quartz samples. UHDM candidates with large interaction cross sections can leave distinctive long, straight damage tracks as they traverse matter. The exceptional age and large exposure of geological quartz compensate for the low UHDM flux, while electron microscopy enables high-resolution, low-background readout of these rare events. This approach opens a unique avenue to probe dark matter beyond the reach of conventional direct detection experiments.

Chapter 5 transitions to an astrophysical precision measurement technique by exploring how gravitational wave observations from double white dwarf (DWD) binaries by the Laser Interferometer Space Antenna (LISA) can be used to dynamically probe the Milky Way's gravitational potential. The impact of apparent acceleration on the gravitational waveforms of these long-lived, quasimonochromatic sources is examined. The dynamical information encoded in the gravitational wave phase evolution is analyzed to provide a complementary and, in principle, more direct constraint on the underlying Galactic potential (and therefore mass distribution) than what is accessible through kinematics alone. A model for the expected apparent accelerations across the Galaxy is constructed, and LISA's sensitivity to these effects is evaluated through Fisher matrix analyses based on a realistic simulated population of resolvable DWDs. The opportunities and limitations of using DWDs as Galactic accelerometers are highlighted, and the scientific return of this probe is shown to be enhanced by combining gravitational wave and electromagnetic observations.

Together, these chapters present a set of novel experimental and observational tools at the intersection of quantum sensing, optical metrology, materials science, and astrophysics. By pushing the boundaries of precision measurement, this thesis advances the search for dark matter across a vast range of candidate masses and interaction types, highlighting the

critical role of innovative technology and cross-disciplinary approaches in tackling one of the most profound problems in physics.

1.1 Citations to Previously Published Work

This dissertation covers research reported in the following articles:

- **LISA double white dwarf binaries as Galactic accelerometers**,
  Reza Ebadi, Vladimir Strokov, Erwin H. Tanin, Emanuele Berti, Ronald L. Walsworth
  Published in: Phys. Rev. D 111 (2025) 4, 044023

- **GALILEO: Galactic Axion Laser Interferometer Leveraging Electro-Optics**,
  Reza Ebadi, David E. Kaplan, Surjeet Rajendran, Ronald L. Walsworth
  Published in: Phys. Rev. Lett. 132 (2024) 10, 101001

- **Directional Detection of Dark Matter Using Solid-State Quantum Sensing**,
  Reza Ebadi, Mason C. Marshall, David F. Phillips, Johannes Cremer, Tao Zhou, Michael Titze, Pauli Kehayias, Maziar Saleh Ziabari, Nazar Delegan, Surjeet Rajendran, Alexander O. Sushkov, F. Joseph Heremans, Edward S. Bielejec, Martin V. Holt, Ronald L. Walsworth
  Published in: AVS Quantum Sci. 4, 044701 (2022)

- **Ultraheavy dark matter search with electron microscopy of geological quartz**,
  Reza Ebadi, Anubhav Mathur, Erwin H. Tanin, Nicholas D. Tailby, Mason C. Marshall, Aakash Ravi, Raisa Trubko, Roger R. Fu, David F. Phillips, Surjeet Rajendran, Ronald L. Walsworth
  Published in: Phys. Rev. D 104 (2021) 1, 015041

List of published articles during PhD that are not covered in the current dissertation:

- **Fingerprints of a Non-Inflationary Universe from Massive Fields**,

  Jerome Quintin, Xingang Chen, Reza Ebadi

  Published in: JCAP 09 (2024) 026

- **Diamond Micro-Chip for Quantum Microscopy**,

  Shahidul Asif, Hang Chen, Johannes Cremer, Shantam Ravan, Jeyson Tamara-Isaza, Saurabh Lamsal, Reza Ebadi, Yan Li, Ling-Jie Zhou, Cui-Zu Chang, John Q. Xiao, Amir Yacoby, Ronald L. Walsworth, Mark J.H. Ku

  Published in: AVS Quantum Sci. 6, 044405 (2024)

- **Gravitational waves from stochastic scalar fluctuations**,

  Reza Ebadi, Soubhik Kumar, Amara McCune, Hanwen Tai, Lian-Tao Wang

  Published in: Phys. Rev. D 109 (2024) 8, 083519

- **Spectral distortions of astrophysical blackbodies as axion probes**,

  Jae Hyeok Chang, Reza Ebadi, Xuheng Luo, Erwin H. Tanin

  Published in: Phys. Rev. D 108 (2023) 7, 075013

- **Classical cosmological collider physics and primordial features**,

  Xingang Chen, Reza Ebadi, Soubhik Kumar

  Published in: JCAP 08 (2022) 083

- **High-Precision Mapping of Diamond Crystal Strain Using Quantum Interferometry**,

  Mason C. Marshall, Reza Ebadi, Connor Hart, Matthew J. Turner, Mark J.H. Ku, David F. Phillips, Ronald L. Walsworth

  Published in: Phys. Rev. Applied 17 (2022) 2, 024041

- **Milky Way Accelerometry via Millisecond Pulsar Timing**,

David F. Phillips, Aakash Ravi, Reza Ebadi, Ronald L. Walsworth

Published in: Phys. Rev. Lett. 126 (2021) 14, 141103

1.2 Co-author Contributions

Chapter 2

This chapter was originally written entirely by me and presents an overview of a larger research effort within the Walsworth group, focused on developing diamond as a low-energy nuclear recoil particle detector. The content was later revised and refined with input from co-authors and subsequently published in *AVS Quantum Science* **4**, no. 4 (2022) [162]. None of the material presented in this chapter is included in another student's Ph.D. thesis. I led the writing of the original draft of this review paper. Mason Marshall, David Phillips, and Ron Walsworth assisted with writing and editing. Surjeet Rajendran, Alex Sushkov, and Ron Walsworth contributed to the development of the original concept. Mason Marshall, David Phillips, and I also contributed to the development of new experimental ideas and analyses. Johannes Cremer, Tao Zhou, Michael Titze, Pauli Kehayias, Maziar Saleh Ziabari, Nazar Delegan, F. Joseph Heremans, Edward Bielejec, and Martin Holt contributed to various experiments reviewed in the paper and assisted in validating its content. This work was performed under the supervision of Ron Walsworth.

Chapter 3

This chapter was originally written entirely by me and presents findings from my research conducted in collaboration with co-authors. The content was later revised and refined with input from co-authors and subsequently published in *Physical Review Letters* **132**, 101001 (2024) [163]. None of the material in this chapter appears in another student's PhD thesis. I led the primary computations and the writing of the original draft of this paper. Surjeet Rajendran, David Kaplan, and I contributed to the development of the original concept.

Surjeet Rajendran, David Kaplan, and Ron Walsworth assisted with editing and validation of the content. This work was performed under the supervision of Ron Walsworth.

Chapter 4

This chapter is based on work published in *Physical Review D* **104**, no. 1 (2021): 015041 [161]. For a comprehensive discussion and complete technical details, see Appendix A, which contains the full text of the original article. This work also appears in the PhD thesis of co-author Erwin Tanin, titled *Beyond the Standard Model Explorations*, submitted to Johns Hopkins University. Erwin Tanin, Anubhav Mathur, and I led the project and the writing of the original draft of this paper. Erwin Tanin and Anubhav Mathur led the development of the theoretical framework and signal computation, while I led the development of the experimental techniques. Nick Tailby performed the SEM measurements and contributed information about the Jack Hills quartz samples presented in the paper. David Phillips, Mason Marshall, and Aakash Ravi assisted in refining the proposed experimental methods. Nick Tailby, Roger Fu, and Raisa Trubko assisted with and validated the geology- and sample-related content. Surjeet Rajendran and Ron Walsworth assisted with editing and validation of the content. This work was performed under the supervision of Ron Walsworth.

Chapter 5

This chapter is based on work published in *Physical Review D* **111**, no. 4 (2025): 044023 [164]. For a comprehensive discussion and complete technical details, see Appendix B, which contains the full text of the original article. This work also appears in the PhD thesis of co-author Vladimir Strokov, titled 'Open Mic with LISA: Intermediate-Mass Black Holes and Double White Dwarfs', submitted to Johns Hopkins University. Ron Walsworth and I originally conceived the idea for this paper. Erwin Tanin and I led the initial primary computations, and Vladimir Strokov performed the Fisher error estimations. Vladimir Strokov, Erwin Tanin, and I led the writing of the original draft of this paper. Emanuele

Berti provided valuable guidance on the gravitational wave physics relevant to the analysis. Emanuele Berti and Ron Walsworth assisted with editing and validation of the content. This work was performed under the supervision of Ron Walsworth and Emanuele Berti.

Chapter 2: Directional Detection of Dark Matter Using Solid-State Quantum Sensing

Dark matter (DM) is one of the most pressing puzzles in modern physics [501]. Possible candidates for DM include weakly interacting massive particles (WIMPs) in the mass range of a few GeV to 100 TeV. Thermally-produced WIMP DM acquires its observed relic abundance through the freeze-out mechanism in the early universe [50]. WIMPs are also strongly motivated from the perspective of model building, predicted in numerous theories beyond the Standard Model [85, 126, 229, 273, 347]. There have been several dedicated experiments looking for WIMP particles in the cross section-mass parameter space for the past decades. Detectors of this type look for nuclear recoils induced by WIMPs in a background-controlled environment. The null results of these experiments exclude a large portion of the parameter space of WIMPs [397].

Next-generation multiton experiments will be sensitive to lower cross sections [1, 2]. Nevertheless, these experiments will ultimately be sensitive to coherent scattering from neutrino scattering as well. The irreducible neutrino background, traditionally called the neutrino floor, produces nuclear recoil spectra similar to those of WIMP-induced recoils [76, 213, 313, 425]. Thus, additional information is required to distinguish between the neutrino background signal and the putative WIMP signal. Angular distributions of WIMP and neutrino fluxes can provide such a discrimination tool. As a result of the motion of the solar system within the Galactic halo, WIMP DM flux exhibits a dipolar structure. Solar

neutrinos, the most imminent neutrino background [38], will also be localized in a relatively small angular distance, improving directional discrimination power further. Directional detectors can determine the incoming direction of incident particles [211, 303, 335, 451, 453]. As a result, developments toward multiple directional detectors are underway worldwide, each with its own advantages and challenges [453].

Our goal is to develop a solid-state detector for directional WIMP detection [297, 367]. The detector we envision operates in hybrid mode: nuclear recoil event registration is performed in real time using charge, phonon, or photon collection; and directional information is read out using high-resolution mapping of the lattice damage left behind incident WIMPs or neutrinos. The proposed detector scheme integrates real-time event registration, three-dimensional directionality information, and high-density target material. Gas-based time-projection chambers (TPCs) have mature directional detection technology and offer real-time event detection and full 3D directional readout as well [451]; however, they feature a very low target density and require large volumes. The scalability of these detectors is therefore limited. Probing DM mass $> 10\,\mathrm{GeV}$ below the atmospheric neutrino floor, despite being theoretically well-motivated [5, 46, 223, 252, 382], would be especially challenging for gas TPCs [334]. However, solid-state detectors could allow to access this parameter space.

In the proposed detector, directional readout and event registration require different sets of technologies. DM detection using nuclear or electron recoils in semiconductors is a mature technology; semiconductor-based DM detection experiments are already operational [18, 290, 371, 444]. Our proposed experiment will use similar methods to register recoil events [297, 367]. Mapping of directional lattice damage, however, requires a different set of capabilities. Our research is focused on developing directional detectors enabled by point defect quantum sensing in wide-bandgap semiconductors. We discuss in the following sections how recent developments in defect-based quantum sensing pave the way for

directional detection. We specifically focus on diamond as a viable target material. Diamond is a leading platform for emerging quantum technologies [58]. Many of the technical developments have been made over the past decade in diamond-based quantum sensing that are applicable to directional readout. In addition, the demand for quantum-grade synthetic diamonds has resulted in efficient protocols for the production of high-quality, low-strain diamonds [189, 298].

In our research program for the 2020s, we aim to demonstrate directional readout capabilities using diamond. Implementing conventional DM detection methods in diamond is also an ongoing research with promising prospects [108, 270]. Combination of directional readout methods (utilizing quantum sensing methods [58, 297, 367]) and nuclear recoil registration methods (similar to those used in silicon and germanium-based detectors [18, 290, 371, 444]), it would be possible to build a detector that retains sensitivity to WIMP despite the presence of irreducible neutrino background.

The rest of the paper is organized as follows. In Sec. 2.1, we discuss the neutrino background for direct DM detectors; briefly discuss directional detection, current and proposed technologies; and give an overview of the working principle of the envisioned solid-state detector. In Sec. 2.3, we summarize the state-of-the-art techniques for directional readout in diamond, summarize our recent advances, and discuss anticipated improvements. A method of producing injected signals for characterization of detector efficiency is discussed in Sec. 2.4. We conclude with a summary and outlook in Sec. 2.5.

2.1 WIMP detection below neutrino floor

2.1.1 Neutrino floor

Neutrinos couple to quarks via the neutral Z boson exchange [218], resulting in coherent scattering off nucleons in an atomic nucleus for neutrinos whose energies are below a

few tens of MeV [188]. Thanks to technological advances in detecting low-energy (down to a few keV) nuclear recoils, coherent elastic neutrino-nucleus scattering (CEνNS) has been observed recently in CsI[Na] scintillator [20] and liquid argon [19] detectors. The measurements offer a new pathway that will provide novel advances in a wide range of fields, including neutrino and nuclear physics [32, 152, 156, 260, 261, 264, 345], possible hidden sectors [57, 147, 157], and astrophysics [51, 187, 230, 395, 475].

Through CEνNS, astrophysical neutrinos could trigger background events in low-energy nuclear recoil detectors. Multi-ton-scale DM direct detection experiments could be sensitive to CEνNS from solar and atmospheric neutrinos which cannot be shielded against, an irreducible background known as the *neutrino floor*. In fact, xenon-based DM detectors (e.g., XENONnT) are expected to detect CEνNS from ^{8}B solar neutrinos in near future, which would resemble the detection of 6 GeV c^{-2} DM [38]. DARWIN is a next-generation liquid xenon time projection chamber (TPC) detector proposed by the XENON collaboration, which employs a 50-ton (30-ton) active (fiducial) mass and can operate for five years, and aims the sensitivity at the atmospheric neutrino floor [1]. In addition, the DarkSide collaboration has proposed ARGO, a 300-ton (200-ton) active (fiducial) liquid argon TPC detector with a five-year operation time, so as to achieve neutrino floor [2].

There can be a substantial overlap between the recoil spectra induced by neutrinos and WIMPs, which makes the distinction between them difficult [76, 213, 313, 425]. A small difference in the tails of the recoil spectra could in principle be used as a discrimination tool, but it would require thousands of neutrino events, making it impractical with any proposed future experiment. Other methods for breaking the neutrino floor have been proposed, such as utilizing timing information [140, 388] or complementarity between detectors [384]. Nevertheless, in the low-statistics limit, directional detection appears to be the only feasible method [211, 335].

Despite the similarities between the signals, a conventional DM search would have

been possible if there had been a precise understanding of neutrino background levels. Recently some have advocated using the term "neutrino fog" rather than "neutrino floor", implying a challenging, but not impossible signal-background discrimination [140, 191, 193, 342, 384, 388]. Even though neutrino-nucleus cross sections are relatively accurately determined, neutrino fluxes are typically subject to large systematic uncertainties, causing large uncertainties in the number of expected neutrino events [42]. Thus, the neutrino flux uncertainty saturates the DM discovery limit in higher exposures [76]. Ref. [342] defines neutrino floor in terms of the derivative of the discovery limit as a function of exposure $n = -(\mathrm{d}\ln\sigma/\mathrm{d}\ln N_\nu)^{-1}$, where N_ν is the number of neutrino events and it is proportional to the exposure; the neutrino floor is the boundary leaving the standard Poissonian regime ($n = 2$) and beginning systematic uncertainty saturation ($n > 2$). (Note that while this definition of neutrino floor is useful for illustrating the neutrino background and comparing different target materials, it does not represent a fundamentally preferred definition.) Figure 2.1 shows the neutrino floor calculated using the method described above for several different target materials. Solar neutrinos dominate the neutrino floor for DM masses $\gtrsim$ 5 GeV; for slightly larger masses diffuse supernova neutrino background dominates; and eventually, for DM masses greater than $\gtrsim$ a few 10 GeV, atmospheric neutrinos are the dominant contribution (for light target nuclear masses like helium or carbon, solar neutrinos are also a significant contributor at this regime since the scattering kinematics allow for large recoil energies) [342].

2.1.2 Directional nuclear recoil detection

As the solar system moves towards Cygnus, the angular distribution of DM scattering rate exhibits a dipolar feature [421]. The angular distance between Cygnus and the Sun changes between 60° (in March) and 120° (in September) over the course of a year.

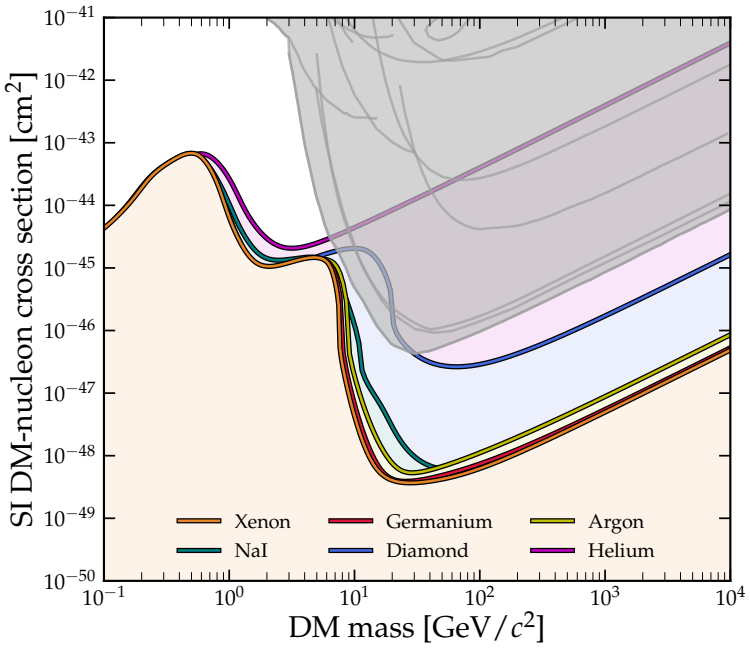

Figure 2.1: Spin-independent DM parameter space, illustrating the neutrino floor for a variety of target materials, including diamond. We use typically dominant ^{12}C isotope. Produced using the method introduced and implemented in ref. [342]. Shaded gray area shows current excluded region. Refer to [342] for further discussion.

This angular separation allows the separation of solar neutrinos and dark matter in a directional nuclear recoil detector [303, 335, 451, 453]. There is overwhelming evidence that Milky Way kinematic structures go beyond the equilibrium Standard Halo Model [36, 68, 114, 115, 135, 190, 198, 199, 276, 322, 323, 326, 394, 469, 474, 483]. First of all, these phase-space structures can influence interpretation of direct detection experiments, but they may also be observed in directional detectors [266]. Furthermore, the dipolar DM angular structure can improve DM reach beyond atmospheric neutrino floor as well; however, to achieve sensitivity to atmospheric neutrinos higher exposure is required [451]. Although atmospheric neutrino flux is not localized as solar neutrino flux is, it exhibits angular structure caused by cosmic rays passing through different thicknesses of atmosphere and their interaction with geomagnetic fields [334]. Such a feature could further enhance the efficiency of directional detection.

Several directional detection technologies are in various stages of development [453]. Identifying three-dimensional direction and head/tail information on an event-by-event basis is the ideal scenario for directional detection. Gas-phase time projection chamber (TPC) detectors [55, 62, 310, 387, 452] provide well-developed 3D vectorial directional readout capabilities [451]. But even so, gas-phase detectors that operate at and below the neutrino floor would require extremely large volumes, since the target mass determines the detector's discovery limit. The use of nuclear emulsion-based detectors provides high-resolution recoil track imaging at higher target densities; however, they are time-consuming to read out and provide only time-integrated signals (hence, a detector installed on a Cygnus-tracking equatorial telescope would be optimal) [15, 22, 26, 27, 201, 448]. Although emulsion-based detectors can image 2D recoil tracks, it is unclear whether they can reconstruct 3D tracks and head/tail signatures.

There are also indirect signatures of DM directionality that can be detected. Solid-state anisotropic scintillators (e.g. $ZnWO_4$) [399, 409] can exploit modulation of incoming

DM direction relative to crystal axes in order to statistically provide a directional signal [66, 110, 113, 139] (although, strong anisotropy at low recoil energies still has to be confirmed experimentally). A statistical measurement of this kind would require much higher exposures than event-resolved directional methods. As a directional signal, the relative direction of the primary ionization cloud and the applied electric field affects the scintillation yield in liquid noble gas detectors, a method known as columnar recombination [109, 330]. The first measurements of direction dependence of scintillation yield, however, suggests a small effect. Also, this method is sensitive to only one track dimension and lacks a head/tail signature, so it is probably ineffective for DM detection below the neutrino floor [334].

We envision using quantum point defects in solid-state detectors to provide directional readout. Due to intensive work on instrumentation of sensitive charge and phonon detectors during the last decade, semiconductor DM detectors based on silicon or germanium have become possible [17, 290, 371, 392, 420]. According to the same principles and using developed instrumentation technologies, wide-bandgap semiconductors such as diamond [270, 367] and silicon carbide [210, 367] are proposed for DM detection. These detectors' semiconductor properties and low nuclear mass provide a complementary sensitivity profile to existing detectors. Furthermore, a WIMP or neutrino event in such a detector would leave a characteristic track of damage, with the crystal acting as a "frozen bubble chamber" to record the direction of the particle's impact [297, 367]. It results from a cascade of secondary nuclear recoils initiated by the initial scattering. The damage track can be read out via spectroscopy of quantum point defects such as nitrogen-vacancy (NV) [58, 166, 282, 390] and silicon-vacancy (SiV) [306] defects in diamond, and divacancies in silicon carbide [447, 479]. (In Section 2.3, we cover readout methods in greater detail.) Simulations for a diamond target indicate measurable orientation and head/tail asymmetry down to 1-3 keV of recoil energy [367]. Therefore, quantum defect-based solid-state detectors offer both full directional information (akin to gas TPCs), as well as high density.

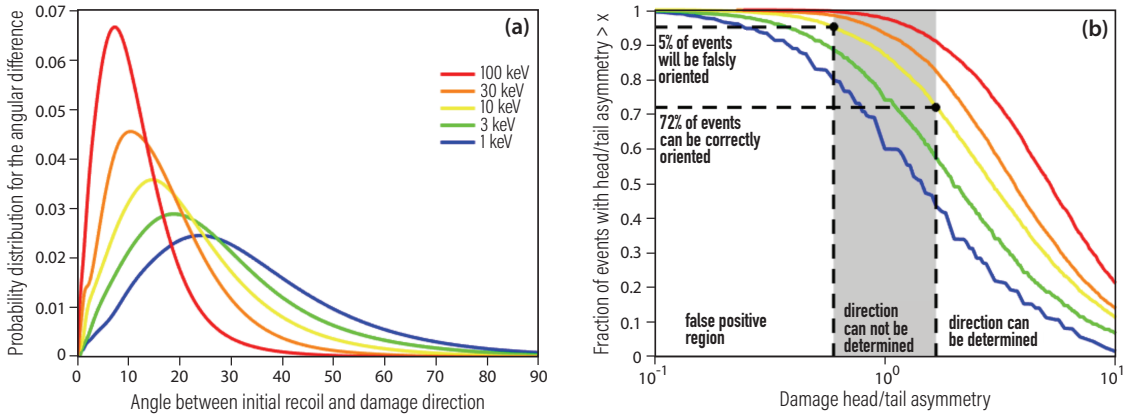

Figure 2.2: Result of the SRIM simulation assuming a carbon lattice (appropriate for diamond) and implantation of a carbon ion with energy in the range $\sim 1-100\,\mathrm{keV}$ (representing the initial recoiling nucleus). **(a)** Distribution of the angular difference between the initial recoil direction and the damage track direction. Higher recoil energies are predicted to have a higher correlation. **(b)** Distribution of damage head/tail asymmetry. The asymmetry is defined as the ratio of the number of lattice vacancies and interstitial nuclei in the first and last third of the damage. As an example, for 10 keV initial ion, we predict about 70% efficiency and 5% false positive rate. Reproduced from ref. [367].

2.1.3 Working principle of a solid-state point defect-based directional detector

In a solid-state crystalline detector, WIMP recoil would impart substantial kinetic energy onto a target nucleus, knocking it off from its lattice point, giving rise to a chain of secondary nuclear recoils, leaving behind a characteristic damage track, comprising interstitial nuclei, lattice vacancies, and distorted bonds. SRIM simulations [499] for a diamond detector predict damage tracks will be tens of nanometers long for recoils with energies in the range of $10-100\,\mathrm{keV}$ [367], equivalent to WIMP masses in the range of $1-100\,\mathrm{GeV}$; the orientation of these damage tracks is well correlated with the initial recoil orientation (see Figure 2.2a); and they will exhibit an observable head/tail asymmetry (see Figure 2.2b).

We envision integrating directional detection within a conventional WIMP detector with

well-developed instrumentation and background discrimination methods [297, 367]. Hybrid detectors like this would be able to detect candidate WIMP events by using established methods, such as charge, phonon, and scintillation detection using semiconductor solid-state detectors. Detector designs utilizing fabricated charge collection electrodes and phonon sensors provide coarse localization of events at mm scale [16, 96]. To operate at the neutrino floor or below, meter-scale solid-state detectors are needed (see Sec. 2.1.1). Following event localization to a mm-scale chip in a modular detector, that chip can be extracted and interrogated to determine the direction of damage. However, using existing methods, it would be time-prohibitive to scan an entire mm-scale chip with nm resolution. We propose a two-step damage track reconstruction strategy: a micron-scale localization of the damage track using optical-diffraction-limited imaging techniques, followed by a high-resolution 3D reconstruction of the damage track. Therefore, the proposed detector's readout can be summarized in three steps as follows (see Figure 2.3):

- **STEP I:** Event localization at mm scale using charge, phonon, or photon collection.
- **STEP II:** Damage track localization at micron scale using optical-diffraction-limited techniques. (See sections 2.3.1 and 2.3.2 for methods.)
- **STEP III:** Mapping damage tracks at nanoscale using either superresolution optical methods or hard x-ray microscopy. (See sections 2.3.3 and 2.3.4 for methods.)

For this hybrid detection method, we propose to develop a detector with diamond as its target material. WIMP detectors based on diamond are currently being studied for next-generation semiconductor-based detectors. Diamond has excellent semiconductor properties, and the carbon nucleus has a relatively light mass, making it a suitable candidate for low-mass DM candidates, as compared with xenon or other heavy target materials. The implementation of traditional event detection techniques in diamond is an active topic of

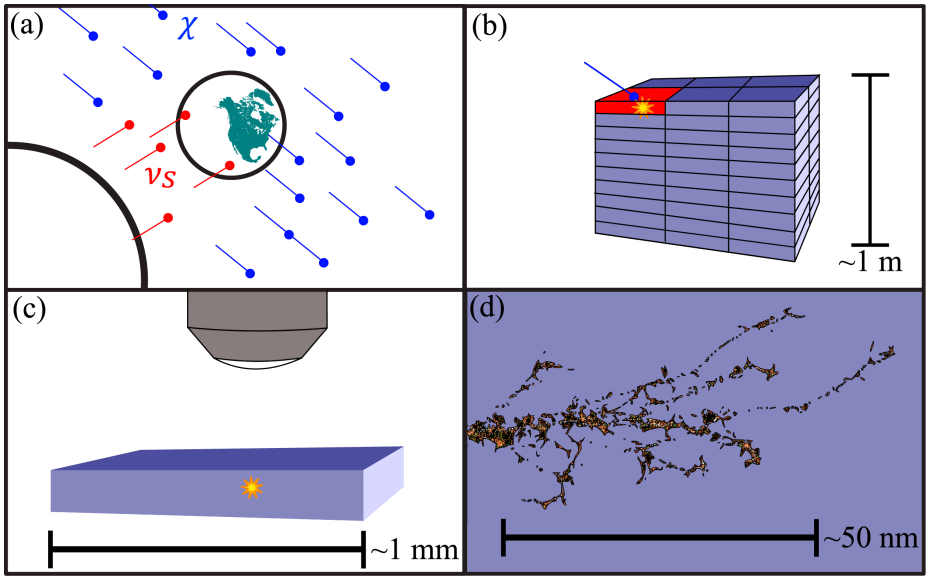

Figure 2.3: Schematic overview of the proposed directional dark matter detection procedure. **(a)** Solar neutrinos (ν_S) stream towards the earth. Because of the motion of the solar system in the Galactic rest frame, there is a preferred direction of incoming WIMP particles (χ) on the earth (so-called WIMP "wind"), distinct from solar neutrinos, allowing directional discrimination (see text for details). **(b)** WIMP or neutrino particles interact occasionally with the shielded solid-state detector at an underground facility, depositing energy as well as causing cascades of nuclear recoils, leaving a long-lasting crystal damage. Charge, phonon, or photon collection is used to detect and localize the event to a mm-scale segment of the detector. The time of the event determines the orientation of the detector with respect to both the Sun and the galactic WIMP wind. **(c)** The triggered segment is removed from the bulk of the detector. Using optical-diffraction-limited methods, damage is localized in a micron-scale volume. **(d)** The nanoscale structure of crystal damage is mapped, allowing WIMP and neutrino events to be distinguished. Reproduced from ref. [297].

research [270]; this includes the first demonstration of a diamond calorimeter coupled to a transition edge sensor (TES) at cryogenic temperatures [108]. Diamond is a promising material for semiconductor electronics applications [236, 482] as well as for quantum sensing [58, 166, 282, 390] and quantum information processing [132, 133] applications that make use of diamond's lattice point defects. Such technological demand is supported by modern diamond growth techniques using chemical vapor deposition (CVD) [166, 236] which enable repeatable, fast, and low-cost growth of uniform crystals. As a result, diamond has also been widely used in particle physics research [436], including in the ATLAS and CMS detectors at the LHC [332]. For the proposed directional WIMP detector, a diamond detector at cubic meter scale is needed to achieve sensitivity below the neutrino floor. In light of the advances over the last decade, a realistic development should be capable of producing the volumes of diamond required for such a detector. With optimized crystal growth protocols [166], both semiconductor properties, which enable very sensitive charge and phonon extraction, and very uniform, low crystal strain properties are achieved, which are advantageous for the proposed directional detector.

In the remaining sections, we provide an overview of methods available for damage track localization and nanoscale mapping (Sec. 2.3) as well as a method for generating injected signals (Sec. 2.4). Here, we present an estimation of the signal strength and background rate in order to evaluate the feasibility of methods based on their sensitivity and speed. SRIM simulations indicate that nuclear recoil-induced damage tracks relevant to WIMP events are $\mathcal{O}(10-100)\,\mathrm{nm}$ in length and have lattice vacancies of $\mathcal{O}(50-300)$ [367]. It is possible to detect the strain caused by such a lattice damage. Following [367], we assume a fractional strain of $\Delta x/x \sim 10^{-6}$ at a distance of 30 nm from a single lattice defect. Furthermore, the strain from each individual point defect in a damage cluster can be added to find the strain from the entire cluster [172]. We benchmark damage localization by a simplified model of the strain signal within a $\mu\mathrm{m}^3$ volume that contains the damage

cluster: for each vacancy, a cylinder of uniform strain $\sim 10^{-6}$ with height and radius 30 nm, while the strain outside the cylinder falls off as $1/r^3$ [297].

We benchmark the damage localization time to not exceed the expected event rate in the detector, so the event direction can be measured as each event is detected before the next occurs. (The localization experiment could, however, be parallelized using multiple setups if necessary.) It is expected that the rate of events from coherent solar neutrino scattering, mainly from ^{8}B solar neutrinos, will be approximately $\mathcal{O}(30)$ per ton $\times$ year [69, 313]. With a low rate of WIMP events, this would limit the localization time to about 10 days. We consider, however, a conservative three-day target between event registration and damage localization at the micron scale to account for a potential WIMP signal at the neutrino floor, as well as background events [297]. Note that we assume a detector with sensitivity below the neutrino floor will have fewer background events than neutrino events. Furthermore, quantum diamond microscopy experiments (see sections 2.3.1, 2.3.2, and 2.3.4) are expected to take place on-site at a shielded complex that houses the detector, using infrastructure that is constructed from high-purity materials, similar to what is used in current WIMP detectors [39]. Note that the complementary technique of scanning x-ray diffraction microscopy for nanoscale strain mapping requires access to synchrotron facilities (see Sec. 2.3.3). Nevertheless, localization of the WIMP/neutrino signal to a small μm^3 volume before transport and shielding during the transport would eliminate significant background contamination. With a reasonable allocation of synchrotron beam time, scanning the micron-scale volumes of interest should also be feasible.

2.2 Nitrogen-vacancy centers in diamond

We present a brief overview of the NV physics and related quantum sensing techniques in this section; the reader familiar with this topic may skip to the next section.

Nitrogen-vacancy centers (NVs) are composed of a nitrogen atom and an adjacent vacancy in a diamond crystal (see Figure 2.4a), and they can be classified according to their orientation in four crystallographic directions. Nanoscale NV centers exhibit quantized energy levels similar to atomic systems. The energy levels couple to magnetic fields, electric fields, temperature, and the lattice strain; this allows NV centers to function as quantum sensors [12, 52, 144, 304, 437]. The transition frequencies can be measured using phase-sensitive interferometric methods [363, 368] or alternatively through resonance features in NV photonic and electronic response [58]. NV sensors feature high spatial resolution as well as operation at ambient temperatures, pressures, and magnetic fields. In particular, negatively charged NV^- is the most useful for quantum sensing. The NV^- is a two-electron system with a triplet spin-1 ground state that typically has a longitudinal relaxation time $T_1 \simeq 6\,\mathrm{ms}$ [239, 380] and decoherence times T_2 of up to a few ms [53] under ambient condition. Although NVs are observed in three charge states (NV^-, NV^0, and NV^+), NV^- is favored for quantum sensing [153]; in reminder of the discussion, NV stands for the negatively charged defects.

Ground state spin Hamiltonian. With a bias magnetic field aligned with the NV symmetry axis z, the simplified NV electronic ground state Hamiltonian can be written as [246]

$$\frac{\mathscr{H}_{\mathrm{gs}}}{h} \simeq (D + \mathscr{M}_z) S_z^2 + \gamma B_z S_z \,. \tag{2.1}$$

$D \simeq 2.87\,\mathrm{GHz}$ is the zero-field-splitting (ZFS) parameter at room temperature, resulting from the spin-spin interactions between the NV electrons. ZFS varies with temperature as $\mathrm{d}D/\mathrm{d}T \simeq -74.2\,\mathrm{kHz/K}$ [13]. $\mathscr{M}_z$ is the spin-strain coupling parameter, which can be converted to lattice strain using proper coupling constants [56]. We ignore the remaining strain-coupling parameters since their contribution is subdominant [246]. The last term is

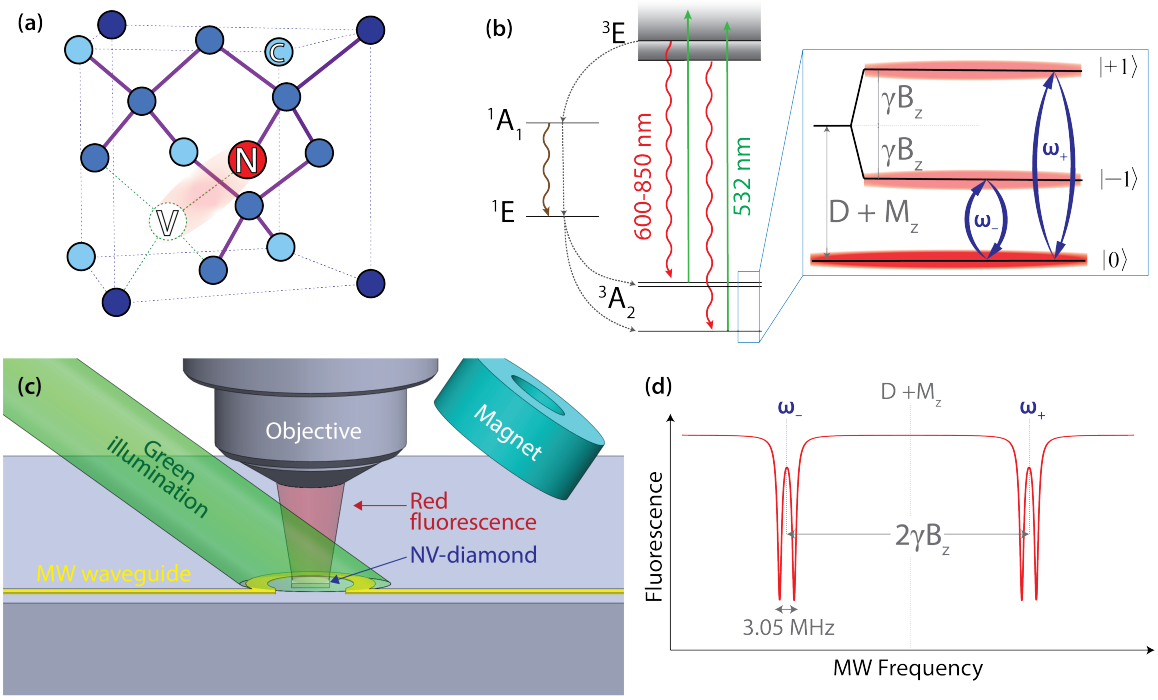

Figure 2.4: Overview of nitrogen-vacancy (NV) centers in diamond. **(a)** Diamond lattice diagram hosting an NV center. **(b)** NV electronic energy level diagram, illustrating triplet ground and excited state as well as singlet states. Intersystem crossing (ISC) through singlet states yields a nonradiative decay pathway. Inset: Ground state spin energy levels. The ISC nonradiative decay path results in dimming of $m_s = \pm 1$ states' fluorescence. MW frequencies of $\omega_\pm$ can be used to drive spin transitions. Further hyperfine splitting results from electronic spin-nuclear spin interactions (not shown). **(c)** Simplified schematic of a quantum diamond microscope (QDM). Permanent magnets and/or Helmholtz coils (not shown) provide a bias field. Green illumination is used to initialize and read out the spin state. MW delivery via the waveguide allows spin transitions. A microscope objective collects red fluorescence and focuses it on a camera (not shown). **(d)** Schematic fluorescence curve as a function of MW frequency: optically detected magnetic resonance (ODMR). Temperature-dependent zero-field-splitting parameter and local strain determine the center frequency, while the axial bias magnetic field determines the splitting between them. The spin-1/2 nuclear spin of ^{15}N contributes to the double resonance structure (splitting of about 3.05 MHz); the ^{14}N spin-1 nucleus would produce triplet hyperfine energies instead (splitting of about 2.16 MHz).

the Zeeman Hamiltonian, which splits $m_s = \pm 1$ eigenstates. The NV electronic gyromagnetic ratio $\gamma = g_e \mu_B / h \simeq 28.03\,\mathrm{GHz/T}$, where $g_e \simeq 2.003$ is the NV electronic g-factor, μ_B is the Bohr magneton and h is the Planck's constant. Hamiltonian (2.1) leads to transition frequencies

$$\omega_{\pm} \simeq (D + \mathscr{M}_z) \pm \gamma B_z \,. \tag{2.2}$$

Energy level diagram of the NV ground state is illustrated in Figure 2.4b (inset). The transition are in the microwave (MW) frequency band, and they can be resonantly driven using MW fields of corresponding frequency.

Spin-dependent fluorescence. NVs can be excited to an excited electronic state by green laser illumination, which decays back to ground state via fluorescence in the red spectrum; in addition, there is a nonradioactive decay pathway which preferentially applies to the spin state excited from the $m_s = \pm 1$ spin ground state, leading to both less fluorescent $m_s = \pm 1$ spin states and a method for spin polarizing the NV ground state to $m_s = 0$ (see Figure 2.4b). Resonance MW driving of spin transitions in the NV ground state, in conjunction with the optically-driven dynamics, results in a decrease in fluorescence level through enabling the non-radiative decay path (see Figure 2.4d). Fluorescence contrast features of this type can be exploited to determine the NV spin state for sensing applications. Figure 2.4c illustrates a simplified schematic of a quantum diamond microscope (QDM), which enables NV-diamond sensing.

Ramsey measurements. Measurement protocols based on quantum interferometry have been successfully and robustly implemented in NV systems. Here we outline a basic Ramsey protocol to introduce the measurement principle (see Figure 2.5); in Sec. 2.3.1, we present our recent advances in engineered strain-sensitive sensing protocols. Ramsey measurements with NVs use a green laser pulse to initialize the spin state at $m_s = 0$. The

spin-polarized state is then driven into an equal superposition state by means of a MW pulse (the so-called $\pi/2$ pulse), which is then allowed to evolve uninterrupted for a period of time. The spin states that comprise the superposition state accumulate a differential phase during the free evolution. Phase accumulation depends on the transition frequencies encoding NV coupling to the environment. During the final MW pulse, which couples the two spin states again, the differential phase is projected to a difference in population between $m_s = 0$ and $m_s = \pm 1$, manifested as interferometry fringes in NV fluorescence (see Figure 2.5c).

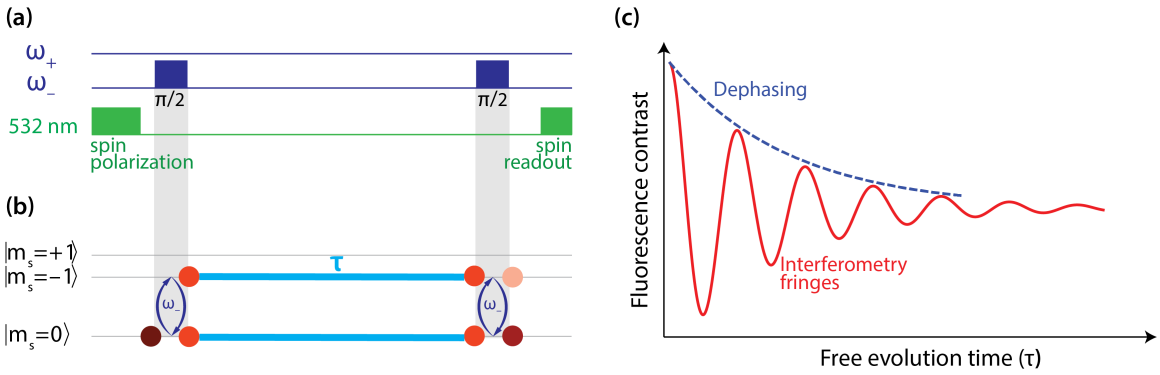

Figure 2.5: Principle of Ramsey measurement protocol in NV systems. **(a)** Ramsey pulse sequence. See text for details. **(b)** Illustration of spin population in each spin state. Following the green initialization pulse, the spin is polarized at $m_s = 0$. The first $\pi/2$ pulse places them in equal superposition of $m_s = 0$ and $m_s = -1$ states. During free evolution, the two populations acquire a differential phase. The second $\pi/2$ pulse projects the phase onto population difference. Note that in this protocol the $m_s = +1$ state does not play a significant role since the longitudinal spin relaxation time is usually longer than the free evolution times limited by the decoherence time scale. **(c)** Schematic NV fluorescence contrast curve as a function of free evolution time. Interferometry fringes reflect the accumulated phase accumulated during the free evolution period. Inhomogeneous phase accumulation causes the overall decay in an ensemble of NV centers.

Ensemble NV-diamond. NV-diamond sensors with ensembles of NV centers provide higher SNR than single NV systems by statistical averaging over multiple single-spin sensors, scaling as square root of number of NVs; additionally, they enable widefield imaging with NV-diamond sensors. High-sensitivity applications using diamond samples with NV

concentrations $\gtrsim$ ppm ($10^{17}\,\mathrm{per\,cm^3}$) have been demonstrated [59, 209, 391, 478, 498]. However, one of the main challenges in using ensemble NVs is the inhomogeneous dephasing, leading to deteriorated coherence time T_2^* (illustrated as the exponentially decaying envelope of the Ramsey curve in Figure 2.5c) and broadened resonance lines. To extend the coherence time, material engineering techniques and dynamical decoupling sequences have been employed, and further improvements are envisioned as well [58].

2.3 Methods for directionality readout in diamond

2.3.1 Optical diffraction-limited strain spectroscopy

In this section, we discuss using nitrogen-vacancy (NV) centers for micron-scale localization of the WIMP or neutrino-induced lattice damage. Strain features can occur in CVD diamond as localized deformations within the crystal lattice because of imperfections propagated during growth and imperfections in surface processing [189, 299]. A variety of methods have been developed for measuring and mitigating such strain features in diamond devices [189, 192, 298]. However, these methods rarely meet all the requirements of the directional dark matter detector proposal (see Sec. 2.1.3). The spatial resolution of birefringence imaging is limited since the signal is integrated over the entire diamond thickness [224, 246]. Raman spectroscopy suffers from relatively high detection noise floor [25, 136]. X-ray tomography and microscopy involve lengthy data acquisition times as well as access to synchrotron beamlines [296, 314]. An alternative method is, however, quantum-point-defect strain spectroscopy, which offers both speed and sensitivity required for directional dark matter detection. NV ground state spin transitions are sensitive to local strain (see Sec. 2.2); therefore, spectroscopic measurements can be used to detect local strain features using NV centers as integrated quantum sensors [95, 246]. Recent developments in NV strain spectroscopy suggest promising prospects for diamond-based directional dark matter

detectors [295].

We model strain induced by each vacancy is modeled as a cylinder of uniform strain 10^{-6} with height and radius 30 nm, while strain outside the cylinder falls off as $1/r^3$ [297] (see Sec. 2.1.3). Based on this model, Figure 2.6 shows the fraction of NV centers experiencing a given stain for a 10 keV recoil, which is 50 induced vacancies (Figure 2.6c). We consider two scenarios of the damage track localization: resolved volume of about 0.1 μm^3 with diffraction-limited 350 nm lateral resolution and 1 μm axial resolution (Figure 2.6a); and resolved volume of 1 μm^3 with three-dimensional μm resolution (Figure 2.6b). NV centers are most sensitive to strain projections onto their symmetry axes. Depending on the relative orientation and location of crystal damage and point defects within the resolved voxel, the strains projected onto different NV centers could add constructively or average to zero. In the former case, we compute the mean averaged strain (leading to frequency shifts), and in the latter case, we calculate the standard deviation of the strain distribution (leading to line broadening and a reduction in coherence time). A small number of NVs exhibit considerably higher strain levels $> 10^{-5}$, whose effect on the signal depends on experimental details. Combining different cases, the voxel-averaged strain signal ranges between 1×10^{-7} and 3×10^{-6} [297].

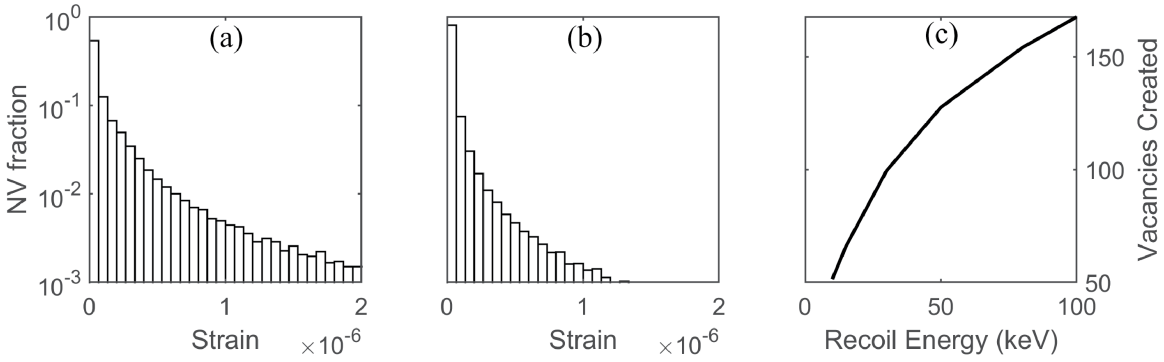

Figure 2.6: Fraction of NV centers experiencing a given strain, within **(a)** 0.1 μm^3 volume and **(b)** 1 μm^3 volume from a 10 keV nuclear recoil. **(c)** Number of vacancies created as a function of the recoil energy, as predicted by SRIM simulations [499]. Reproduced from ref. [297].

NV strain imaging is typically performed using quantum diamond microscopes (QDM) [282] to detect strain-induced modulations in optically detected magnetic resonance (ODMR) spectra [95, 246, 282] (see Figure 2.4c and 2.4d). Although the best measurements with this method demonstrate the sensitivity required to detect WIMP-induced strain, its lengthy averaging times render it unsuitable for dark matter detection. The implementation of Ramsey-like measurements in QDM, however, provides fast and sensitive measurements. The strain Carr-Purcell-Meiboom-Gill (strain-CPMG) sequence, illustrated in Figure 2.7, is a Ramsey-like sequence that is suitable for strain sensing [295] (and thermometry in certain applications [254, 265, 325, 442, 461]). The protocol is insensitive to magnetic inhomogeneities arising from electronic and nuclear spin bath within the diamond lattice, thereby allowing longer NV ensemble dephasing times and enhanced strain sensitivity.

We describe the spin evolution during the strain-CPMG protocol here. We first spin polarize the NV ground state to $|\mathrm{m_s}=0\rangle$. After that, we prepare an equal superposition of $|0\rangle$ and $|-1\rangle$ by applying a microwave (MW) $\pi/2$ pulse resonant with the $|0\rangle \leftrightarrow |-1\rangle$ transition. The NV spins accumulate a relative phase with the rate of $D+M_z-\gamma B_z$ (see eq. (2.1)) during the free evolution of this superposition state. Following that, we apply triplets of MW π-pulses, switching between $|0\rangle \leftrightarrow |-1\rangle$ and $|0\rangle \leftrightarrow |+1\rangle$ transitions that collectively swap the NVs from $|-1\rangle$ to $|+1\rangle$. Therefore, during the middle free evolution time $\tau/2$ the phase accumulation rate is $D+M_z+\gamma B_z$. Following, we apply a reverse swap pulse to transfer the spin population from $|+1\rangle$ back to $|-1\rangle$ and phase accumulation continues for another $\tau/4$ duration. The final accumulated NV phase is independent of B_z and only sensitive to $D+M_z$. The last MW $\pi/2$ pulse projects the accumulated phase onto NV population difference in $|0\rangle$ and $|-1\rangle$ states which we read out using the spin-dependent fluorescence measurement discussed in Sec. 2.2.

The Strain-CPMG protocol employed on a QDM has enabled us to perform high-precision strain mapping at micron-scale resolution and with mm-scale field-of-view [295].

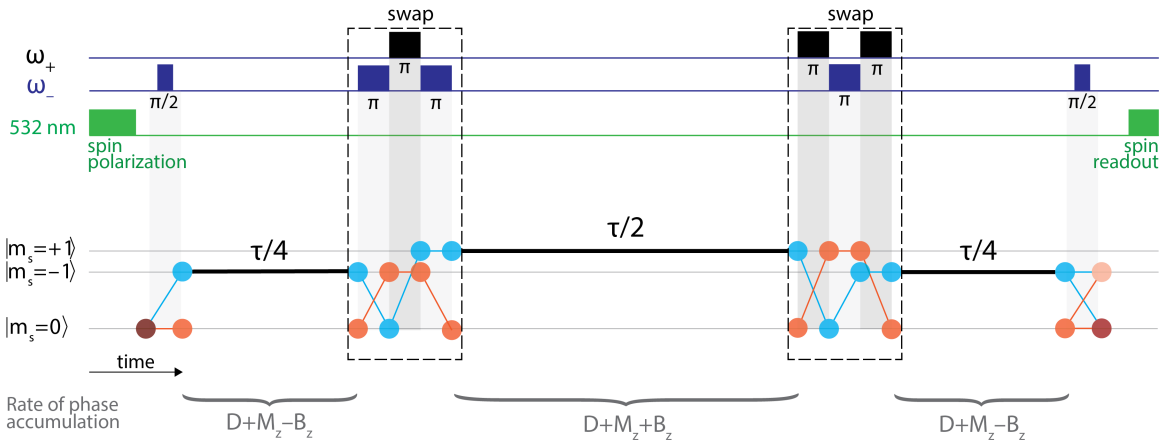

Figure 2.7: Strain-CPMG measurement protocol. Top: Pulse sequence. $\omega_{\pm}$ denotes microwave frequencies addressing $|m_s = 0\rangle \leftrightarrow |m_s = \pm 1\rangle$ transition. Bottom: Evolution of the ground state spin population. See text for details.

The technical details of this work are detailed in ref. [295], but here we summarize the most important implications for directional dark matter detection. We use an NV-diamond sample that is a CVD bulk diamond grown by Element Six Ltd., isotopically purified with 99.995% ^{12}C, and have NV concentrations of about 0.4 ppm. The strain-CPMG measurements exhibit extended dephasing time $T_D = 21\,\mu$s, compared with $T_2^* = 7.5\,\mu$s in basic Ramsey protocol, which demonstrates strain-CPMG's effectiveness in reducing effects of inhomogeneous magnetic noise. In the sensing mode, we fix the total free evolution time to 21 μs and monitor signal variations at different locations in the diamond. This is then translated into strain using spin-strain couplings. In the first step, we employ a confocal microscope to limit the interrogation volume to micron scale, and characterize the volume-normalized sensitivity of the method; we obtain an unprecedented volume-normalized sensitivity of $5(2) \times 10^{-8}/\sqrt{\text{Hz}\cdot\mu\text{m}^{-3}}$, surpassing previous work [246] by two orders of magnitude. To map mm-scale areas, we use widefield-imaging QDM because confocal scanning is excessively time-consuming.

Figure 2.8 shows the widefield imaging results. A mm-scale strain map is obtained by

registering multiple fields-of-view of $150 \times 150\,\mu\text{m}^2$ each with one second of data acquisition (Figure 2.8a). We detect strain features of strength $\sim 10^{-6}$ at micron-scale. Large areas of diamond sample with sub-10^{-7} strain variations are observed, indicating promising prospects for diamonds used to detect dark matter. An example of such a low-strain region is shown in Figure 2.8b, and a distribution of one-second pixel Allan deviations is shown in Figure 2.8e. Furthermore, post processing might be performed in order to improve spatially resolving WIMP/neutrino-induced strains; intrinsic strain features can be spatially filtered, for instance, using high-pass filters or with modern machine learning-based methods proposed in similar contexts [197]. Because of the fast decay of the signal, interferometric measurements are less sensitive in pixels with large strain variations. These pixels, for example, can be found near the center or edge of strain features. In order to calculate the amplitude of the interferometry curve, we measure the two quadratures of the interferometry signal (see [295] for details). Figure 2.8d shows an example of how we use this information to identify pixels with high strain gradients.

Since the QDM used for measurements reported in Figure 2.8 does not impose any further depth restrictions beyond the focal plane of the objective, sufficient z-resolution for 3D micron-scale localization remains to be demonstrated. Various methods of achieving z-resolution are envisaged [297]. Well-established optical sectioning methods such as structured illumination microscopy [125] and light-sheet microscopy [248] offer promising pathways, especially since these techniques have already been implemented in NV-diamond systems [231, 486]; another possibility is z-dependent NV control with engineered spatial inhomogeneity of the MW drive [500]. In the assumption of a realized z-resolution, demonstrated strain imaging capabilities in [295] allow for micron-scale localization of WIMP-induced strain within a mm-scale diamond chip after one day of sensing time. Including the experiment overhead time, damage localization can be achieved within the required three-day period.

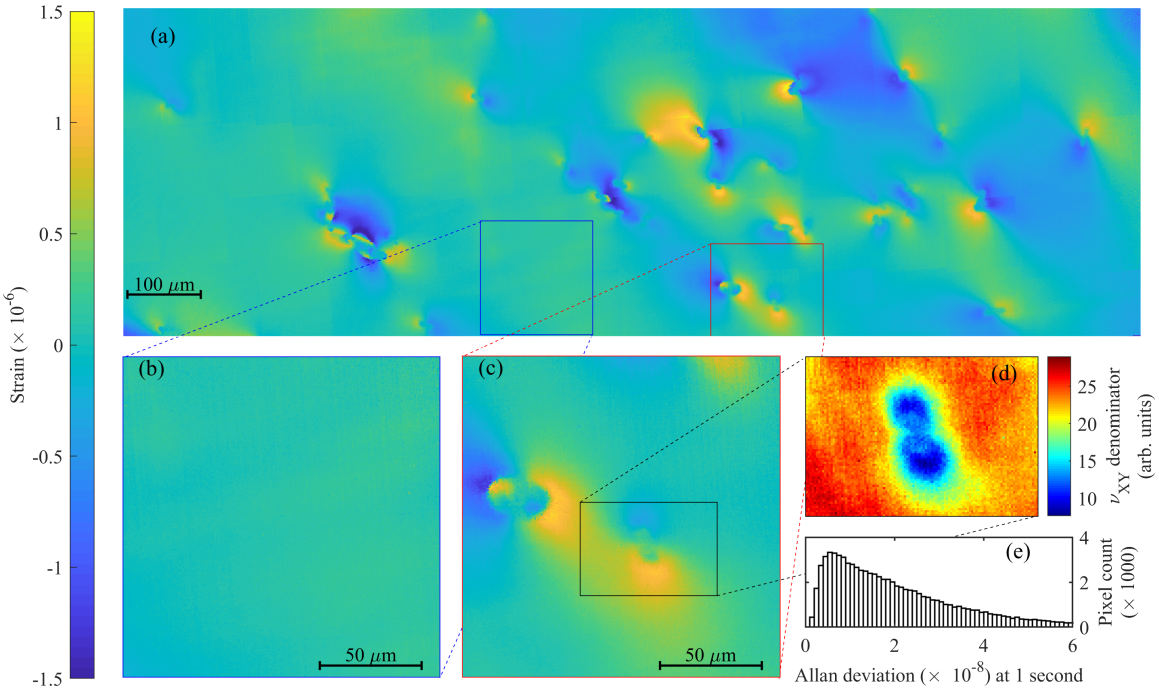

Figure 2.8: Strain map generated with a quantum diamond microscope (QDM) using the strain-CPMG measurement protocol. **(a)** Manually-registered array of multiple $150 \times 150\,\mu\text{m}^2$ strain images, covering a mm-scale area of the NV-diamond sample. Each field-of-view is acquired in one second. Since diamond is an excellent thermal conductor [446], the temperature is constant over the entire sample area for a single measurement, however, temperature drift between multiple measurements causes minor artifacts in the concatenated image. **(b)** An example of a low-strain region. **(c)** Typical intrinsic strain features are detected. **(d)** Interferometry curve amplitude (refer to [295] for definition of the visibility parameter v_{XY}) in a high-strain-gradient region with degraded dephasing time. **(e)** Distribution of the pixel Allan deviation after one second of averaging data in the low-strain region (b). Reproduced from ref. [295].

2.3.2 Fluorescence detection of defect creation

Under high-temperature annealing, diamond lattice vacancies become mobile and can be captured by fixed nitrogen impurities, forming nitrogen-vacancy (NV) centers [37, 122, 143, 216]. This NV center creation mechanism can be utilized to localize the WIMP-induced damage track [297]: WIMP scattering event induces lattice vacancies along with interstitial nuclei; subsequently, high-temperature treatment of the sample helps develop NV centers on-site, which can then be detected through fluorescence microscopy. Fluorescent nuclear track detection using $Al_2O_3 : C, Mg$ crystals [21] is a mature field with applications in oncology/dosimetry [262, 329], as well as nuclear [61], neutron [185], and beam [449] physics. Such fluorescent nuclear track detectors (FNTDs) capture particle tracks in three dimensions through the electronic activation of color centers in the crystal lattice caused by the local electron cascades triggered by particle interactions [328]. However, FNTDs are focused on much longer track lengths than the expected damage length of WIMP events. Fluorescence detection of particle tracks in diamond has also been demonstrated [337]; for example, to study diffusion dynamics of the particle-induced vacancies [338]. Nonetheless, the ability to detect lower energy particles relevant for WIMP recoils remains to be established.

Diamonds of low pre-existing NV concentration and high nitrogen impurity content offer favorable prospects of localizing WIMP damage tracks using NV creation scheme. High concentration of pre-existing NV centers present a confusion background for WIMP-induced NVs. HPHT-grown type Ib diamonds typically contain few vacancies and pre-existing NV centers, while nitrogen concentration can be as high as a few hundred parts per million (ppm) [128, 175]. The initial scans reported in ref. [297] find no more than two NV centers in the diffraction-limited volume (see Figure 2.9). Assuming similar NV background in a scaled up diamond detector material, three NVs created for each WIMP

event is sufficient for diffraction-limited damage track localization. Simulations suggest that each WIMP scattering event results in $\mathcal{O}(10-100)$ lattice vacancies (see Figure 2.6c). However, not all the vacancies form NV centers during the high-temperature annealing – competing processes like recombination of vacancy with an interstitial carbon atom or formation of vacancy clusters reduce the NV yield [37, 143, 216]. In order to determine the minimum detectable recoil energy, NV yield must be characterized for different incident particle energies and annealing parameters. An understanding of NV creation efficiency can be gained from molecular dynamics simulations of induced damage and annealing processes [37]. Additionally, the described characterization can be performed experimentally employing focused ion beam (FIB) systems (see Sec. 2.4).

If damage localization through NV creation proves to be effective, a crucial aspect of this method that needs to be demonstrated is maintaining the directionality and head/tail asymmetry of the damage tracks (see Figure 2.2) during high-temperature annealing process. For the 3D directional information to be retained, vacancy travel range must be less than 10 nanometers since damage track length scale is expected to be several tens of nanometers. Twenty nitrogen atoms are located within the 3 nm travel range in a type Ib diamond with 200 ppm nitrogen concentration; the expected larger than percent level vacancy capture probability [37] suggests minor damage geometry deformation. The amount of directional signal wash-out caused by annealing can be assessed by nanoscale analysis of the damage track induced by single ion implantation before and after annealing. The high nitrogen content in type Ib diamonds may help preserve the head/tail asymmetry, but it reduces the NV coherence time, which negatively affects nanoscale mapping using super-resolution Ramsey-type measurements (see Sec. 2.3.4). Instead, the directionality readout can be achieved by resolving the positions of individual NVs or using x-ray diffraction microscopy [296].

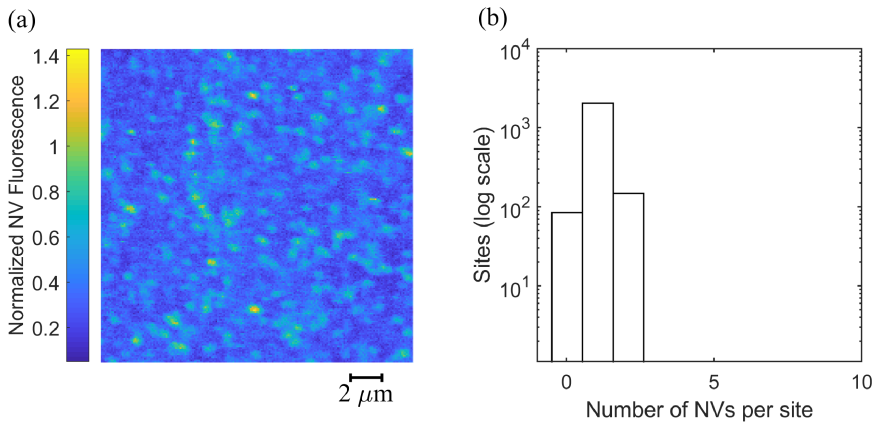

Figure 2.9: Nitrogen-vacancy center background in type Ib HPHT diamonds. The measurements are carried out using a scanning confocal microscope. The number of NVs was then determined based on the normalized intensity of fluorescence at each site. **(a)** A typical field of view illustrating intrinsic NV centers. **(b)** Distribution of pre-existing NV centers in diffraction-limited spots. Approximately $10^4\,\mu\text{m}^3$ volume of diamond from three different samples is scanned. A maximum of two NVs per spot is found. Note that the low-background facilitates fast confocal scanning; with about 100 μm of dwell time, a mm-scale diamond can be scanned within one day. Reproduced from ref. [297].

2.3.3 Hard X-ray diffraction microscopy

Scanning X-ray diffraction microscopy (SXDM) offers a method to map the crystal strain features in 3D at nanoscales [297]. In a recent study [296], using the Hard X-ray Nanoprobe (HXN) at Argonne National Laboratory's Advanced Photon Source [476], we demonstrated the SXDM's capabilities suitable for reconstructing the strain induced by WIMPs on diamond in 3D. HXN uses a monochromatic beam of hard X-rays focused to a spot size of $10-25\,\text{nm}$ [227, 312]. A pixelated photon counter records the spatial pattern of diffracted photons as the spot moves across the sample. These diffraction patterns encode information about local crystallographic deformations [463]. The spot size resolution of about 10 nm is expected to be sufficient for directional signal, but even higher resolutions can be achieved, for example, using Bragg projection ptychography [222, 232, 350].

Figure 2.10 shows a high resolution scan of strain features at about 100 nm scale in

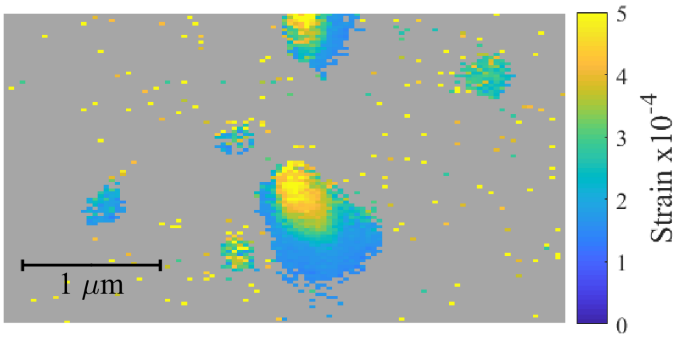

Figure 2.10: In an HPHT sample, strain features at length scale relevant to WIMP signals are detected using SXDM. The results demonstrate SXDM's ability to resolve damage caused by WIMP in diamond crystals. Scanning step size is 22 nm. Reproduced from ref. [296].

an HPHT diamond sample, demonstrating the ability to resolve features with sufficient spatial and strain resolution to detect WIMPs. Using the strain model associated with WIMP-induced vacancies (see Sec. 2.1.3), the expected damage strain from a 10 keV nuclear recoil is 1.8×10^{-4} at a 30 nm spot. Ref. [296] reports a strain sensitivity of about 1.6×10^{-4}. Therefore, the WIMP signal should be detectable. The CVD diamond sample used for this sensitivity analysis includes multi-layer strain structures, which complicate the analysis and possibly reduce the sensitivity. Uniform diamond samples with low strain, ideal for detecting dark matter, can result in up to about an order of magnitude lower strain detection floor. In addition, scanning the crystal from different Bragg angles allows for 3D reconstruction of strain features. In Figure 2.11, intrinsic growth strain features are scanned at two different Bragg angles and 3D reconstructed using a model described in [296]. In summary, SXDM proves its ability to detect directional damage in diamond by combining high spatial resolution, high strain resolution, and 3D reconstruction capabilities.

Preexisting localized sub-micron strain features can be identified as false positive dark matter signals. A nanoscale study of such intrinsic small-scale strain features in CVD diamond samples is crucial for the realization of diamond-based detectors. Figure 2.12 illustrates an initial background search in a limited scanning region. In this survey, we do not

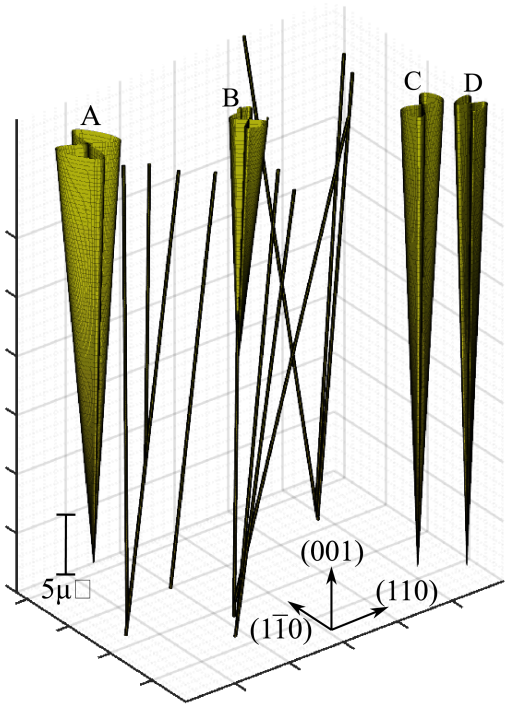

Figure 2.11: Reconstruction of the intrinsic strain features in a CVD diamond in three dimensions. 3D models are constructed using SXDM scans in two (113) and $(\bar{1}13)$ diffraction planes. The illustrated boundary of features correspond to strain 2×10^{-4}. "Rodlike" features are likely the high-strain edges of similar dislocation features with small projections onto both of the diffracting planes. See ref. [296] for details. Reproduced from ref. [296].

find any false positives. We do not see any localized sub-micron features in Figure 2.12a. We detect features in Figure 2.12b that are 100 nm wide, but they extend over a few microns in one dimension. Even though further background characterization is still needed, the results suggest that defect patterns in CVD diamond are either pointlike or extended, thus, distinguishable from WIMP or neutrino signals. The observed defect spatial structure is consistent with those expected of CVD samples treated by high-temperature annealing [189, 353].

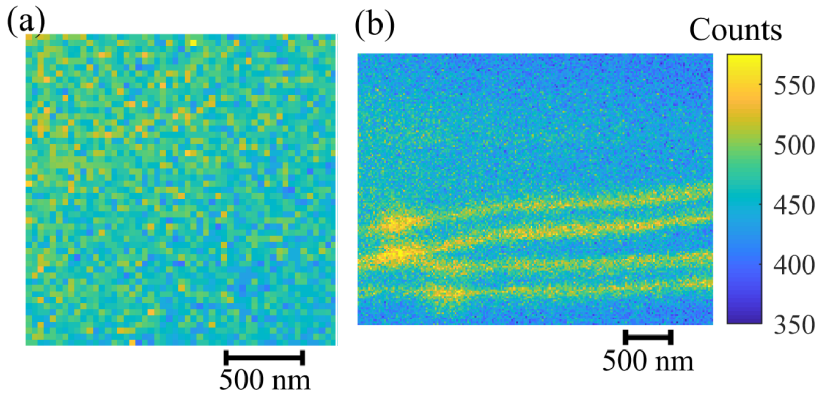

Figure 2.12: In a CVD diamond, small-scale background scans are carried out away from large-scale strain features using SXDM. Results demonstrate that there are no preexisting strain tracks corresponding to the expected WIMP-induced strain features, i.e., localized strain features at $\lesssim 100\,\text{nm}$. Plots show the number of detector counts attributable to strain in the CVD diamond layer. A scanning step size of **(a)** 40 nm and **(b)** 20 nm was used for two different diamond regions. Reproduced from ref. [296].

At present, only a few synchrotron facilities worldwide offer hard x-ray nanobeams with suitable resolution and sensitivity [243, 321, 476]. And high-resolution scans are rather time-consuming. However, with accurate optical localization for candidate WIMP events, the damage track direction for all WIMP events could be determined with a reasonable amount of x-ray beam time. Furthermore, the detector segments would need to be adequately shielded against cosmic rays in transit from the underground detector site to the synchrotron facility.

2.3.4 Superresolution NV microscopy

In addition to hard x-ray diffraction microscopy, superresolution techniques can also be used to resolve directional WIMP tracks below the optical diffraction limits [297, 367]. We summarize the current state-of-the-art in the field and outline a path toward three-dimensional reconstruction of WIMP tracks.

Superresolution techniques are mainly being applied to NV-diamond systems in the context of nanoscale magnetic resonance imaging [82, 83, 390]. By using relevant measurement protocols, such as strain-CPMG, these techniques can be adapted for strain sensing. The first class of techniques uses secondary doughnut-shaped beam spots, superimposed to the Gaussian excitation beam, to suppress signals from everywhere except the low-intensity central region of the doughnut. For example, STED [44, 374, 471] causes stimulated emission depletion under the doughnut; CSD [130, 131] produces NV^- to NV^0 photoionization under the doughnut, which makes them less relevant to sensing; and spin-RESOLFT [240, 302] eliminates the sensing information stored in spins under the doughnut after the sensing protocol has been applied (and before the readout). A second class of methods uses stochastic superresolution microscopy techniques such as STORM [127, 351] and PALM. Nevertheless, stochastic methods appear challenging to use in high-NV density regimes. Finally, gradients of external fields are used to achieve sub-diffraction-limit resolution [40, 79, 495, 496]. A large magnetic gradient over a small region in diamond induces a gradient of Zeeman splittings in NVs distributed within that region; this allows one to spatially resolve NVs using a MW frequency in reference to the induced gradient of resonance frequencies. Magnetic gradients are also used in Fourier magnetic imaging, which utilizes the position information of NV relative to magnetic field gradients encoded in their precession phase and frequency, which is extracted after post-processing the data. Similar to magnetic gradients, MW inhomogeneities has also been demonstrated viable

in reaching sub-diffraction-limit resolution [500]. In Table 2.1, we summarize the results reported on superresolution techniques in NV-diamond systems.

Method	Resolution	Modality	Ref.
STED	$\sim$ 10 nm	Real space, Scanning	[374]
SIL-STED	$\sim$ 2.5 nm	Real space, Scanning	[471]
CSD	$\sim$ 4 nm	Real space, Scanning	[131]
spin-RESOLFT	$\sim$ 20 nm	Real space, Scanning	[240]
STORM	$\sim$ 25 nm	Real space, Widefield	[351]
Magnetic gradient	$\sim$ 30 nm	Fourier space, Widefield	[40]
Magnetic gradient	$\sim$ 30 nm	Real space, Widefield	[496]
MW gradient	$\sim$ 100 nm	Real space, Widefield	[500]

Table 2.1: Superresolution techniques demonstrated in NV-diamond sensing. STED: stimulated emission depletion. SIL: solid immersion lenses fabricated directly in the diamond. CSD: charge state depletion. RESOLFT: reversible saturable optical linear fluorescence transitions. STORM: stochastic optical reconstruction microscopy.

All of the methods discussed achieve or approach the benchmark resolution of 20 nm needed to detect directionally oriented WIMP signals. The demonstrations, however, have been limited to thin NV layers or samples with sparse NV centers, passively imposing 3D resolution. In order to adapt these techniques for WIMP track reconstruction, it is important to integrate depth-resolution into any of the methods. The 3D analogue of doughnut-shape illumination has been attempted, reaching about 100 z-resolution [215, 487]. However, the high index of refraction of diamond might impede further progress in this route for achieving 3D resolution of 20 nm.

For the reconstruction of the WIMP-induced strain in three dimensions, we propose a combined technique: STED, CSD, and spin-RESOLFT methods can be used for achieving lateral resolution, while simultaneous magnetic field gradients can be used for achieving depth resolution [297]. Figure 2.13 illustrates this scheme. Using this combination method, it is estimated that it will take about 11 hours to scan a 1 μm^3 volume with 10 nm resolution [297]. In addition, to avoid complications of mapping out the damage track deep in the diamond, fast and low-strain etching methods [189, 221, 318] can be employed to have the

damage track closer to the surface instead of deep in the bulk. Spectroscopic methods such as spin-RESOLFT and Fourier imaging require good quantum coherence properties that are present in CVD diamond but not commonly in HPHT diamond samples. Therefore, the proposed combined method may not be applicable to HPHT samples with high nitrogen content in the detection scheme based on NV creation (see Sec. 2.3.2). However, due to low initial density of NVs, it will be possible to directly resolve created NV centers. In summary, state of the art in superresolution imaging using NV centers suggests a promising path for 3D damage reconstruction in either scheme of the detector, i.e., localization using strain spectroscopy (see Sec. 2.3.1) or localization using creation of NV centers (see Sec. 2.3.2).

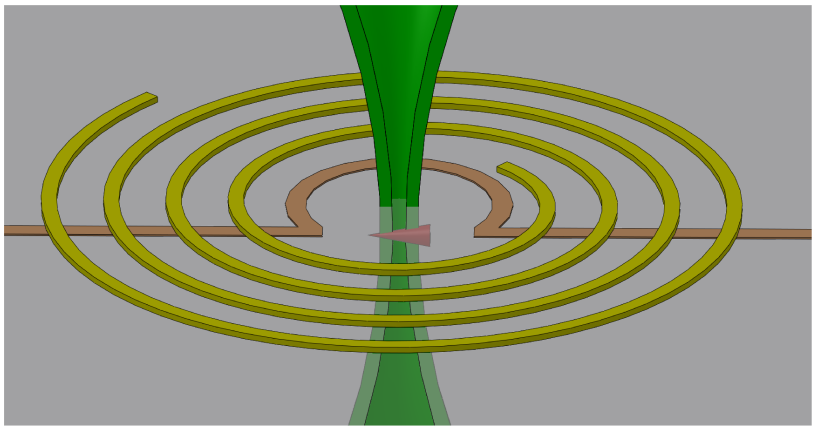

Figure 2.13: Illustration of the combined method proposed for superresolution NV strain spectroscopy. A doughnut-shaped illumination provides lateral resolution through STED, CSD, or spin-RESOLFT. Fabricated gradient coils produce magnetic field gradients that provide depth resolution. An Ω-shape waveguide for microwave delivery is also illustrated. Reproduced from ref. [297].

2.4 Sensitivity characterization via single ion implantation

Thus far, we have discussed methods that enable the localization of WIMP and neutrino damage tracks and retrieval of the directional information encoded in the track geometry

and orientation. Here, we present a method to generate injected signals that can be used to determine the directional sensitivity of the detector.

State-of-the-art focused ion beams (FIB) offer single ion number resolution, low-energy ions, high spatial resolution, as well as high mass resolution [343]. In the ion implanter at Ion Beam Laboratory (IBL) at Sandia National Laboratories (SNL), the ions are extracted from liquid metal alloy ions sources (LMAIS), which allows working with a third of the atoms in the periodic table. Electrostatic ExB filters incorporated in the setup provide mass resolution of $M/\Delta M > 61$. A fast beam-blanker is implemented with a minimum pulse time of about 16 ns. Lastly, the electrostatic objective lens provides submicron ion beam spots [343]. The combination of these features makes this setup a suitable platform for generating single-particle-induced damage tracks in diamond, simulating WIMP recoil tracks.

With fast beam blanking, pulsed ion implantation can achieve low ion numbers. In spite of this, as the number of ions in a fixed pulsed time is determined by Poisson statistics, there is large relative uncertainty regarding the number of ions in a pulse at low ion counts. In situ ion counting is a method developed to overcome the Poissonian uncertainty [8, 75, 238, 343, 398, 439]. In this method, illustrated in Figure 2.14, metallic pads with a separation of about 10 microns are fabricated on the sample surface. Ion beams are focused on the gap between the pads. During the implantation, the pads are biased with a DC voltage and are connected to a collection circuit for monitoring the charge generation due to ion implantation, i.e. ion-induced electron-hole production. The following method uses a charge collection system to achieve precise single ion implantation. Based on the beam-off charge readout, a lower threshold for the collection circuit voltage is defined. The mean ion number per pulse during the implantation is set to a small number (e.g., $\langle \mathrm{ionnumber/pulse} \rangle \lesssim 0.1$). Poisson distribution suggests that there are mostly zero ions per pulse, but occasionally there are one or more (but mostly one ion). As the implantation

continues pulse by pulse at the same site, the readout voltage is monitored and compared to the pre-determined threshold. As soon as the voltage passes the threshold, implantation is stopped at that site. Besides threshold-based implantation, the full distribution of ion-induced voltage can also be used in post-processing to reduce the ion-number uncertainty [439]. A recent example is the use of this method for silicon implantation on diamond with a 5% ion number error [439].

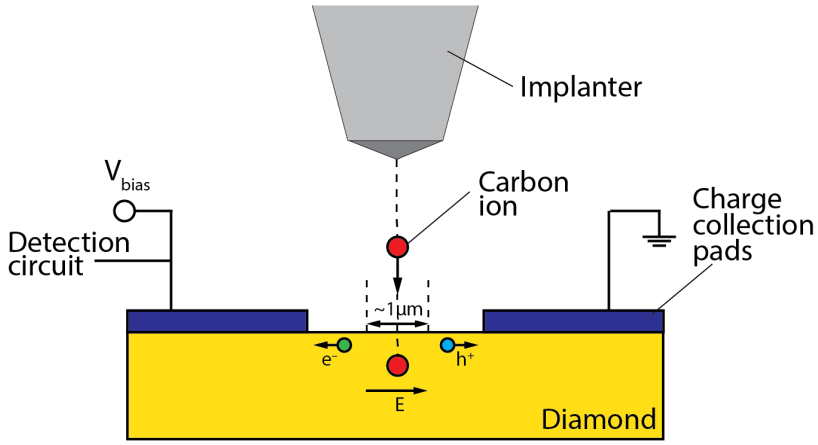

Figure 2.14: Illustration of the single ion implantation experiment using in situ ion counting method. The produced electron-hole pairs are collected under a DC bias voltage through the fabricated pads.

We propose using single carbon ion implantation experiments to generate WIMP-like signals in diamond. The implanted ion will bounce off of native diamond lattice atoms initiating nuclear recoils, much like the initial recoil of the carbon atom caused by WIMP or neutrino interactions. The single-ion implantation can be used to test both methods of localization described in Sections 2.3.1 and 2.3.2. For NV-based strain spectroscopy, the implantation will take place in a high-quality CVD diamond with an ensemble of NV centers. The ion-induced strain signal can then be examined and detector efficiency can be determined as a function of implantation energy (corresponding to recoil energy, thus the WIMP mass). For NV creation, an HPHT diamond sample with low NV density and

high nitrogen density will be used. During high-temperature annealing, some ion-induced vacancies will combine with the nitrogen atoms, forming NV centers that can be detected with NV fluorescence microscopy. The use of such an experimental method will provide insight into NV creation efficiency and the effects of annealing on initial damage track distortion.

2.5 Summary and outlook

Objective. Results from upcoming generations of WIMP detectors are likely to approach the "neutrino floor", where coherent scattering of low-energy neutrinos will be detected [1, 2, 38]. Like WIMPs, neutrinos induce nuclear recoils in a target. They scatter at energies relevant to WIMP searches, meaning standard background discrimination techniques cannot reject them. Without discrimination between WIMP and the neutrino events, identifying WIMPs below the neutrino floor will require detecting annual modulation atop the neutrino background, demanding dozens of events to achieve a improved discovery limit. As the direction of incoming particles could be detected, solar neutrinos would be rejected in the early stages of a directional WIMP detector [211, 303, 335, 451, 453], and other astrophysical and terrestrial neutrinos in the later stages as they become relevant in higher exposures. Further, a directional detector would reveal a WIMP signal's cosmological origin, and potentially improve our understanding of local dynamical DM structures [266, 336]. A solid-state directional detector is especially attractive for probing WIMP cross-sections below the neutrino floor. Their high target density contrasts well to existing directional detection methods with gaseous and emulsion targets. Further, the proposed solid-state detector concept yields both timing information as well as complete three-dimensional information via head/tail asymmetric signals [297, 367] (similar to the well-developed gas TPC detectors.)

Detector principle. Wide-bandgap semiconductors such as diamond [270] and silicon carbide [210] have been proposed as a target for solid-state WIMP detection. Their good semiconductor properties and lower-mass nuclei provide an advantageous sensitivity profile compared to existing detectors. These materials can be lab-grown with high purity and homogeneous crystal structure [189, 189, 298]; a WIMP event in such a crystal would leave a characteristic track of damage, with the crystal acting as a "frozen bubble chamber" recording the direction of the incident particle [297, 367]. The crystal damage track results from the cascade of secondary nuclear recoils initiated when a WIMP (or neutrino) impacts a target nucleus; simulations for a diamond target indicate measurable orientation and head/tail asymmetry down to 1–3 keV of recoil energy [367]. The shape and orientation of this damage track can be read out via spectroscopy of quantum point defects in the crystal such as nitrogen-vacancy (NV) [58, 166, 282, 390] and silicon-vacancy (SiV) [306] defects in diamond, and divacancies [447, 479] in silicon carbide.

A directional detector based on solid-state point defects in a semiconductor could take advantage not only of a large target mass, but also of intensive development of instrumentation for WIMP detectors based on silicon or germanium [18, 290, 371, 444]. Detector segments could be instrumented with charge or phonon collectors such as transition edge sensors, or scintillation photons could be collected from the detector bulk. When a crystal segment triggers one of these detection methods, it would be removed from the detector for directional analysis, while the remainder of the detector continues to accumulate exposure (Sec. 2.1.3).

Damage tracks from WIMP events will be tens or hundreds of nanometers long [367], requiring a two-step process to extract the directional information [297]. Fortunately, both steps can be built upon techniques established in the fields of solid-state quantum sensing and quantum information processing. First, diffraction-limited optics can be used to resolve the position of the damage track to a sub-micron voxel within the millimeter-scale detector

segment (sections 2.3.1 and 2.3.2). Second, optical superresolution techniques (Sec. 2.3.4) or high-resolution x-ray nanoscopy (Sec. 2.3.3) can be used to measure the damage track structure at the nanometer scale.

Directional readout technologies. Initial simulations and experimental demonstrations of these techniques have focused on the NV centers in diamond, as it is the most widely used and best-characterized quantum emitting defect [58]. Consisting of a lattice site vacancy adjacent to a substitutional nitrogen defect, the NV is a spin-1 system featuring optical initialization and readout, and a microwave transition frequency sensitive to local crystal strain (as well as magnetic and electric fields, and temperature); see Sec. 2.2. The damage track from a WIMP-induced recoil cascade would induce significant strain on nearby NV centers, which can be measured via shifts in their spin transition frequencies. Diffraction-limited strain imaging (Sec. 2.3.1) could be used to localize damage tracks at the micron scale; sensitive, widefield strain imaging has been the subject of much recent work [95, 246, 295]. Superresolution microscopy and spectroscopy using NV centers (Sec. 2.3.4) has been extensively developed as well. Spatially-resolved, subdiffraction strain sensing is a plausible avenue for nanoscale readout of damage track direction. These same methods are applicable to other color centers in diamond such as the silicon-vacancy center, or to divacancies in silicon carbide.

Alternatively, defects can be created from recoil-induced lattice site vacancies generated during a WIMP interaction with the diamond (Sec. 2.3.2). A nitrogen-rich diamond could be annealed to induce these vacancies to form new NV centers or other color centers. In crystals with few pre-existing emitters, this represents a near-background-free method of damage track localization. The direction can then be extracted either via strain spectroscopy of the created color centers, or by superresolution spatial mapping of the defect positions. Scanning X-ray nanobeam diffraction measurements (Sec. 2.3.3) present a non-defect-based method for damage track direction measurement – instruments at synchrotron

facilities can detect strains at the level predicted for a WIMP damage track, and can be performed with nanometer spatial resolution.

All of the techniques outlined above require that optical measurements be performed on-site to avoid cosmic ray exposure during transit. The low cost and simplicity of the setups for these measurements enable multiple of them to be used in parallel. Additionally, detector segments may require etching to bring the damage track close to the surface for nanometer-scale measurements, but appropriate techniques enable this without introducing additional strain or distorting the WIMP signal [189, 221].

Outlook. In the near term, the work towards such a solid-state WIMP detector with directional sensitivity will be centered around demonstrating the capability to locate and determine the direction of nuclear recoil damage tracks in diamond. This requires adaptation and development of existing techniques, but the current state of the art is not far from the requisite sensitivity and resolution. In particular, our recent work on widefield strain imaging in diamond via NV spectroscopy [295] as well as scanning X-ray diffraction microscopy of nanoscale strain mapping [296] demonstrate the sensitivity required for directional detection. For concrete experimental characterization of the efficiency of these methods, injected nuclear recoil signals can be generated using single ion implantation (Sec. 2.4).

In the medium term, such a detector will require instrumentation of a prototype detector. Such prototype would feature low-threshold charge, phonon, or photon collection capabilities with spatial resolution at the millimeter scale. Development of crystal growth techniques to create large volumes of structurally homogeneous crystals is also required. Modern diamond growth techniques using chemical vapor deposition (CVD) enable repeatable, fast, and low-cost growth of uniform crystals; a reasonable progress in this field expected in the next decade should allow for the production of the volume of diamond material required for WIMP detection. With appropriate development and synergy between

multiple disciplines, the proposed approach offers a viable path towards directional WIMP detection with sensitivity below the neutrino limit.

Chapter 3: GALILEO: Galactic Axion Laser Interferometer Leveraging Electro-Optics

The nature of dark matter (DM) in modern physics remain elusive. A well-motivated class of DM candidates is light bosonic particles. The QCD axion, for example, is a viable candidate for DM [4, 151, 228, 293, 355] in addition to solving the Strong CP problem [346, 466, 470]. Axion-like pseudoscalar particles [228, 293] (a generalized form of the QCD axion) and vector particles (e.g., a dark or hidden photon) [111, 174] are similarly well-motivated DM candidates. Such new particles typically have suppressed interactions with the standard model, which nevertheless can be used to search for them in the laboratory [14, 111, 366, 400, 412, 428].

Light DM is also referred to as wave-like, in contrast to heavier particle-like DM candidates. Due to the high occupancy number of such particles at galactic scales, light DM behaves as a classical wave. Such a DM background can be modeled as a classical random field $a_0 \cos(\omega t + \mathbf{k}\cdot\mathbf{x} + \phi)$ [1], where $a_0 = \sqrt{\rho_{\rm DM}}/m_{\rm DM}$ is the field amplitude given by the DM density $\rho_{\rm DM}$ and mass $m_{\rm DM}$; $|\mathbf{k}| \simeq m_{\rm DM} v$ is the wave number; and ϕ is a random phase. The characteristic frequency of the random field's oscillations is given dominantly by the DM mass, with corrections from the kinetic energy, as $\omega \simeq m_{\rm DM} + m_{\rm DM} v^2/2$, where $v \sim 10^{-3}$ is the virial velocity in the Milky Way. The light DM field is therefore coherent over spatial separation $\lambda_{\rm c} \sim (m_{\rm DM} v)^{-1}$ and over a time scale $\tau_{\rm c} \sim (m_{\rm DM} v^2)^{-1}$, expressed

[1] The oscillatory field will also have a direction if the DM is a vector like dark photon.

in natural Planck units [186].

Several experimental programs are underway or proposed to probe the parameter space of light DM, with different methods sensitive to specific couplings to standard model physics and a particular range of DM masses. Interactions with the standard model gluons and fermions can be probed via measuring its induced oscillatory electric dipole moments (EDMs) [6, 383, 396], as well as secondary effects of an oscillatory EDM in precision experiments such as storage rings [24, 124, 245, 250, 356], nuclear magnetic resonance [47, 99], molecular and atomic spectroscopy [204, 249], among others [45, 72]. Light DM candidates generically couple to electromagnetism as well, which can be investigated using high-precision methods including resonant cavity haloscopes [23, 49, 60, 119, 123, 242, 272, 308, 362, 435], lumped elements [97, 137, 205, 386], among others [71, 339, 378].

Our lack of knowledge about the nature of DM makes it imperative to probe a wide range of DM parameter space. In addition, different scenarios of cosmological production of the observed DM abundance suggest a wide range of viable masses. For instance, the QCD axion is produced as the pseudo-Nambu-Goldstone boson of spontaneous breaking of the global Peccei-Quinn (PQ) symmetry [228, 293]. Importantly, the QCD axion mass that could serve as DM critically depends on whether the PQ symmetry breaks during inflation or after. Post-inflationary production of the axion serving as DM in principle predicts a unique mass. Even so, it is challenging to solve axion cosmology accurately – topological defects contribute to axion production on top of the misalignment production, making the dynamics highly nonlinear. Analytical calculations and simulations predict a post-inflationary QCD axion mass that ranges from tens to hundreds of μeV [54, 70, 80, 84, 102, 150, 251], with more recent simulations suggesting a narrower range of approximately $40-180\,\mu$eV [101]. A QCD axion with even lower masses are feasible via production pre-inflation and could also serve as DM.

Resonant microwave cavity haloscopes have been the leading DM detectors for $m_{\rm DM} \sim$

μeV, achieving sensitivity to the QCD axion. However, due to the rapidly diminishing scanning rate caused by a decreasing signal-to-noise ratio (SNR) at smaller cavity volumes [14], it is challenging to probe masses above a few tens of μeV with such detectors. Despite this technical limitation, ongoing efforts are being made to further optimize microwave cavity haloscopes and explore this higher-mass DM parameter space [107, 288, 305], mainly motivated by the post-inflationary axion production as discussed above.

In this Letter, we propose a new approach to detect both axion and dark photon DM over a wide mass range, approximately from $0.1 - 10^3\,\mu$eV. The basic principle is as follows. Nonlinear electro-optical materials respond to the electric field induced by a coherently oscillating light DM background: the material's refractive index thereby acquires oscillatory corrections. We outline a resonant readout scheme based on laser interferometry to detect such DM-induced signals (Fig. 3.1); see also Refs. [149, 176, 287, 300, 309, 319, 331, 340, 365] for other interferometry-based DM detection proposals. A Michelson interferometer using a nonlinear electro-optical material in *only* one arm will exhibit an oscillatory differential optical phase between its two arms, imprinted in the measured interferometry fringes. We refer to this experimental approach as GALILEO: Galactic Axion Laser Interferometer Leveraging Electro-Optics. In the following, we present projected sensitivities for this measurement scheme for both the axion and dark photon DM parameter spaces, and compare to the current state of the art (Fig. 3.2). Note that for the light DM mass range considered here, the induced oscillations in material refractive index and hence interferometer output signal are in a frequency range $\sim 100\,$MHz to 1 THz; and the light-DM background field is coherent over $\lambda_c \sim 1\,$cm to 100 m and $\tau_c \sim 0.1\,\mu$s to ms.

3.1 Electro-optic effect

Light-DM-induced electric fields can be detected via interactions that modulate an electro-optical (EO) material's properties. In particular, the presence of an external electric field results in a change in the polarization of the material, which then modifies the dispersion relation of the electromagnetic wave inside the material. Therefore, one can detect ambient electric fields, such as that induced by light DM, by measuring the effect on propagation of a probe laser through an EO material [485].

This scheme requires a nonlinear response of the material that couples the probe laser and the light-DM-induced electric field to be sensed, $E_{\rm DM}$. This property can be found in electro-optical materials, where the polarization is given by $P = \varepsilon_0 \chi^{(1)} E + \varepsilon_0 \chi^{(2)} E^2 + \mathcal{O}(E^3)$ [354]. Here, ε_0 is the vacuum permittivity and $\chi^{(n)}$ is the n-th order electric susceptibility of the material [2]. We define an effective electric susceptibility as follows: $\chi_{\rm eff.} = \chi^{(1)} + \delta\chi$, where $\delta\chi = \chi^{(2)} E_{\rm DM}$. Since the effect of DM is expected to be small, one can treat the additional term $\delta\chi$ perturbatively. The electric susceptibility $\chi_{\rm eff.}$ is used to calculate a medium's refractive index via $n = (1+\chi_{\rm eff.})^{1/2}$. Therefore, in the presence of non-zero $E_{\rm DM}$ we have a correction to the material's refractive index proportional to the light-DM-induced electric field $n = \bar{n} + \delta n$, where $\bar{n} = (1+\chi^{(1)})^{1/2}$ and $\delta n \simeq \delta\chi / 2\bar{n}$. We calculate this DM-induced refractive index correction for a given set of DM parameters and material properties.

Electro-optic properties due to $\chi^{(2)}$ (i.e., the Pockels effect) can be observed in crystals lacking inversion symmetry. These materials are typically used for applications that employ modulations of the refractive index to achieve fast optical switching and frequency conversion. A widely used example of such a crystal is lithium niobate ($LiNbO_3$) [456, 467],

[2] Note that this equation is written in a schematic form and that it must be computed using proper scalar products.

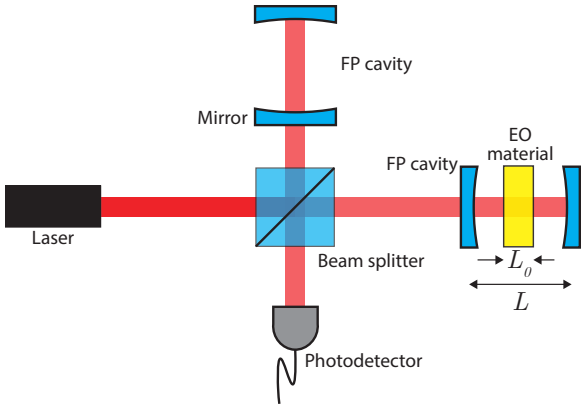

Figure 3.1: Schematic of the proposed laser interferometer-based light dark matter (DM) detector, GALILEO. The Fabry-Perot (FP) cavities are resonant with the light-DM mass $L = 2n\pi/m_{\rm DM}$. The electro-optical (EO) material's thickness is limited to $L_0 \leq \pi/m_{\rm DM}$ to preserve the oscillatory DM signal while averaging over laser travel time through the material. Note that the EO material needs to be exposed to a large, uniform magnetic field for axion-induced effects. See text for details.

while barium titanate ($BaTiO_3$) is an emerging material with a higher Pockels coefficient [7, 170]. We use these two crystals as benchmarks for the light-DM detector material in our interferometry measurement scheme. The Pockels coefficient r is defined such that the modulation in the refractive index due to an applied electric field is $\delta n = \bar{n}^3 r E/2$. Note that r is a tensor quantity, with its largest component being about 31 pm/V [467] (923 pm/V [7]) for $LiNbO_3$ ($BaTiO_3$). Therefore, we have:

$$\delta n \sim \begin{cases} 1.8 \times 10^{-10}\,(\mathrm{m/V})\; E_{\rm DM}, & \text{for } LiNbO_3 \\ 6.4 \times 10^{-9}\,(\mathrm{m/V})\; E_{\rm DM}, & \text{for } BaTiO_3 \end{cases} \tag{3.1}$$

where we used $\bar{n} = 2.3$ for $LiNbO_3$ and $\bar{n} = 2.4$ for $BaTiO_3$.

3.2 Dark matter-induced electric field

We first consider axion DM coupling to photons:

$$\mathscr{L} \supset -\frac{g_{a\gamma\gamma}}{4} a F_{\mu\nu}\tilde{F}^{\mu\nu} = g_{a\gamma\gamma} a \mathbf{E}\cdot\mathbf{B} \tag{3.2}$$

where a and F are the pseudoscalar axion field and electromagnetic field strength, respectively. This interaction modifies Maxwell's equations. In particular, the axion field generate oscillatory electric and magnetic fields in the presence of a large bias magnetic field B_0. When the Compton wavelength of the axion $2\pi/m_{\rm a}$ is smaller than the physical size of the magnet, the axion-induced electric field is given by $E_{\rm a} \sim g_{a\gamma\gamma} a B_0$ [73, 341]. Therefore, we have:

$$\begin{aligned} E_{\rm a} \simeq 5.6\times 10^{-9}\,\frac{\rm V}{\rm m}\left(\frac{g_{a\gamma\gamma}}{10^{-10}\,{\rm GeV}^{-1}}\right)\left(\frac{\rho_\odot}{0.45\,{\rm GeV/cm^3}}\right)^{1/2} \\ \times\left(\frac{m_a}{100\,\mu{\rm eV}}\right)^{-1}\left(\frac{B}{10\,{\rm T}}\right) \end{aligned} \tag{3.3}$$

For dark photon DM, we consider the kinetic mixing Lagrangian term:

$$\mathscr{L} \supset -\frac{\kappa}{2} F_{\mu\nu} F'^{\mu\nu} \tag{3.4}$$

where κ is the dimensionless mixing parameter and F' is the dark photon field strength. The light-DM-induced electric field due to this mixing term is $E_{\rm d.p.} \sim \kappa\sqrt{\rho_\odot/\varepsilon_0}$. Therefore, we have:

$$E_{\rm d.p.} \simeq 2.8\times 10^{-8}\,\frac{\rm V}{\rm m}\left(\frac{\kappa}{10^{-11}}\right)\left(\frac{\rho_\odot}{0.45\,{\rm GeV/cm^3}}\right)^{1/2} \tag{3.5}$$

3.3 Detection scheme

We propose using an asymmetric Michelson interferometer, where the sensing volume of the EO material is placed in one arm but not in the other; see Fig. 3.1. Due to the modulated refractive index, the probe laser will experience a modulated phase velocity as it propagates through the EO material according to $\delta v = -\delta n/\bar{n}^2$. The differential phase velocity between the two arms, integrated over the length of the material, leads to an effective differential arm length $\delta L = \int \mathrm{d}t\, \delta v = -\delta n L_0/\bar{n}$. Hence, the interferometer output will oscillate with the light-DM oscillation frequency.

Interferometer arms can be equipped with a Fabry-Perot (FP) cavity to further increase the sensitivity via increasing the effective integration length as $L_{\rm eff} = L_0 N \mathscr{F}$, where L_0, N, and $\mathscr{F}$ are the EO material's thickness, number of EO material pieces in the cavity, and finesse of the FP cavity. In order to not average over DM oscillations as the laser beam travels through an EO material of thickness L_0within a FP cavity of length L, we require that $L_0 \leq \pi/m_{\rm DM}$ and $L = 2n\pi/m_{\rm DM}$, in natural Planck units, where n is an integer number. We note that in this case, the FP cavities are in resonance with the DM mass and the signal enhancement is due to the laser light traveling repeatedly through the EO material rather than enhancing the DM-induced electric field or the laser amplitude.

Ultra-high-finesse FP cavities with $\mathscr{F} \sim 1.5 \times 10^5$ are developed for precision experiments [316, 327, 360]. Also, FP cavities can achieve Q-factors $\gg 10^6$ via extending the cavity length, despite a lower finesse [142, 146]. Therefore, it is feasible to include multiple EO materials separated by $2\pi/m_{\rm DM}$ in a single cavity. The effective travel length through the total amount of EO material is ultimately limited by laser absorption. The absorption coefficient for pure, high-Q nonlinear crystals (including $LiNbO_3$ [279]) is about $10^{-5}\mathrm{cm}^{-1}$, i.e., $\mathscr{O}(1)$ fraction of the laser power gets absorbed after about 1 km of traversing inside the EO material. Therefore, we set an upper limit on $L_{\rm eff} \leq 1\,\mathrm{km}$. Reflection

from crystal surfaces is a potential challenge to achieve ultra-high-finesse cavities [169]. However, in our proposed scheme the separations between EO materials and cavity mirrors are set to be multiples of $\pi/m_{\rm DM}$, in which case the reflected and transmitted light have the same phase, and therefore the effect of reflection on the cavity finesse can be minimized. Alternatively, high quality anti-reflection coatings can be used to improve the cavity finesse [494] when there are practical restrictions on the material length such that $L_0 \neq \pi/m_{\rm DM}$.

Before moving on to computing signal-to-noise (SNR) values for this measurement scheme, we provide the transfer function that relates the light-DM-induced modulation of the refractive index (3.1) to the interferometer output signal power:

$$\frac{\delta P_{\rm out}}{\delta n} = \frac{\delta P_{\rm out}}{\delta L}\frac{\delta L}{\delta n} = \frac{2\pi}{\lambda \bar{n}} P_{\rm in} L_0 N \mathscr{F} \tag{3.6}$$

where, we used $\delta P_{\rm out}/\delta L = (2\pi/\lambda) P_{\rm in} N \mathscr{F} \sin(8\pi\Delta L/\lambda)$ in the second equality [106]. Here, λ is the laser wavelength and ΔL is a DC offset between the two arm lengths, which we choose such that $\delta P_{\rm out}/\delta L$ is maximum, thereby giving optimal sensitivity to a light DM background.

3.4 Experimental feasibility

Quantum noise and thermal noise are the fundamental sources of noise in the described interferometer measurement scheme. Here, we estimate these two noise sources and show that the proposed experiment can reach the quantum noise limit for experimentally feasible parameters. Technical noise mitigation (such as laser frequency and phase noise, as well as EO material birefringence [145]) is also an important aspect of the final detector, which can benefit from well-established techniques used in state-of-the-art high-precision laser interferometers like LIGO [3, 104, 105]. We leave a detailed description of the detector

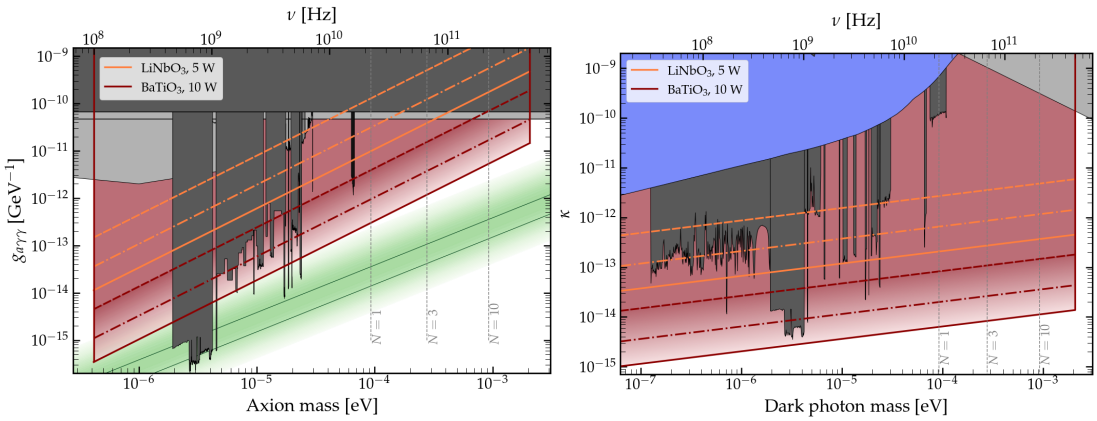

Figure 3.2: Projected sensitivities of the GALILEO experiment for axion (*Left*) and dark photon (*Right*) dark matter searches. The red shaded area is within the reach of the proposed detector. Orange (red) lines: $LiNbO_3$ ($BaTiO_3$) as target electro-optical material. Dashed lines: 1 s averaging at each frequency band $\Delta f = m_{\rm DM}/(2\pi\mathscr{F})$. Dash-dotted lines: extended search time of 290 s per bin, equivalent to scanning a decade in mass for about 3 years. Solid lines: 290 s averaging time per bin and 10 dB squeezing of light input to the interferometer. Vertical gray dashed lines indicate the number of EO material pieces $N = 1, 3$, and 10 needed to achieve maximum sensitivity at representative DM masses if each EO material has a thickness of $L_0 = \pi/m_{\rm DM}$. See text for details. Dark (light) gray shaded areas are excluded by terrestrial experiments (astrophysical observations). Green: QCD axion parameter space. Blue: excluded by dark photon DM cosmology [41]. Existing limits are adapted from ref. [333].

design for a follow-up study. We next discuss the sources of quantum and thermal noise.

Photon counting (shot) noise is the fundamental quantum-mechanical limit of a laser interferometer [117]. The number of detected photons follows Poissonian counting statistics, which leads to an output power uncertainty of $\delta P_{\text{out}} = \hbar\omega_{\text{L}}\sqrt{N_{\text{out}}}/\tau$, where ω_{L} is the carrier photon frequency and N_{out} is the number of detected photons in the output port over integration time τ. The shot noise amplitude spectral density (ASD) is $\delta P_{\text{out}}/\sqrt{\Delta f}$, with Δf being the bandwidth, which can thus be expressed as:

$$\text{ASD}_{\text{s.n.}} = \sqrt{2\hbar\omega_{\text{L}} P_{\text{out}}} = \sqrt{\hbar\omega_{\text{L}} P_{\text{in}}}\,. \tag{3.7}$$

The second fundamental noise source is thermal noise, which has been extensively studied in the context of gravitational wave laser interferometers [91, 92, 159, 173, 281]. There are several mechanisms that contribute to the total thermal noise. Homogeneous damping within a material, which is characterized by the imaginary component of Young's modulus, induces interferometer phase noise through elastic deformations of the material. In the presence of inhomogeneous/space-dependent temperature variations, heat flow leads to entropy redistribution and therefore energy dissipation and thermal noise. Such temperature variations can arise from temporal, stochastic fluctuations at a finite temperature or from the photo-thermal effect, i.e., photon absorption inside the material. These fluctuations induce interferometer phase noise via the thermo-elastic effect (due to a non-zero thermal expansion coefficient) and the thermo-refractive effect (due to a non-zero refractive index). We estimate each of the noise sources using the fluctuation-dissipation theorem (FDT); we find that photon shot noise dominates over thermal noise for temperatures around 200 K and below. This operational temperature can be achieved even with a few watts of laser absorption (and therefore heat generation) via active cooling feedback [407].

3.5 Thermal noise sources

The fluctuation-dissipation theorem (FDT) allows thermal noise contributions to a GALILEO measurement to be characterized according to the associated loss mechanism. Before estimating various noise contributions, let us briefly review the FDT. The temperature-dependent fluctuations of the effective interferometer arm length difference (i.e., effective displacement) z as our observable can be written as:

$$\delta z = \mathscr{A} \int \mathrm{d}^3\mathbf{r}\ \delta T(\mathbf{r}) q(\mathbf{r}) \tag{3.8}$$

where $q(\mathbf{r})$ is a space-dependent form factor and $\mathscr{A}$ is a coefficient that relates temperature to the observable of interest z. In this work, the form factor is proportional to the laser beam intensity profile in the transverse plane and is assumed constant along the beam line, i.e.,

$$q(\mathbf{r}) \propto I(x,y) = \frac{1}{\pi R_{\mathrm{beam}}^2} e^{-(x^2+y^2)/R_{\mathrm{beam}}^2}\,. \tag{3.9}$$

with R_{beam} being the Gaussian width of the optical beam intensity profile.

We are interested in calculating the noise power spectral density (PSD) $S_{\delta z} = \langle \delta z(\omega) \delta z^*(\omega) \rangle$ where ω is an arbitrary frequency within the range of light-DM masses relevant for the detector. According to FDT, one performs the following steps for each relevant loss mechanism:

- Assume a periodic, local entropy injection $\delta s_{\mathrm{inj}}(r)$ to the measurement system, with a density of

$$\frac{\delta s_{\mathrm{inj}}(\mathbf{r})}{\delta V} = \frac{1}{T}\frac{\delta Q_{\mathrm{inj}}(\mathbf{r})}{\delta V} = F_0 \cos(\omega t) q(\mathbf{r}) \tag{3.10}$$

  where δQ_{inj} is the injected heat/energy, and T is the mean temperature. If z has dimensions of length, then F_0 has dimensions of force, with a magnitude set by the

specific loss mechanism being considered.

- Calculate the dissipated power W_{diss} associated with each loss mechanism considered.

- Compute the the noise PSD for each loss mechanism via

$$S_{\delta z}(\omega) = \mathscr{A}^2 \frac{8k_B T}{\omega^2} \frac{\langle W_{\text{diss}} \rangle}{F_0^2} \tag{3.11}$$

where k_B is the Boltzmann constant and $\langle \cdots \rangle$ denotes time-averaging over one cycle with period $2\pi/\omega$.

Parameter	Value	Description
$\mathscr{F}$	$\sim 10^5$	Cavity finesse
P	5 W	Laser power
λ	1064 nm	Laser wavelength
R_{beam}	1 cm	Gaussian width of the laser beam
T	200 K	Cavity temperature
L_z	$L_0 \leq 6.7$ mm	EO material thickness
$L_{x,y}$	5 cm	EO material lateral dimensions
σ	0.25	Poisson ratio*
Y_0	170 GPa	Young's modulus*
φ	10^{-6}	Loss angle*
ρ	$4.64\,\text{g/cm}^3$	Density*
κ	$4.6\,\text{W/(m}\cdot\text{K)}$	Thermal conductivity*
C	$628\,\text{J/(kg}\cdot\text{K)}$	Heat capacity*
α	$14.8 \times 10^{-6}/\text{K}$	Thermal expansion*
β	$\sim 5 \times 10^{-4}/\text{K}$	Thermo-refractive coefficient*

*The material properties are reported for $LiNbO_3$.

Table 3.1: GALILEO benchmark experimental parameters.

Table 3.1 provides benchmark experimental parameters. Note that we choose the hierarchy $L_z < R_{\text{beam}} \ll L_{x,y}$, which is analogous to the geometry of LIGO mirror coatings; the calculations that follow will also be analogous.

We will compare different thermal noise contributions with quantum (photon shot) noise, assuming lithium niobate ($LiNbO_3$) as the electro-optic (EO) material, with the amplitude spectral density (ASD) of the quantum noise (see the main text for details):

$$\mathrm{ASD}_{\mathrm{s.n.}} = \sqrt{\hbar\omega_{\mathrm{laser}}P_{\mathrm{in}}} = 9.7\times10^{-10}\,\frac{\mathrm{W}}{\sqrt{\mathrm{Hz}}}\,. \tag{3.12}$$

Using the transfer function $\delta P_{\mathrm{out}}/\delta L = (2\pi/\lambda)P_{\mathrm{in}}N\mathscr{F} \sim 2\times10^{13}\,\mathrm{W/m}$ we can translate this ASD to an effective displacement ASD:

$$\mathrm{ASD}_{\mathrm{s.n.}} = \sqrt{\mathscr{S}_{\delta z}} \sim 4\times10^{-23}\,\frac{\mathrm{m}}{\sqrt{\mathrm{Hz}}} \tag{3.13}$$

According to the following computations of the thermal noise sources for an operational instrument temperature $< 200\,\mathrm{K}$, we conclude that in the DM mass range of interest:

$$\mathrm{ASD}_{\mathrm{thermal}} < \mathrm{ASD}_{\mathrm{s.n.}} \tag{3.14}$$

3.5.1 Brownian noise

Homogeneous mechanical damping inside a material is typically characterized by an imaginary contribution to the Young's modulus:

$$Y = Y_0[1 + i\varphi(\omega)] \tag{3.15}$$

where φ is the so-called loss angle, which is given by the quality factor of the material's internal mechanical modes as $\varphi = 1/Q_{\mathrm{int}}$. The dissipated power due to φ can be written as $\langle W_{\mathrm{diss|mechanical}}\rangle = \omega\varphi(\omega)U_{\mathrm{def}}$, where U_{def} is the maximum elastic deformation energy of the material under an oscillatory drive at frequency ω. Assuming that $L_{x,y} \gg R_{\mathrm{beam}}$ and that

the mechanical resonance frequencies are far away from ω, one recovers the well-known result for the Brownian noise PSD as studied in the context of interferometric gravitational wave detectors [281]:

$$S_{\delta z|\text{Brownian}} \simeq 1.87 \times \frac{8k_BT}{\omega} \frac{1-\sigma^2}{\pi^2 Y_0 R_{\text{beam}}} \varphi \tag{3.16}$$

where the numerical factor 1.87 applies to a Gaussian optical beam. Therefore, for $LiNbO_3$ EO material in the GALILEO detector we have:

$$\text{ASD}_{\text{Brownian}} = \sqrt{\text{S}_{\text{ffiz}|\text{Brownian}}} \simeq 6.1 \times 10^{-24} \left(\frac{2ß \times 10\,\text{GHz}}{!} \right)^{1/2} \frac{\text{m}}{\sqrt{\text{Hz}}} \tag{3.17}$$

for the choice of parameters in Table 3.1.

3.5.2 Inhomogeneous thermal noise

Whenever there is space-dependent temperature variations $\delta T(\mathbf{r})$, there will be entropy redistribution, and therefore dissipation, due to heat flow. The rate of change of entropy density s in terms of heat flow per unit area $\mathbf{j}$ is given by $\dot{s} = -(\nabla \cdot \mathbf{j})/T$, which implies:

$$W_{\text{diss}} = -T \int \mathrm{d}^3\mathbf{r} \frac{\nabla \cdot \mathbf{j}}{T} = \underbrace{-T \int \mathrm{d}^2\vec{A} \cdot \frac{\mathbf{j}}{T}}_{\text{surface}} \underbrace{-T \int \mathrm{d}^3\mathbf{r}\, \mathbf{j} \cdot \nabla(\frac{1}{T})}_{\text{bulk}} \tag{3.18}$$

where we used $W_{\text{diss}} = T\dot{S}$. Using κ as the thermal conductivity in the bulk, i.e., $\mathbf{j} = -\kappa \nabla T$, the second term can be written as:

$$W_{\text{diss}|\text{bulk}} = \frac{\kappa}{T} \int \mathrm{d}^3\mathbf{r}\, (\nabla \delta T)^2 \tag{3.19}$$

To proceed with the surface term, we assume radiative thermal equilibrium with the surrounding environment, which implies a vanishing net radiative heat flow. However, at first order we have $\mathbf{j} = 4\varepsilon_{\text{emm}}\sigma_{\text{SB}}T^3\delta T$ (linearized Stefan-Boltzmann law), where ε_{emm} and σ_{SB} are the EO material's emissivity and Stefan-Boltzmann constant, respectively. As a result, the radiative surface dissipation is:

$$W_{\text{diss|surface}} = \frac{1}{T}\int \mathrm{d}^2\vec{A}\cdot\mathbf{j}\delta T = 4\varepsilon_{\text{emm}}\sigma_{\text{SB}}T^2\int \mathrm{d}x\mathrm{d}y\ \delta T^2 \tag{3.20}$$

Next, we employ the process of entropy injection according to Eq. (3.10), so that we can use the FDT to compute the noise PSD. We solve the diffusion equation with this source:

$$\rho C\dot{\delta T} - \kappa\nabla^2\delta T = \partial_t\left(\frac{\partial Q_{\text{inj}}}{\partial V}\right) \tag{3.21}$$

which can be greatly simplified considering the hierarchy of length scales involved in the problem. We notice that the sharpest spatial heat injection gradient in the system is given by the laser beam radius. For the benchmark parameters given in Table 3.1, we can thus neglect the second term in the diffusion equation. As a result,

$$\delta T = \frac{1}{\rho C}TF_0\cos(\omega t)q(\mathbf{r}) \tag{3.22}$$

with $q(\mathbf{r}) = (1/L_z)I(x,y)$. The bulk and surface dissipated power, following the above integrals, are [159]:

$$\left\langle W_{\text{diss|bulk}}\right\rangle = \frac{\kappa T F_0^2}{2\rho^2C^2}\frac{1}{L_z}\frac{1}{\pi R_{\text{beam}}^4} \tag{3.23}$$

$$\left\langle W_{\text{diss|surface}}\right\rangle = \frac{2\varepsilon_{\text{emm}}\sigma_{\text{SB}}T^4F_0^2}{\rho^2C^2}\frac{1}{L_z^2}\frac{1}{\pi R_{\text{beam}}^2} \tag{3.24}$$

Thermo-elastic effect. Temperature fluctuations can couple to the interferometer phase noise through thermal expansion [91]. For a non-zero thermal expansion coefficient $\alpha \neq 0$,

$$\delta z \equiv \delta L_z = \alpha(1+\sigma) L_z \delta T \tag{3.25}$$

where, σ is the Poisson ratio. Therefore, the $\mathscr{A}$ coefficient in the FDT for thermo-elastic noise source is:

$$\mathscr{A}_{\mathrm{TE}} = \alpha(1+\sigma) L_z \tag{3.26}$$

Thermo-refractive effect. Temperature fluctuations can also couple to the interferometer phase noise through the temperature dependence of the refractive index [92]. In other words, if $\beta = \mathrm{d}n/\mathrm{d}T \neq 0$,

$$\delta z \equiv \delta L_z = -\beta \lambda \, \delta T \tag{3.27}$$

In this case, the corresponding $\mathscr{A}$ coefficient is:

$$\mathscr{A}_{\mathrm{TR}} = -\beta \lambda \tag{3.28}$$

As pointed out in [173], we should consider thermo-elastic and thermo-refractive effects coherently. We thus define a total coefficient:

$$\mathscr{A} = \mathscr{A}_{TE} + \mathscr{A}_{TR} = \alpha(1+\sigma) L_z - \beta \lambda \tag{3.29}$$

Finally, we are ready to combine all results into the FDT, and compute the bulk and surface

contributions to the interferometer noise:

$$S_{\text{ffiz|bulk}} = \mathscr{A}^2 \frac{4k_B\kappa}{\omega^2} \frac{T^2}{\rho^2 C^2} \frac{1}{L_z} \frac{1}{\pi R_{\text{beam}}^4} \tag{3.30}$$

$$S_{\text{ffiz|surface}} = \mathscr{A}^2 \frac{16k_B\varepsilon_{\text{emm}}\sigma_{\text{SB}}}{\omega^2} \frac{T^5}{\rho^2 C^2} \frac{1}{L_z^2} \frac{1}{\pi R_{\text{beam}}^2} \tag{3.31}$$

which implies,

$$\text{ASD}_{\text{bulk}} = \sqrt{\text{S}_{\text{ffiz|bulk}}} = 5.6 \times 10^{-29} \left(\frac{2\pi \times 10\,\text{GHz}}{\omega} \right) \frac{\text{m}}{\sqrt{\text{Hz}}} \tag{3.32}$$

$$\text{ASD}_{\text{surface}} = \sqrt{\text{S}_{\text{ffiz|surface}}} = 1.1 \times 10^{-29} \left(\frac{2\pi \times 10\,\text{GHz}}{\omega} \right) \frac{\text{m}}{\sqrt{\text{Hz}}} \tag{3.33}$$

for the choice of parameters given in Table 3.1 and $\varepsilon_{\text{emm}} = 1$.

3.5.3 Photo-thermal noise

Another source of temperature fluctuation inside the EO material is photon absorption. Optical photons absorbed in the material can generate a collection of phonons that thermalize quickly and lead to local temperature increase [91]. The noise PSD due to such a process in a thin material is calculated by Braginsky et al.:

$$S_{\text{ffiz|photo-thermal}} = \alpha^2 (1+\sigma)^2 \frac{\hbar \omega_{\text{laser}} W_{\text{abs}}}{(\rho C \pi R_{\text{beam}}^2)^2} \frac{1}{\omega^2} \tag{3.34}$$

where ω_{laser} and W_{abs} are the carrier frequency and average absorbed power. We assume that 10% of the total power gets absorbed in the medium. In this case, we have:

$$\text{ASD}_{\text{photo-thermal}} = \sqrt{\text{S}_{\text{ffiz|photo-thermal}}} \simeq 1.3 \times 10^{-28} \left(\frac{2ß \times 10\,\text{GHz}}{!} \right) \frac{\text{m}}{\sqrt{\text{Hz}}} \tag{3.35}$$

for the choice of parameters given in Table 3.1.

3.6 Projected sensitivities

In order to project the sensitivity of the GALILEO experiment in the light-DM parameter space, we calculate the shot noise-limited and time-averaged SNR. The DM coherence time τ_c plays an important role here. As long as the integration time $t < \tau_c$, the total number of interferometer signal photons scales linearly with t, the shot noise scales as $\sqrt{t}$, and hence the measurement SNR $\propto \sqrt{t}$. The SNR degrades for $t > \tau_c$ as the phase of the light-DM background field varies during the measurement. However, the overall measurement sensitivity to the presence of a non-zero average light-DM background field can still be improved with repeated independent measurements, each lasting for time τ_c, with the resulting SNR scaling as $\sqrt{T/\tau_c}$, where T is the total overall time of the repeated measurements. In this repeated measurement regime, the effective noise power spectral density scales as $(T/\tau_c)^{-1/2}$. The SNR scaling behavior in the two regimes can be combined as [99]:

$$\mathrm{SNR} = \frac{\delta P_{\mathrm{out}}}{\mathrm{ASD}_{\mathrm{s.n.}}} (\tau_c T)^{1/4} \tag{3.36}$$

Using Eqs. (3.1), (3.6), and (3.7), we thus estimate GALILEO SNR values for axion and dark photon DM as follows [3]:

$$\begin{aligned}\mathrm{SNR} \simeq & \left(\frac{L_0 N \mathscr{F}}{6.7\,\mathrm{mm} \times 1.5 \times 10^5}\right)\left(\frac{\lambda}{1064\,\mathrm{nm}}\right)^{-1/2}\left(\frac{P_{\mathrm{in}}}{5\,\mathrm{W}}\right)^{1/2}\left(\frac{T}{\mathrm{s}}\right)^{1/4} \\ & \times \begin{cases} 20\left(\dfrac{g_{a\gamma\gamma}}{10^{-10}\,\mathrm{GeV}^{-1}}\right)\left(\dfrac{B}{10\,\mathrm{T}}\right)\left(\dfrac{m_{\mathrm{DM}}}{100\,\mu\mathrm{eV}}\right)^{-5/4} \\ 120\left(\dfrac{\kappa}{10^{-11}}\right)\left(\dfrac{m_{\mathrm{DM}}}{100\,\mu\mathrm{eV}}\right)^{-1/4} \end{cases}\end{aligned} \tag{3.37}$$

where we use $BaTiO_3$ as the EO material. We set projections in the axion and dark photon DM parameter space using the criterion SNR ~ 1, as shown in Fig. 3.2.

[3] We use (3.3) and (3.5) as estimates for the DM-induced electric field, neglecting the spatial profile of electric field inside the EO material.

To achieve maximum sensitivity in the higher-mass regime, we propose using multiple EO materials inside a FP cavity, each separated by $2\pi/m_{\rm DM}$. As discussed above, laser absorption in the EO material limits $L_{\rm eff} \leq 1\,{\rm km}$. This means that for $\mathscr{F} = 1.5 \times 10^5$ we have $L_0 N \lesssim 6.7\,{\rm mm}$. Therefore, for $m_{\rm DM} \lesssim 90\,\mu{\rm eV}$ (corresponding to $L_0 \gtrsim 6.7\,{\rm mm}$) we use a single EO material with a thickness of 6.7 mm; whereas for $m_{\rm DM} \gtrsim 90\,\mu{\rm eV}$ (corresponding to $L_0 = \pi/m_{\rm DM} < 6.7\,{\rm mm}$) we use multiple EO materials. Vertical gray dashed lines in Fig. 3.2 indicate the required number of EO materials for the higher-mass DM parameter space to achieve maximum sensitivity.

In the proposed detection scheme, the background DM-induced electric field oscillations manifest as an oscillatory signal at the interferometer output. It is therefore crucial to have a high photodetector bandwidth in order to resolve higher-mass DM-induced oscillations. While commercially available low-noise photodetectors have a bandwidth of up to 50 GHz (corresponding to $m_{\rm DM} \simeq 210\,\mu{\rm eV}$), there are currently demonstrations of detectors with bandwidths up to 500 GHz [283, 489]. The EO material's response time will also limit detection of DM masses higher than a few meV. We thus set a higher mass limit of about 2 meV in Fig. 3.2, corresponding to a photodetector bandwidth of about 500 GHz. In the low-mass axion regime the Fabry-Perot cavity length becomes a limiting factor, because at least one arm of the interferometer must be within the magnet producing the large bias magnetic field necessary for axion-induced signals. Therefore, we consider only axion masses greater than $0.4\,\mu{\rm eV}$ in the sensitivity estimations. This requirement is more relaxed for dark photon searches, where no background magnetic field is needed.

It is possible to reduce the observed noise below the nominal shot-noise limit through *squeezing*, where the electromagnetic vacuum noise in the measurement readout quadrature is reduced, with a corresponding increase of the noise in the other quadrature, consistent with the Heisenberg quantum limit. To date, laser interferometric gravitational wave detectors have successfully achieved 10 dB vacuum squeezing [445, 450, 493], which is equiva-

lent to improved sensitivity by a factor of about 3. As part of our sensitivity projections in Fig. 3.2, we also consider squeezing to further improve the detector reach.

3.7 Summary

We proposed a new approach to detect axion and dark photon dark matter (DM) over almost four decades in mass from about $0.1 - 10^3\,\mu$eV. We dub this experiment GALILEO, which is based on laser interferometry and uses electro-optical properties to detect DM-induced electric fields. The proposed experiment explores parameter spaces that are challenging to probe with resonant cavity haloscopes in the high mass and low mass regimes. Future technical improvements, such as the development of materials with enhanced electro-optical properties, may extend the reach of this approach to the QCD axion dark matter parameter space across a range of several orders of magnitude for the axion mass.

Chapter 4: Ultra-Heavy Dark Matter Search with Electron Microscopy of Geological Quartz

Note: This chapter draws on the work published in [161]. For a detailed discussion and complete technical content, refer to Appendix A, which includes the full text of the original article.

Despite extensive direct detection efforts, simple weakly interacting DM candidates have evade detection, prompting interest in more complex dark sectors. In particular, DM with strong self-interactions could lead to the formation of composite states–ultra-heavy dark matter (UHDM)–through dark-sector nucleosynthesis in the early universe. These massive composite objects, with masses far exceeding 10^{24} GeV, would interact more readily with standard model matter and produce rare but distinct signals, requiring alternative detection strategies that rely on large exposure rather than detector sensitivity.

One promising approach is to search for damage tracks left by UHDMs in ancient geological samples, which act as natural particle detectors with billion-year exposure times. We focus on geologically old quartz as a target material and propose a readout method based on scanning electron microscopy with cathodoluminescence (SEM-CL), offering high spatial resolution and no need for etching. This method improves on previous efforts with mica crystals, such as those by Price and Salamon [358], by allowing larger

sample areas and better background discrimination. In this work, we assess the feasibility and sensitivity of this approach and explore its capability to probe a class of composite UHDM models.

4.1 Detection feasibility and experimental protocol

Solid-state detectors have long been used to record particle tracks [182, 183, 212], including proposals to detect WIMPs via nanoscale damage in synthetic crystals [297, 367] or ancient rocks [63, 155, 168]. Building on this, we propose using ancient quartz to detect UHDM, which can deposit enough energy to locally melt the quartz along its path. These melted regions would re-solidify into amorphous silica—stable over geological times—and can be identified using SEM-CL [424]. While SEM-CL may also detect non-melting lattice distortions, we only focus on the more robust signature of UHDM-induced melting.

We illustrate the detection protocol in Figure 4.1. The proposed experimental protocol for detecting UHDM involves selecting ancient, low-impurity quartz samples that have remained unannealed for over a billion years and exhibit low CL background. Each selected sample, approximately 1 cm^3 in volume, is sectioned into $100\,\mu\text{m}$ slices, polished using standard petrographic techniques, and scanned on both faces using SEM-CL. The search focuses on identifying correlated damage features, indicative of a continuous track across multiple slices, rejecting false positives by non-detection of aligned damage spots over additional layers. SEM-CL is well suited for this purpose as it is a non-destructive method with sufficient spatial resolution.

We propose three stages of sample scanning, of increasing scale and sensitivity. The first phase, Quartz-1 m^2, involves scanning enough samples to reach a total exposure of 1 $\text{m}^2\cdot\text{Gyr}$ using four SEM-CL systems over two years, probing UHDM masses up to 10^{27} GeV. The second phase, Quartz-10 m^2, would use 20 SEM systems over four years

to reach 10^{28} GeV sensitivity. Finally, the Quartz-100 m^2 phase would involve 100 SEM systems over eight years, achieving exposures capable of probing UHDMs with masses up to 10^{29} GeV. While alternative imaging methods such as CT or confocal microscopy may offer 3D reconstruction capabilities, their slower scan rates and technical limitations make SEM-CL the most practical choice for this search, with other methods reserved for potential follow-up analysis of candidate tracks with higher resolution.

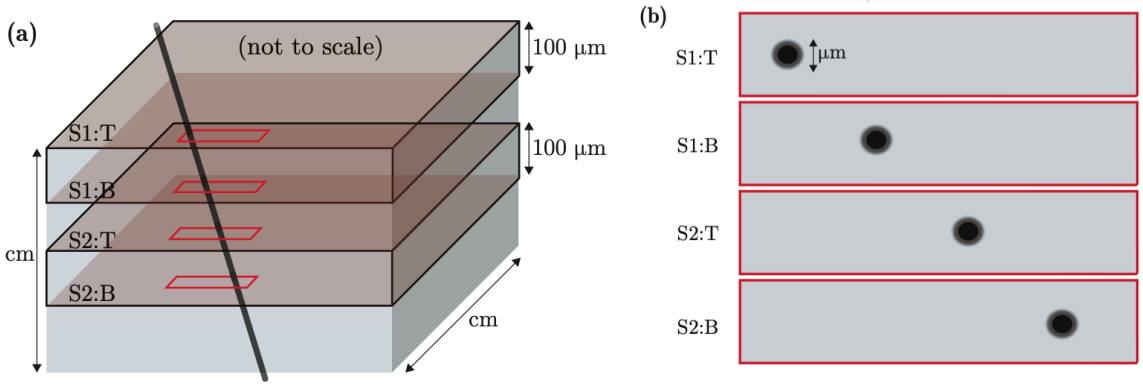

Figure 4.1: Schematic of the proposed readout method. **(a)** A quartz sample of size $\sim$ cm^3. The black straight line illustrates a damage track as a result of an ultra-heavy composite dark matter (UHDM) particle passing through the sample. The sample is sectioned into multiple sections of thickness $\sim$ 100 μm. We show several sections where the top and bottom surfaces are highlighted, which would be scanned using SEM-CL. **(b)** Correlated damage spots of micron-scale diameter over a macroscopic (mm-scale or longer) distance, between sections is the unique signature of the ultra-heavy DM particle interaction with quartz. Note that the probability of background features coincidently aligning reduces exponentially with the number of correlated layers. For a realistic feature density of $1000/cm^2$, simulations show that correlations of 4 layers efficiently rejects false positive signals.

4.1.1 Quartz samples and backgrounds

The UHDM signal (long, continuous, micron-scale in diameter damage tracks) is highly distinctive, as no known natural or cosmic ray-induced process produces such features. Localized defects from radioactive decay or crystal growth can be ruled out due to their limited spatial extent, while even weakly interacting particles like neutrinos fail to leave extended

tracks of sufficient energy density. Geological stress fractures may traverse the entire length of the crystals but differ in geometry and they lack the amorphous quartz signature indicative of UHDM-induced local melting. Thus, the extended structure of UHDM-induced damage tracks provides a powerful tools for background rejection.

To enhance this discrimination, the experimental design involves SEM-CL scans across serially sectioned quartz slabs to search for correlated damage spots spanning multiple layers. Backgrounds from radioactive isotopes, such as uranium-induced fission tracks, are detectable but typically form isolated halos rather than linear tracks. These features, while potentially mimicking UHDM signals in a single scan, are readily disqualified due to lack of multi-layer correlation. Interestingly, preserved fission tracks also serve as a useful indicator of the sample's thermal history, as their survival suggests absence of recent annealing, thereby supporting the stability of any older UHDM-induced features.

In our work, hydrothermal vein quartz (HVQ), particularly from the Jack Hills in Western Australia, is identified as an optimal target material due to its high purity, low impurity levels, and geologically stable history. HVQ from this region forms large, well-preserved veins with exceptionally low Ti and Al inclusion concentrations (which is critical for minimizing CL background) and has remained at relatively low temperatures (¡420°C) for over 1.7 billion years. These properties allow large-scale exposure with minimal background contamination and enable efficient use of the SEM-CL scanning protocol. Jack Hills HVQ thus offers a unique and ideal natural archive for conducting a high-sensitivity search for UHDM interactions over geological timescales. Figure 4.2 presents an initial SEM-CL scan of a HVQ sample from Jack Hills, illustrating several key proof-of-principle points discussed above.

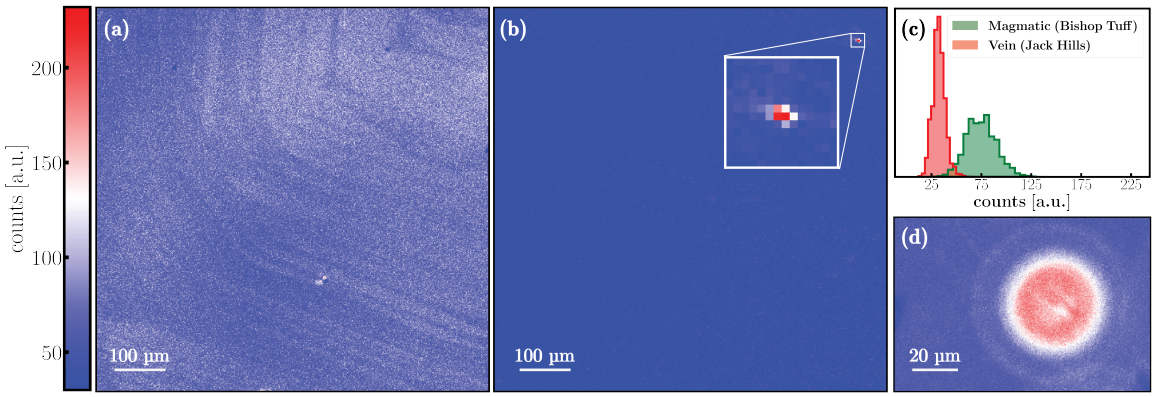

Figure 4.2: Example quartz sample characterization. SEM-CL images of two samples, **(a)** magmatic quartz from Bishop Tuff with Ti concentration 51 ± 6 ppm, and **(b)** vein quartz from Jack Hills with Ti concentration 5.2 ± 6.5 ppm, measured on a mass spectrometer. The scan rate is 20 s/mm^2 with 1.5 μm resolution for magmatic quartz and 5 s/mm^2 with 3 μm resolution for vein quartz (we forecast the full-scale UHDM experiment time and resources using these values). In (b) we identify a few high-count pixels in the vein quartz image, which demonstrates the possibility of high-resolution detection of concentrated CL emission. The inset shows a zoomed-in image of the region of interest with high-count pixels. These pixels could be a melting track intersection, which needs to be investigated by correlating multiple sections as described in the text. **(c)** Normalized histogram of the pixel counts in arbitrary units for each of the two sample SEM-CL images. Vein quartz shows a lower CL noise level as well as smaller variation, making it a suitable target for our detection proposal. **(d)** SEM-CL signal from a uranium halo (measured in a different quartz sample from those shown in (a) and (b)). Microscopic uranium inclusions have decayed over time; the fission products from these inclusions create crystal lattice damage, which emits cathodoluminescence (CL) upon excitation by the SEM. The CL signal from an ultra-heavy composite dark matter (UHDM) particle track would also result from crystal lattice defects at and around the track of melted quartz. Any such uranium halos in a UHDM search would be disqualified as potential damage tracks by lack of correlated damage in other slices of the sample.

4.1.2 Model-independent sensitivity

The proposed experiment is designed to detect UHDM candidates that (1) pass through quartz samples with high enough probability and (2) deposit sufficient, localized energy to melt a micron-scale region. The expected number of DM transits through a quartz sample of area $L \times L$ over a duration T is estimated as:

$$N \sim 1 \left(\frac{10^{29}\,\text{GeV}}{m_{\text{DM}}} \right) \left(\frac{L}{10\,\text{m}} \right)^2 \left(\frac{T}{10^9\,\text{yr}} \right), \tag{4.1}$$

assuming the local dark matter density $\rho_{\text{DM}} \approx 0.3\,\text{GeV}/\text{cm}^3$. Given quartz samples that are $\sim 10^9$ years old and areas up to 100 m^2 (in stage three of the experiment), this implies sensitivity to UHDM with mass $m_{\text{DM}} \lesssim 10^{29}$ GeV.

An UHDM particle traversing Earth deposits energy primarily through collisions with Standard Model nuclei. The energy per nucleus, E_1, can reach up to the kinematic limit of ~ 10 keV. For simplicity, we assume the UHDM traverses several kilometers into the Earth's surface without significant deceleration, maintaining its Milky Way virial velocity $v_{\text{DM}} \sim 10^{-3}c$. Under this assumption, the energy deposition rate is bounded from above by:

$$\frac{dE}{dx} \lesssim 10^{13} \frac{\text{MeV}}{\text{Å}} \left(\frac{m_{\text{DM}}}{10^{29}\,\text{GeV}} \right). \tag{4.2}$$

To produce a robustly detectable amorphous damage trail in quartz, the deposited energy per unit length must exceed the latent heat required to melt a micron-radius cylinder:

$$\frac{dE}{dx} \gtrsim \frac{\text{MeV}}{\text{Å}}. \tag{4.3}$$

Additionally, the energy transferred per collision must exceed the quartz melting temperature ($10^4\,\text{K} \sim 1$ eV) in order for the energy deposition to be sufficiently localized, but not

surpass the kinematic limit:

$$1\,\mathrm{eV} \lesssim E_1 \lesssim 10\,\mathrm{keV}. \tag{4.4}$$

Figure 4.3 illustrates the parameter space accessible to the quartz detector, showing that this technique probes a wide range of UHDM masses and energy deposition rates in a model-independent way. For a concrete model of UHDM and a discussion of the experimental reach of the proposed method within that model's parameter space, see Appendix A.

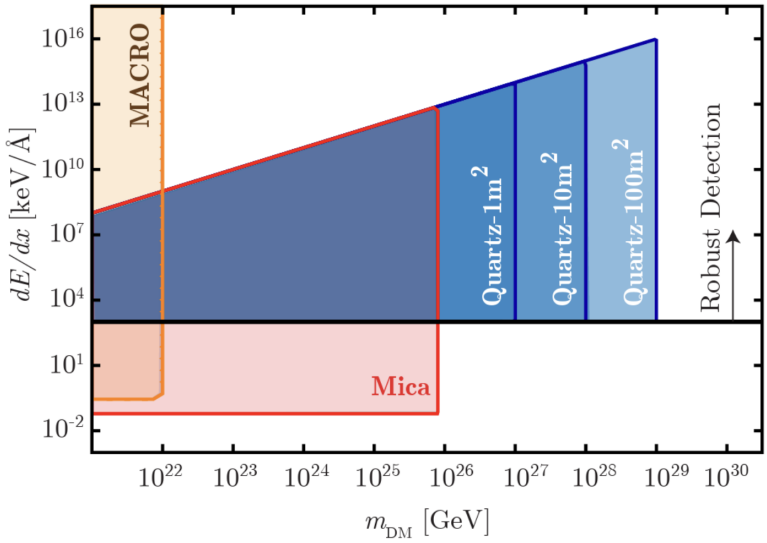

Figure 4.3: Sensitivity projections for the proposed ultra heavy dark matter (UHDM) search. Model-independent reach of the geological-quartz detector proposal expressed as stopping power dE/dx vs mass m_{DM} of a passing UHDM particle, together with the existing constraints from MACRO for energy deposition per nucleus $E_1 \sim 1$ eV [31, 393] as well as from damage track searches in ancient mica [358]. The vertical and slanted boundaries of the quartz-detectable parameter space (for different effective detector areas) stem from the requirements of an $O(1)$ probability of transit, Eq. (A.1), and a negligible slowing of the UHDM up to a 1 km depth, Eq. (A.2), respectively. The black horizontal line indicates the melting threshold for a micron-sized lateral region, Eq. (A.3), above which robust detection is possible.

4.2 Conclusion and outlook

We propose a novel method for detecting UHDM particles based on the identification of long, cylindrical damage tracks in ancient quartz using SEM-CL. This approach offers two major advantages: the natural billion-year exposure time of geological quartz enables sensitivity to DM masses as high as 10^{29} GeV, and the distinctive damage morphology allows robust discrimination from backgrounds. Focusing on tracks resulting from melting-induced amorphous silica, this work demonstrates that geological materials, in combination with modern imaging techniques, can be used as powerful detectors for probing previously inaccessible regions of DM parameter space.

Future work may aim to extend experimental sensitivity to lower energy depositions, potentially below the melting threshold. This includes signal calibration using laser-induced tracks and noise characterization across quartz samples with varied CL activator concentrations. While quartz is a prime candidate due to its availability and imaging compatibility, other minerals with similar properties may also be suitable, enabling complementary searches. We also analyzed a concrete UHDM model featuring composite bound states from a QCD-like dark sector coupled via a light mediator, identifying viable, detectable parameter space consistent with existing constraints (see Appendix A). Broadening the scope to other DM models capable of producing similar geological signatures remains an exciting direction for future explorations.

Chapter 5: LISA Double White Dwarf Binaries As Galactic Accelerometers

Note: This chapter draws on the work published in [164]. For a detailed discussion and complete technical content, refer to Appendix B, which includes the full text of the original article.

The Laser Interferometer Space Antenna (LISA) is a future space-based gravitational wave observatory that will detect gravitational waves in the millihertz regime. Among the most abundant sources expected in the LISA frequency band are Galactic double white dwarf (DWD) binaries–systems composed of two white dwarf stars in close orbits. These binaries produce continuous, nearly monochromatic gravitational waves over the typical LISA mission duration of several years.

In this chapter, we explore a novel use of LISA's observations of DWD binaries: using them as "Galactic accelerometers." The central idea, developed in [164], is that the frequency of gravitational waves from DWD systems can exhibit small but measurable shifts over time due not only to intrinsic binary evolution (like inspiral) but also due to the acceleration of the binary relative to the Solar System barycenter. This apparent frequency change encodes information about the gravitational potential of the Milky Way and thus provides a new way to map its mass distribution.

The dynamics of stars and compact binaries in the Milky Way are governed by the Galaxy's gravitational potential, which arises from the combination of its luminous components (bulge, disk) and dark matter halo. Traditionally, our knowledge of this potential has come from electromagnetic observations of stellar motions and gas kinematics. However, such methods are often limited by equilibrium assumptions and does not include dynamical information, i.e., acceleration of the Galactic sources.

LISA, through its precise measurement of DWD gravitational wave signals, offers an independent and complementary approach. By measuring how the observed frequency of a DWD's gravitational wave signal changes over time, it is in principle possible to infer the line-of-sight acceleration experienced by the system due to the Galaxy's gravitational field. Since this effect is cumulative and depends on the system's location in the Galaxy, a large ensemble of such measurements provides a new way to reconstruct the Galactic potential.

5.1 Galactic acceleration and synthetic population

To model the apparent acceleration of Galactic double white dwarf (DWD) binaries, we adopt a simplified, axisymmetric representation of the Milky Way's gravitational potential. The model consists of three components: a Miyamoto–Nagai stellar disk, a Hernquist bulge, and a Navarro–Frenk–White (NFW) dark matter halo. From this potential, the Galactocentric acceleration is computed as the negative gradient of the total potential.

In the observer frame (assumed to follow the Sun's motion), the apparent line-of-sight acceleration of a source has two main contributions: (i) the differential gravitational acceleration between the source and the observer projected along the line-of-sight, and (ii) a perspective (or Shklovskii) acceleration resulting from the proper motion of the source across the sky. The latter is estimated under the assumption that DWDs follow near-circular orbits in the Galactic disk and bulge.

Acceleration maps (see Figure 5.1) show that the gravitational component can be either positive or negative depending on the source location, while the perspective acceleration is always positive. The typical magnitude of the total apparent acceleration is on the order of $10^{-10}\,\mathrm{m/s^2}$, with the strongest contributions arising near the Galactic Center and the far side of the disk.

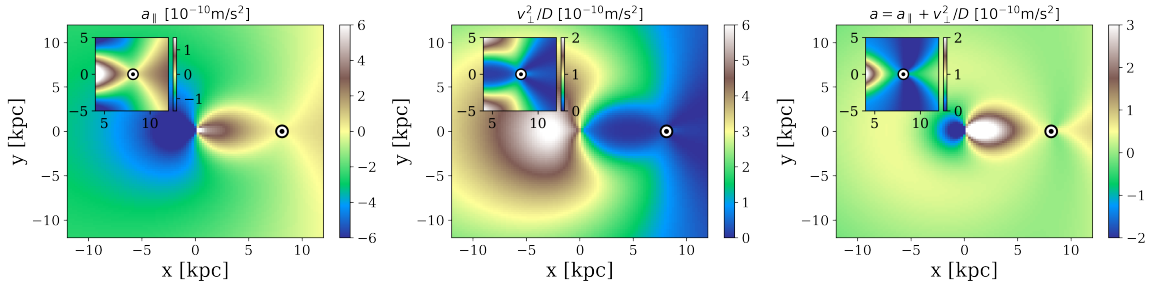

Figure 5.1: Model maps of Galactic acceleration. Left: Galactic line-of-sight acceleration contribution $\Delta a \cdot \hat{n}$. Center: Shklovskii (perspective) contribution using only $v_{\mathrm{circ.}}$. Right: Sum of the two contributions. The contours of these quantities are shown as functions of x and y, the Galactocentric coordinates on the Galactic plane, aligned such that the location of the Sun (labeled by $\odot$) is along the x axis. Insets in each panel show acceleration maps centered on the Sun, with enhanced contrast.

We use a synthetic population of Galactic DWD binaries using from a catalog developed by Thiele et al. [438], which combines simulations of Milky Way-like galaxies with stellar and binary evolution codes to generate the catalog. For a 10-year LISA mission, resolvable sources are selected by requiring a signal-to-noise ratio (SNR) greater than 7, averaged over position, orientation, and polarization angle. This yields a sample of approximately 16,000 resolvable DWD systems shown in Figure 5.2. A subset of these, known as verification binaries, are systems already identified through electromagnetic (EM) observations and are guaranteed to be detectable by LISA. Currently, this subset includes about 10 detached DWDs, which are also expected to exceed the detection threshold.

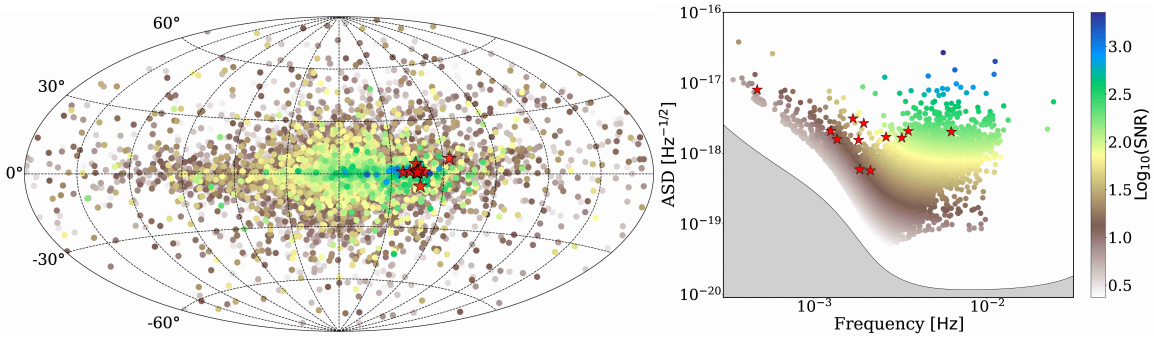

Figure 5.2: Synthetic population of Galactic DWDs observable in the 10 yr LISA mission. *Left:* Aitoff projection of the population in the Galactic longitude and latitude map. *Right:* The population shown in the amplitude spectral density (ASD) vs. frequency plane, together with the LISA noise curve (in gray), which includes the DWD confusion noise. DWD sources are simulated following Ref. [438] (the total number of sources is 16264); verification binaries (labeled with red stars) are from Ref. [268]. For both panels, DWD symbol color indicates LISA SNR for the associated GW.

5.2 Fisher analysis

The prospects of DWD binaries as Galactic accelerometers for mapping the Galactic gravitational potential is explored through a combination of analytical arguments and quantitative Fisher matrix analysis in our work.

An apparent acceleration a of a DWD system induces observable deviations in the GW frequency evolution $f(t)$, relative to the intrinsic chirp signal $f_s(\tau)$ expected in the source's rest frame. These effects are subtle due to the slow frequency evolution of DWDs over LISA's nominal 10-year observation period, as well as small Galactic accelerations.

We argue that distinguishing the effects of acceleration from intrinsic binary evolution requires measuring high-order derivatives of the GW frequency. The first frequency derivative $\dot{f}_0(\tau)$ is generally measurable for many DWDs, but is degenerate with acceleration and the intrinsic chirp. Breaking this degeneracy is possible through measuring the second derivative $\ddot{f}_0$, which is only feasible for a small subset of high-SNR, high-frequency DWDs. A dephasing criterion, defined by a significant shift in the GW phase due to higher-order frequency derivatives, indicates that only a small number of DWD systems will exhibit a

measurable second derivative $\ddot{f}_0$ over a 10-year observational baseline; see Figure 5.3.

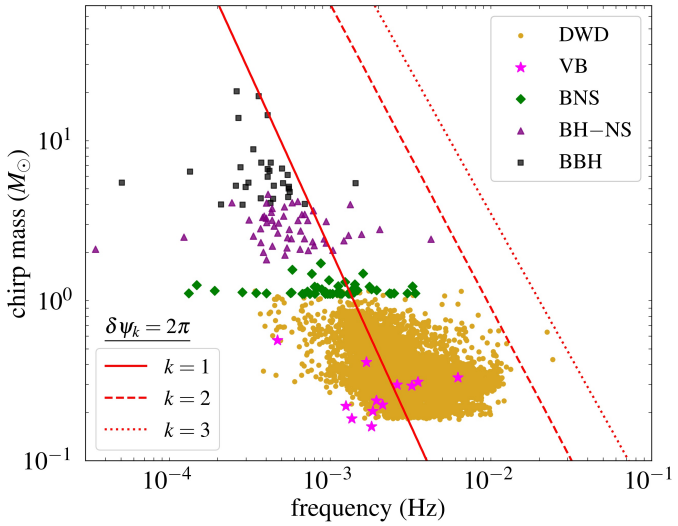

Figure 5.3: Yellow dots show the synthetic DWD binary population considered in this work in the frequency vs. chirp mass plane. Other types of compact binaries listed in the legend are verification binaries (VB), binary neutron stars (BNS), black hole–neutron star binaries (BH–NS), and binary black holes (BBH). The red lines are contours of constant dephasing $\delta\psi_k = 2\pi$. The plot suggests that there should be a sizeable portion of the DWD population with measurable $\dot{f}_0 \equiv f_0^{(k=1)}$ (i.e., to the right of the $k = 1$ line), while $\ddot{f}_0 \equiv f_0^{(k=2)}$ is only measurable for a few binaries (roughly, those to the right of the $k = 2$ line).

To quantify uncertainties, Fisher matrices were computed using both time-domain and frequency-domain GW signal models. A representative DWD system with $\mathscr{M} = 0.44 M_\odot$, and SNR = 1000 shows that $\dot{f}_0$ can be determined to within $\sim 1\%$. However, $\ddot{f}_0$ remains poorly constrained, resulting in large uncertainty in the inferred acceleration, even for high-SNR sources. This confirms that, using GW data alone, the degeneracy between $\dot{f}_{s0}$ and a cannot be lifted in practice. The situation improves significantly when EM data is available. If the chirp mass $\mathscr{M}$ or the distance D to the source is independently known (e.g., from spectroscopy or Gaia parallax), the degeneracy between $\dot{f}_s$ and a is broken, allowing precise estimation of the acceleration. Thus, combining LISA data with EM measurements enables DWDs to serve as effective accelerometers for probing the Galactic potential.

5.3 Galactic accelerometry

We quantify the uncertainties in measuring DWD accelerations and assess the prospects for constraining the Galactic mass distribution. In particular, we use a mdel with a single free parameter: the normalization parameter $\mathscr{N}$ that linearly scales the fiducial Galactic gravitational potential $\Phi = \mathscr{N}\Phi_{\rm model}$.

Using Fisher matrix analysis, the uncertainties in GW-derived parameters for the synthetic DWD population are computed under various assumptions. Including higher-order GW frequency derivatives, such as $\ddot{f}_0$, does not significantly improve constraints on key parameters due to their poor measurability. The observed frequency derivative $\dot{f}_0$ can be measured to within 10% for many sources, but remains degenerate with intrinsic binary evolution and apparent acceleration. After transforming to physical parameters—source-frame frequency $f_{\rm s0}$, intrinsic chirp rate $\dot{f}_{\rm s0}$, and normalized acceleration $\mathscr{N}$—the degeneracy becomes explicit, rendering both $\dot{f}_{\rm s0}$ and $\mathscr{N}$ essentially unmeasurable; see Figure 5.4. This implies that, from GW data alone, the Galactic acceleration cannot be measured, even when aggregating across the full LISA-observable DWD population.

The inclusion of EM data significantly improves parameter inference. When the chirp mass $\mathscr{M}$ is known (e.g., from spectroscopy), degeneracies between $\mathscr{M}$, D, and $\dot{f}_{\rm s0}$ are broken, allowing more accurate estimation of $\mathscr{N}$. Comparative Fisher matrix calculations demonstrate that fixing $\mathscr{M}$ externally reduces uncertainties in all other parameters; see Figure 5.5.

We forecast the improvement in the relative error of the Galactic potential normalization, $\varepsilon_{\mathscr{N}} = \sigma_{\mathscr{N}}/\mathscr{N}$, as EM surveys of LISA DWD counterparts become more complete. Using the synthetic DWD population, we model EM survey completeness as a spherical volume around the Sun within which *all* LISA sources have identified EM counterparts.

Figure 5.6 illustrates how $\varepsilon_{\mathscr{N}}$ decreases with increasing survey coverage distance, com-

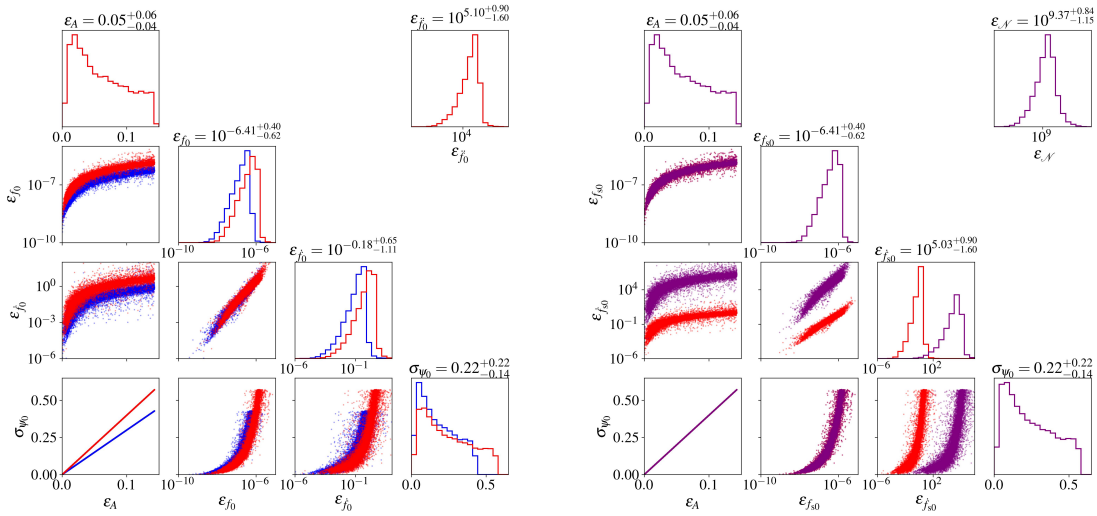

Figure 5.4: Measurement uncertainties for a synthetic population of Galactic DWDs (model FZ from Ref. [438]) using GWs alone. *Left*: The second time derivative of the GW frequency $\ddot{f}_0$ is either included (red) or excluded (blue) from the set of parameters in the Fisher matrix calculation. Here, numbers quoted at the top of plots refer to the "red" case. *Right*: The parameters include either the observed first and second time derivatives of the GW frequency (red, same points as in the left panel), or the source GW frequency $\dot{f}_{s0}$ and the global parameter $\mathscr{N}$ (purple), which is related to the Galactic gravitational potential as in Eq. (B.39). Here, numbers quoted at the top of the plots refer to the "purple" case.

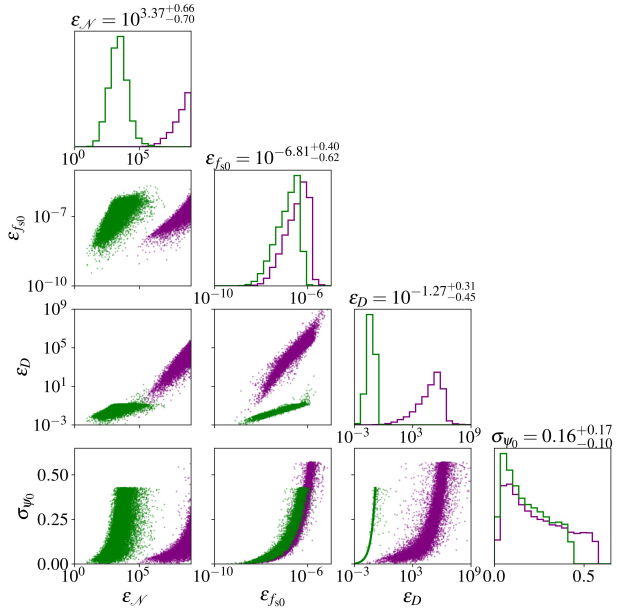

Figure 5.5: Comparison of the measurement uncertainties on the parameters $(\mathscr{N}, \mathscr{M}, D, f_{s0}, \psi_0)$ when the chirp mass $\mathscr{M}$ is included (purple) or excluded (green) from the parameter set. The numbers quoted at the top of the plots refer to the "green" case. Uncertainties on $\mathscr{M}$ are not shown even when this parameter is included, because in general it cannot be determined. The synthetic population of DWDs is the same as in Figure 5.4 above (i.e., model FZ from Ref. [438]).

paring two cases: (1) EM measurements determine only the chirp mass $\mathscr{M}$, and (2) EM data provide full characterization except for $\mathscr{N}$, i.e., $\{\mathscr{M}, D, f_{s0}, \psi_0\}$. In both cases, larger coverage increases the number of EM counterparts, reducing $\varepsilon_{\mathscr{N}}$. Sharp improvements correspond to inclusion of high-SNR sources. In case (1), $\varepsilon_{\mathscr{N}}$ asymptotes to ~ 2 beyond $\sim 10\,\mathrm{kpc}$, indicating limited measurability. In case (2), uncertainties are an order of magnitude smaller, and $\mathscr{N}$ becomes measurable with $\sim 10^3$ counterparts within a few kpc, consistent with extrapolations from current verification binary catalogs [269]. This analysis suggests the feasibility of Galactic accelerometry with LISA as part of a multimessenger approach.

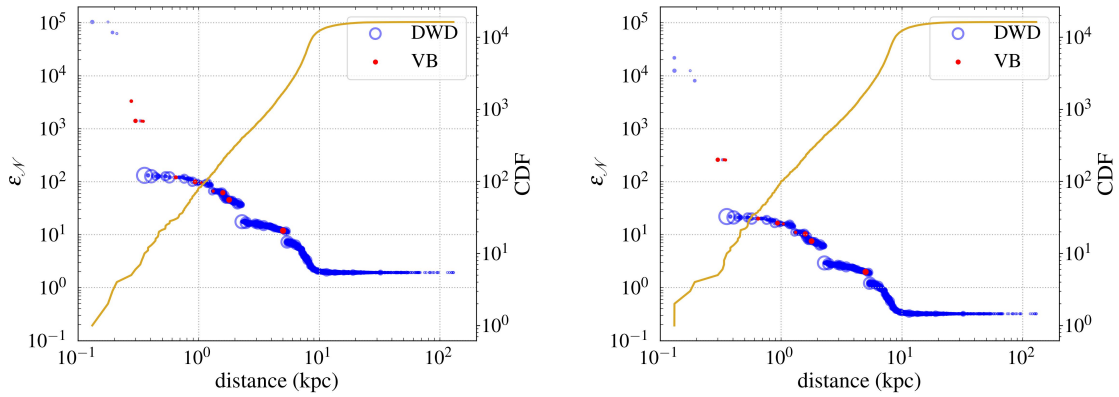

Figure 5.6: *Left panel:* only the chirp mass $\mathscr{M}$ is determined through EM observations. *Right panel:* all parameters (other than normalized acceleration $\mathscr{N}$) are determined through EM observations: i.e., $\{\mathscr{M}, D, f_{s0}, \psi_0\}$. In each plot, the vertical position of a given circle or dot (as measured by the left vertical axis) indicates the relative measurement uncertainty on $\mathscr{N}$, $\varepsilon_{\mathscr{N}} \equiv \sigma_{\mathscr{N}}/\mathscr{N}$, assuming that all DWDs within a certain distance from the Sun (as given by the position of the circle or dot on the horizontal axis) were used to infer the acceleration; the orange line and the right axis show the cumulative distribution function (CDF) of the DWDs within that distance. Recall that $\mathscr{N} = a/a_0$, where a_0 is the acceleration in the fiducial model of the Milky Way: see also Eq. (B.39). Individual sources are marked in blue (for all sources in the catalog, i.e., those detectable by LISA) or red (for verification binaries). The sizes of the circles or dots are proportional to the source SNR. Although the distance is not the only factor determining the GW SNR of a source, we observe a general trend of SNR falling with distance.

5.4 Conclusion

We have shown that LISA's resolved double white dwarf binaries can serve as accelerometers to probe the Milky Way gravitational potential. While gravitational wave data alone suffers from strong parameter degeneracies limiting the measurement of apparent accelerations, combining these observations with electromagnetic measurements of binary parameters significantly improves constraints. In particular, identifying and characterizing about 10^3 electromagnetic counterparts enables determination of the Galactic potential normalization parameter. This multimessenger approach complements existing dynamical tracers from electromagnetic observations, offering a promising new avenue to map the Galactic gravitational potential with LISA.

Chapter 6: Final Remarks

This thesis has explored innovative precision measurement approaches to advance the search for dark matter across a broad spectrum of candidate masses and interaction regimes, demonstrating the promise of combining quantum sensing, materials science, and astrophysical techniques.

In **Chapter 2**, in the quest for directional detection of WIMPs, we developed and analyzed a solid-state detector concept based on quantum defects in diamond. This approach leverages the exceptional spatial resolution and strain sensitivity of nitrogen-vacancy centers to identify and reconstruct nanoscale damage tracks induced by nuclear recoils. The detector concept offers a viable pathway to overcome the neutrino floor by enabling directional discrimination of particle signals from neutrino backgrounds–a critical milestone for future direct detection experiments. Our analysis highlights both the near-term experimental challenges and the medium-term roadmap toward prototyping a functional detector, emphasizing the interdisciplinary synergy required to realize these capabilities.

Beyond WIMPs, in **Chapter 3**, we proposed the GALILEO experiment, a novel method leveraging electro-optical material and optical interferometry approach to search for ultralight bosonic dark matter candidates such as axions and dark photons over a wide mass range. GALILEO's innovative design addresses key sensitivity gaps in existing haloscope experiments and provides complementary benchmarks that motivate its experimental implementation for broader coverage of the dark matter parameter space. This approach could significantly broaden the accessible parameter space and paves the way for future technical

improvements to probe the QCD axion regime as well as dark matter models.

In **Chapter 4**, we proposed a novel method to search for ultra-heavy composite dark matter (UHDM) by analyzing damage tracks in ancient quartz samples using scanning electron microscopy cathodoluminescence (SEM-CL). The exceptional billion-year exposure time of these geological samples offers a unique window to detect extremely massive dark matter candidates, far beyond the reach of current direct-detection experiments. Our approach is largely model-independent regarding dark sector microphysics, relying primarily on the distinctive long damage trails UHDMs would leave in quartz. Future efforts will focus on refining experimental sensitivity and extending this method to other mineral targets, as well as broadening the class of dark matter models that can be tested.

Chapter 5 investigated the use of gravitational wave observations from LISA-resolved double white dwarf binaries as accelerometers to probe the Milky Way's gravitational potential. By modeling the Galactic potential and using a simulated population of detectable binaries, we assessed LISA's sensitivity to apparent line-of-sight accelerations encoded in Doppler modulations of gravitational wave signals. Our results emphasize the necessity of combining gravitational wave data with electromagnetic observations of binary parameters to break degeneracies and achieve precise measurements of the Galactic potential normalization. This multi-messenger approach, alongside refined modeling and accounting for systematic uncertainties, holds promise to improve our understanding of the Milky Way's mass distribution. Collectively, this technique complements existing electromagnetic dynamic tracers such as stellar accelerations and pulsar timing, enriching the landscape of Galactic gravitational studies.

Taken together, these complementary efforts illustrate the power of precision measurement techniques in probing fundamental physics beyond current limits. The interdisciplinary advances presented here contribute critical tools and concepts toward the overarching goal of identifying the elusive nature of dark matter, motivating continued experimental

and theoretical developments in the years to come.

Appendix A: Published Article: Ultra-Heavy Dark Matter Search with Electron Microscopy of Geological Quartz

Note: We reproduce ref. [161] in this appendix. Content of this appendix also appears in the PhD thesis at Johns Hopkins University of one of the co-authors, Erwin Tanin, titled 'Beyond the Standard Model Explorations'.

A.1 Introduction

A major outstanding puzzle in modern physics is the nature of dark matter (DM) [434]. Despite the ever-improving sensitivities of direct detection experiments, the simplest DM candidates have not been observed, motivating searches for a wider range of possible dark sectors. Moreover, challenges that simple cold DM candidates face on sub-galactic scales [100, 267] might be relieved with more complex dark sectors. For instance, self-interacting DM has been investigated to address small-scale challenges such as the core-cusp problem [289, 422].

Nearly all current DM detection strategies, ranging from direct-detection efforts in the laboratory to indirect signals from DM annihilation (or decay), are based on the assumption that the DM is distributed around the universe as a gas of free particles with a large number density. This picture naturally emerges if self-interactions within the dark sector are weak, but is not strictly prescribed by existing observational constraints. The most stringent limits arise from observations of the Bullet Cluster, which restrict the self-interaction cross

section per unit mass to be $\sigma_{\chi\chi}/m_{\rm DM} \lesssim 1\ {\rm cm}^2/{\rm g}$ [422]. It is apparent that the limit on $\sigma_{\chi\chi}$ itself is significantly weakened if DM is clustered into composite states with large masses $m_{\rm DM}$.

If the dark sector has strong self-interactions, it would undergo a nucleosynthesis process in the early universe much like the nuclei of the standard model (SM), whereby individual particles coalesce to form large composite states [217, 477]. SM nucleosynthesis suffers from a number of theoretical accidents (such as the deuterium bottleneck) that render certain light elements unstable and thereby inhibit the production pathway of ultra-heavy elements. Still, the SM manages to produce large composite systems [195]. It is thus not surprising that a completely unconstrained dark sector could also produce large composite objects. We will refer to these composite states, which can easily be much heavier than 10^{24} GeV, as ultra-heavy dark matter [203, 208].

Direct searches for canonical DM in the form of a gas of small particles leverage the large influx of these particles in a detector to compensate for their small cross section with SM particles. For example, about 10^{16} weakly interacting massive particles (WIMPs) of mass 100 GeV would pass through a $\rm m^3$ detector in a year, allowing for the direct detection of WIMP-nucleon scattering cross sections as low as $10^{-45}\ {\rm cm}^2$ [381]. UHDMs, on the other hand, would arrive with significantly lower flux and require a different detection strategy. Thus, an experimental strategy for UHDM detection should leverage generic signatures of large composite objects instead of focusing on the specifics of any one composite DM model, as the rich dynamics of an interacting dark sector can produce a plethora of models. Accordingly, we focus here on the fact that the many constituent particles of a UHDM will enhance its cross section with SM matter such that each rare UHDM incidence could result in a spectacular (and possibly lethal [414]) event with a distinct signature imitated by no SM effect. The detector sensitivity is therefore less important in such scenarios and can be traded for greater exposure that maximizes the probability of a rare UHDM

transit. In this paper, our primary focus is to establish the detectability of such a signal. While we provide an example of a DM model that yields such a signal, it is straightforward to construct other examples of ultra-heavy particles that can cause similar damage (e.g., Q-balls [271], charged primordial black hole relics [278]).

Damage tracks left by particles passing through the Earth over geological times could be recorded by ancient rock samples buried underground. For this reason, such geological samples have been proposed and used as "natural particle detectors" in the past, including for magnetic monopoles [165, 179, 180, 184, 241, 263, 357, 358], macroscopically large DM [411], WIMPs [63, 134, 155, 168, 171, 415, 416], and neutrinos [64, 244]. The geological exposure times of ancient rock detectors range from the present back to the time they were last heated naturally to the point of annealing, which can be up to $\sim 10^9$ years and is thus much longer than typical DM direct detection laboratory experiments (by factors of up to 10^9). This advantage makes geological DM detectors ideal probes of sparser, higher-mass composite DM. As we discuss in Sec. A.2, searches with 10 m^2 of billion-year old rock would probe DM masses up to $m_{\rm DM} \sim 10^{28}$ GeV. A major challenge for such a detection strategy is the ability to efficiently identify DM signatures in a large volume of rock and distinguish them from geological, radioactive, and cosmic ray backgrounds. Such discrimination is significantly simpler in searches for UHDMs, since the extremely long and continuous cylindrical damage patterns they generically leave are qualitatively different from the sporadic defects due to expected backgrounds.

Here, we assess the use of geologically old quartz samples as solid-state particle detectors to search for damage tracks left by UHDMs. Quartz, a crystalline polymorph of silica SiO_2, is one of the most abundant and well-studied minerals in the lithosphere [202]. Defects and damage tracks can be resolved down to the micron scale with SEM-CL: a scanning electron microscope (SEM) combined with a cathodoluminescence (CL) detector. Imaging provided by the SEM is supplemented with spectral information from CL,

which reveals the nature of trace elements and point defects in the quartz [423]. This modality has already proved successful at providing answers to key geological questions [10, 11, 214, 277, 292, 419, 455]. The technical advantages of SEM-CL mapping, as well as the considerable literature on its application in quartz, make it an appropriate choice for our readout method.

Note that a similar search for long damage tracks was performed by Price and Salamon [358] in ancient mica crystals with null results. While they used this result to constrain the abundance of magnetic monopoles, the experiment is also sensitive to UHDMs with masses $m_{\mathrm{DM}} \lesssim 10^{26}\,\mathrm{GeV}$ [74, 237]. Mica is a crystalline mineral with almost perfect basal cleavage, offering efficient sample preparation. However, the readout method used in their experiment requires acid etching prior to microscopy in order to enlarge damage tracks and render them visible in an optical microscope. Such an etching process also enlarges background signals in the form of naturally-occurring lattice defects. Hence, the success of the experiment hinges on the low level of background in the samples and its scalability is limited by the availability of sufficiently pristine mica crystals. By contrast, the lack of etching in our proposed SEM-CL readout and the more readily available quartz mineral that meets our requirements allow us to scan over larger sample areas and extend the search pioneered by Price and Salamon to higher DM masses.

The rest of the discussion is organized as follows. In Sec. A.2 we present an experimental realization of the UHDM detection method sketched above, identify optimal samples, and assess its model-independent sensitivity. We then demonstrate its ability to probe a simple composite UHDM model, taking into account various existing constraints, in Sec. A.3. Finally, we conclude in Sec. B.6.

A.2 Detection Feasibility

In this section, we investigate experimental issues for UHDM detection with quartz. Based on the considerations below, we establish the criteria for UHDM signatures to be robustly detectable with microscopy of about μm-resolution. We discuss the discovery reach of this approach in Sec. A.2.4 (see equations (A.2)-(A.4)).

A.2.1 Damage Tracks

Solid-state systems [182, 183, 212] have been used as particle track detectors with applications ranging from nuclear science to geophysics, as such tracks yield information about the history of the sample and properties of the impinging particles [181]. For example, DM detection using crystal damage tracks has been proposed as a directional signal in semiconductors such as diamond, where a WIMP scattering event would give rise to damage tracks of $\sim\ 30-100$ nm in length; the directional information in these tracks could enable such a detector to probe below the "neutrino floor" [297, 367]. Paleodetection, which looks for damage tracks of a similar size in ancient rock samples, has also been investigated for WIMP detection [63, 155, 168].

We propose using ancient quartz as a detector for ultra-heavy composite dark matter (UHDMs). As we discuss in Sec. A.2.4, each UHDM could deposit enough energy to locally melt nearby quartz along its trajectory. Since quartz nucleation under ambient conditions is a very slow process [98], the melted region would solidify into amorphous silica without recrystallizing. Detecting such amorphous micro-regions within quartz samples is feasible with SEM-CL, where defects in the tetrahedrally coordinated SiO_2 microstructure contribute to CL emission [424]. Even in the absence of melting, the same SEM-CL method would in principle be sensitive to linear tracks of lattice distortions left by UHDMs. However, quantitatively characterizing the sensitivity of this method to such tracks requires

further study of the backgrounds in natural quartz, which we leave for future work. Thus, in what follows we focus on detecting UHDMs that can cause melting.

A.2.2 Quartz Samples and Backgrounds

The signature of the proposed UHDM detection method is a long damage track, of micron-scale cross section, extending through the entire length of the quartz sample (see Figure 4.1a). This signature has the distinct advantage that no known mechanism produces such a track, allowing for strong geometric rejection of background signals. A variety of effects may induce localized disruption of the crystal lattice on the micron scale, such as extended growth defects or radioactive decays, but these localized features cannot pass through the entire macroscopic crystal. And although particles with low interaction probability (e.g., neutrinos or relativistic cosmic rays) can pass through an entire sample, their low nuclear cross sections yield dispersed individual damage events rather than a continuous, micron-scale-diameter track. The density of atmospheric neutrino-induced damage tracks falls off exponentially with the track length, with essentially zero density of tracks longer than a few mm [244]. Note that the imparted energy per unit length along such tracks is much lower than the robust detection threshold; however, if detected, they can be rejected as a UHDM signal due to the lack of correlation throughout the full $\sim$ cm extent of the sample.

Fractures induced by historical geological stresses could similarly pass continuously through an entire sample, but would in general be two- or three- rather than one-dimensional, and would not leave behind amorphous quartz within the damage track. Geologically-induced single line defects might also be present in quartz samples, however, at smaller scales, only observable by transmission electron microscopy (TEM) [280] or atomic force microscopy (AFM). So these features are not relevant backgrounds for the proposed read-

out.

To take advantage of the distinctive extended geometry of a UHDM signal, we propose a multi-phase scanning readout, where we search for correlated feature positions at multiple depths in the sample (see Figure 4.1). This allows us to reject backgrounds, which have an exponentially suppressed likelihood of lying along a single line (as shown by simulations discussed in Figure 4.1). An expected background signal, given the imaging resolution of our method, is from the presence of radioactive isotopes such as uranium, which lead to fission tracks and alpha recoil damage within the crystal lattice. These processes leave behind halos of size $\sim$ 10 μm [89], which are readily detectable using our proposed SEM-CL protocol (see Figure 4.2d). In a single two-dimensional SEM-CL scan, these could mimic a UHDM damage track, but would be disqualified as UHDM signals by lack of correlated damage in subsequent slices. The presence of some radioactivity-induced features is potentially beneficial to our analysis, as their preservation would indicate that recent annealing events would not have removed older, UHDM-induced features. As such, if the fission track age can be determined from the host quartz, the absence of UHDM-induced features implies the lack of UHDM interaction events since the time of occurrence of the fission track.

Quartz samples with low impurity levels are essential for reducing background levels. High-resolution cathodoluminescence (CL) studies reveal both the microstructure of the samples and trace element inclusions. Titanium (Ti) and aluminum (Al) are the two of the most abundant impurities in quartz. Ti is the dominant CL activator while Al is not generally considered an activator [277, 429]. Trace element studies show that quartz samples of different geological origins have a wide range of Ti and Al concentrations. Low-temperature hydrothermal vein quartz (HVQ) has the lowest trace element concentrations: quartz typically has a Ti concentration of a few 100 ppm; but this number could be as low as 6 ppm for an HVQ sample, which simultaneously has a low Al concentration [11, 385].

Here, we characterize preliminary measurements to demonstrate that low-Ti vein quartz samples are a suitable choice for our proposed experiment (see Figure 4.2).

We note that any mineral deposits with comparable geological history and suitability for low-background CL scanning could in theory serve as a target in a UHDM search. However, HVQ is well suited for a high sensitivity search: it is available in large quantities with high purity and crystal homogeneity from deposits with well characterized geological history. Hydrothermal fluid flow is commonly localized along fracture systems, fault systems, and shear zones that can produce vast arrays of quartz veins. When a fracture or fault remains open and under hydrothermal pressure for a sufficient period of time, hydrothermal vein quartz grows as large, euhedral, and high-purity crystals. These properties will enable us to analyze a large net exposure with the proposed protocol, using serial sectioning and SEM-CL scanning of large samples, with background rejection via correlation of damage spots across layers (see Figure 4.1b).

HVQ from the Jack Hills of Western Australia is an ideal source of quartz for the DM search. The siliciclastic units at Jack Hills contain numerous, large quartz veins that appear as prominent surface features (i.e., clusters of milky white outcrops that can form very localized topographic highs) observed throughout the range. The veins are generally either undeformed or very weakly deformed, and often show an abundance of high-purity, gem-quality quartz crystals. These HVQ systems can reach impressive sizes at several locations within the Jack Hills from cm-scale to 50 meters wide [418]. Several of the vein systems can be followed for several kilometers and appear to be associated with major episodes of brittle faulting. The combined work of Rasmussen et al. [370] and Spaggiari [417] provide strong evidence that units (including the hydrothermal quartz veins) at Jack Hills, particularly in the vicinity of the ”classic” W74 location, have likely remained at temperature conditions less than 330-420 °C for $\sim$ 1.7 Gyr. The fact that the tectonic environment can be evaluated in detail [65, 118, 417, 443] (including thermometry and age

dating) and consistently demonstrates equilibria at such low temperature (i.e., at or below greenschist facies), is to the best of our knowledge unique to Jack Hills, making it an ideal source of HVQ for our proposed measurements.

A.2.3 Experimental Protocol

The proposed experimental protocol is as follows:

1. Identify quartz samples that are (i) old, having last annealed no less than 1 Gyr ago; and (ii) clean, with low CL noise level and less than a few thousand micron-scale resolved CL features per cm^2.

2. Prepare about 10^4 samples of size $\sim cm^3$ that satisfy the above conditions and prepare each of the samples into sections of thickness $\sim 100\ \mu m$ (see Figure 4.1a). Polish the top and bottom surfaces of each section, then scan them with SEM-CL.

3. Search for correlated damage spots, across the first few sections, that are aligned, section-to-section, along a straight line (see Figure 4.1b).

4. If such a damage track of interest is identified, perform a dedicated search in subsequent sections to reject false positives.

5. Repeat steps 3 and 4 for all the cm^3 samples.

To prepare HVQ samples for SEM-CL analysis we perform a standard petrographic polishing preparation. Conventional polishing, using successive SiC powders ranging from 240-1200 ANSI[1] grit sizes ($\sim$10 minutes per grit) are used to gradually reduce surface topography. SiC polishing is followed by a series of automated polishing stages on a MiniMet polishing/grinding unit, proceeding from 3 to 1 to 0.1 micron Al_2O_3 grits ($\sim$30-60 mins

[1] American National Standards Institute

per grit, with $\sim$1 minute of ultrasonic bathing between grits). As these polishing stages are generally done on automated or semi-automated systems, large volumes of material can be processed. The effects of polishing on the quartz surface is negligible for most aspects of a UHDM search; there may be some localized damage to the near surface environment, restricted to the first few nm [464], whereas SEM-CL typically probes about 1 μm.

Additionally, polishing and SEM scanning should not significantly heat the sample. Paleomagnetic studies on ancient rock samples show that the magnetization, which would change under heating by only a few tens of degrees, remains unchanged after polishing [468]. While SEM interrogation may induce some heating for macroscopic, microns-thick samples such as we propose here, such heating should be limited to $\sim 10^{\circ}$C [226, 462]– especially with appropriately chosen SEM beam parameters. SEM-CL can therefore be considered a non-destructive readout method.

Alternative methods –including high resolution computed tomography x-ray (CT) or superresolution optical microscopy– offer sufficiently high resolution to measure UHDM-induced damage tracks, as well as the prospect of three-dimensional imaging. However, these methods generally require much longer scan times than SEM-CL, as well as method-specific constraints such as sample size restrictions or synchrotron beam availability. If correlated damage spots in serially-sectioned quartz slabs are identified by the proposed SEM-CL readout, follow-up experiments on the same sample could be pursued (due to the non-destructive nature of the SEM technique); e.g., 3D imaging using techniques such as CT or laser scanning confocal microscopy at different wavelengths.

The scanning rate with SEM-CL depends on sample properties such as the concentration of CL activators. Given a typical data acquisition time of $\sim$ 100 min per cm^2 with μm resolution (for example see Figure 4.2), we plan the experiment in three stages:

- Quartz-1 m^2: About two years of experiment time with four SEM-CL apparatuses

will be required to scan samples with a total area of about 1 m^2. The total quartz exposure of $\sim 1\,m^2\,Gyr$ for such a search would probe UHDMs of mass $m_{DM} \lesssim 10^{27}$ GeV. This first stage search would probe a currently unconstrained mass range with a new technique; see Figure 4.3.

- Quartz-10 m^2: 20 SEM apparatuses running for about four years would provide a total quartz exposure to UHDMs of $\sim 10\,m^2\,Gyr$, yielding sensitivity $m_{DM} \lesssim 10^{28}$ GeV.

- Quartz-100 m^2: 100 SEM apparatuses running for about eight years would provide a total quartz exposure to UHDMs of $\sim 100\,m^2\,Gyr$, yielding sensitivity $m_{DM} \lesssim 10^{29}$ GeV.

A.2.4 Model-Independent Sensitivity

The proposed experiment would be sensitive to a wide range of ultra-heavy dark matter (UHDM) candidates, independent of the underlying dark sector microphysics, that (1) pass through the quartz sample with sufficiently high probability while (2) depositing enough energy in a sufficiently concentrated way to melt a micron-size lateral region.

Given a DM candidate of mass m_{DM}, we can estimate the expected number of DM transits in a sample of area $L \times L$ over a duration T to be

$$N \sim 1 \left(\frac{10^{29}\ \text{GeV}}{m_{DM}}\right) \left(\frac{L}{10\,\text{m}}\right)^2 \left(\frac{T}{10^9\ \text{year}}\right) \tag{A.1}$$

based on the local DM density, $\rho_{DM} \approx 0.3\,\text{GeV}/\text{cm}^3$. As described in the previous sections, the quartz samples under consideration are roughly $T \sim 10^9$ year old, and a 100 m^2 sample area can be scanned in stage three. The requirement that $N \gtrsim 1$ imposes an upper bound on the UHDM mass, $m_{DM} \lesssim 10^{29}$ GeV ~ 100 kg. The advantage afforded by the large exposure of such a long-lived sample is manifest.

An UHDM moving through the Earth will collide with and deposit energy to SM particles along its path. The energy E_1 imparted to each SM nucleus can go as high as the kinematical limit of 10 keV (corresponding to nuclei acquiring twice the velocity of the UHDM in a collision) depending on how elastic these collisions are, while the stopping power dE/dx depends on E_1 as well as the UHDM radius. For simplicity, we assume in our estimates that the UHDM travels at least a few kilometers deep into the Earth's surface while maintaining its Milky Way virial velocity of $v_{\rm DM} \sim 10^{-3}c$. This amounts to an upper bound on the energy deposition rate

$$\frac{dE}{dx} \lesssim 10^{13} \frac{\rm MeV}{\text{Å}} \left(\frac{m_{\rm DM}}{10^{29}\ \rm GeV} \right). \tag{A.2}$$

Most of the deposited energy will likely go to SM nuclei. Only a tiny portion will go directly to electrons, whose low mass limits their kinetic energy gain (for kinematics reasons) and whose coupling to DM is severely limited by astrophysical and cosmological constraints [207]. The nuclei and electrons will then thermalize, leading to a loosening of molecular bonds as the electrons acquire more energy, and eventually cause melting. Due to thermal diffusion, the melted region will enlarge and cool. What ultimately remains, in the case of quartz, is a long cylindrical trail of amorphous silica, precisely the kind of damage that is detectable with the method outlined above.

In order to leave a robustly detectable damage trail, the UHDM must deposit sufficient energy per unit length dE/dx exceeding the required latent heat to melt each unit-length segment of a micron-radius cylinder. This amounts to a dE/dx threshold for robust detection of

$$\frac{dE}{dx} \gtrsim \frac{\rm MeV}{\text{Å}}. \tag{A.3}$$

See Figure A.1a for model-independent sensitivity projections. Further, since quartz has a

melting point of 10^4 K $\sim$ 1 eV and energy tends to spread outward, the energy deposition must be sufficiently localized that the energy E_1 gained by each nucleus is greater than the melting temperature, i.e. it must lie in the range

$$1\,\mathrm{eV} \lesssim E_1 \lesssim 10\,\mathrm{keV} \tag{A.4}$$

where the upper bound is the kinematical limit for energy transfer per nucleus (with mass number $A \sim 10$).

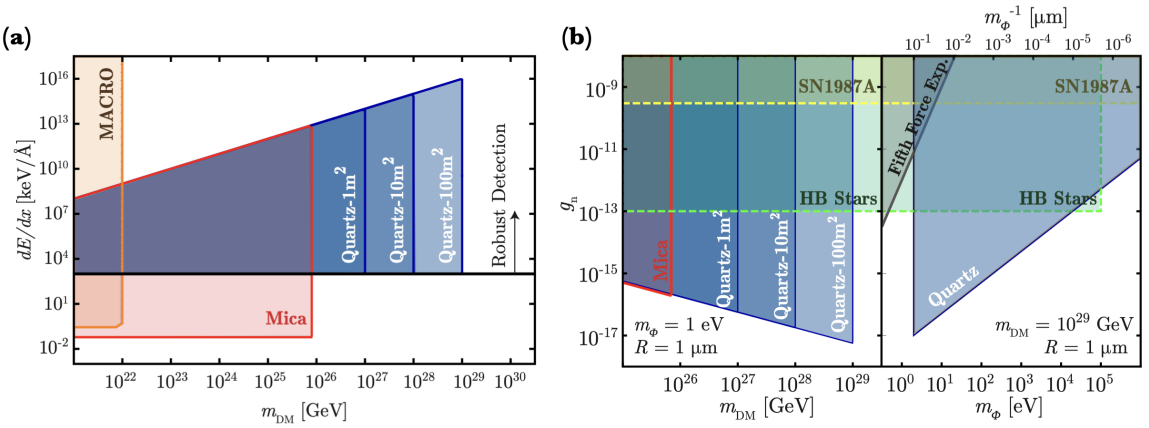

Figure A.1: Sensitivity projections for the proposed ultra heavy dark matter (UHDM) search. **(a)** Model-independent reach of the geological-quartz detector proposal expressed as stopping power dE/dx vs mass $m_{\rm DM}$ of a passing UHDM particle, together with the existing constraints from MACRO for energy deposition per nucleus $E_1 \sim 1$ eV [31, 393] as well as from damage track searches in ancient mica [358]. The vertical and slanted boundaries of the quartz-detectable parameter space (for different effective detector areas) stem from the requirements of an $O(1)$ probability of transit, Eq. (A.1), and a negligible slowing of the UHDM up to a 1 km depth, Eq. (A.2), respectively. The black horizontal line indicates the melting threshold for a micron-sized lateral region, Eq. (A.3), above which robust detection is possible. **(b)** Parameter space of the UHDM model considered in Sec. A.3. *Left:* reach on coupling $g_{\rm n}$ vs DM mass $m_{\rm DM}$. *Right:* reach on coupling $g_{\rm n}$ vs mediator mass m_ϕ. Also shown are existing constraints from ancient mica [358], fifth force experiments [207], and stellar cooling of SN1987A [207] and horizontal branch (HB) stars [207] (note that the stellar cooling bounds are model-dependent [148]). In these $g_{\rm n}$ plots, we set g_χ to its upper bound m_ϕ/Λ_χ from Eq. (A.14).

A.3 Example UHDM Model

In this section, we consider an example of a simple, ultra-heavy composite dark matter (UHDM) state [203] that can give rise to the desired damage tracks while being consistent with existing experimental and observational constraints. These composite objects consist of N_χ dark fermions χ whose mass, inverse size, and binding energy to form the UHDM are determined by a single scale Λ_χ. It follows that they have mass $m_{\rm DM} \sim N_\chi \Lambda_\chi$ and size $R \sim N_\chi^{1/3} \Lambda_\chi^{-1}$. We assume that the fermions χ interact with standard model nucleons $\psi_{\rm n}$ through a repulsive[2]. Yukawa interaction mediated by a scalar ϕ of mass m_ϕ:

$$-\mathscr{L} \supset \frac{1}{2} m_\phi^2 \phi^2 + g_{\rm n} \phi \bar{\psi}_{\rm n} \psi_{\rm n} - g_\chi \phi \bar{\chi} \chi \,. \tag{A.5}$$

We show that UHDMs with the following properties satisfy the robust detectability criteria detailed in Sec. A.2.4 without running afoul of any existing constraints:[3]

$$10^{26}\,{\rm GeV} \lesssim m_{\rm DM} \lesssim 10^{29}\,{\rm GeV} \tag{A.6}$$

$$10\ {\rm nm} \lesssim R \lesssim 1\ {\rm cm} \tag{A.7}$$

$$0.1\,{\rm eV} \lesssim m_\phi \lesssim {\rm MeV} \leftrightarrow\ 10^2\ {\rm fm} \lesssim m_\phi^{-1} \lesssim 1\,\mu{\rm m} \tag{A.8}$$

$$100\,{\rm keV} \lesssim \Lambda_\chi \lesssim 10\,{\rm GeV}\,. \tag{A.9}$$

This allows us to probe wide ranges of the couplings $g_{\rm n}$ and g_χ. Two slices of this parameter space are shown in Figure A.1b. Eq. (A.6) follows from Eq. (A.1) and ancient mica constraints; Eq. (A.7) follows from (A.3), (A.4), (A.13), and the quartz sample size of 1 cm;

[2] Attractive DM-nucleon interactions are just as compelling as the repulsive interaction considered here. We note that the attractive interactions might have more complicated dynamics as nuclei may get trapped and accumulate inside the UHDM. See e.g. [9]

[3] Due to various constraints, this parameter space has a complicated geometry. Here we simply identified the lower and upper limits for each parameter.

Eq. (A.8) follows from fifth force constraints and the requirement that the UHDM-nucleus interaction be treated classically; Eq. (A.9) follows from Eqs. (A.6) and (A.7).

A.3.1 Detectability with Quartz

The optimal UHDM detection signature is expected for mediators with a range m_ϕ^{-1} satisfying $\Lambda_\chi^{-1} \ll m_\phi^{-1} \lesssim \mu\text{m}$, since this is the intermediate regime where the UHDM-nucleon coupling is enhanced by the number of constituents χ of the UHDM within the range of the mediator $(m_\phi^{-1}/\Lambda_\chi^{-1})^3$ while simultaneously evading existing fifth force constraints. For simplicity of analysis we only consider part of the parameter space where $m_\phi^{-1} \ll R$. In doing so, we limit the UHDM's cross section to be at most geometrical.

An SM nucleus located inside the UHDM only sees the composite DM particle's constituents χ within the range of the mediator $m_\phi^{-1} \ll R$. Hence, to the SM nucleus each point in the bulk of the UHDM is just like any other, yielding a potential energy $V(r)$ as a function of the distance r from the center of the UHDM with the following profile:

$$V(r) = \begin{cases} +V_0, & r < R \\ 0, & r > R \end{cases} \tag{A.10}$$

where at the boundary $r \approx R$ the potential drops to zero exponentially over a length scale of order m_ϕ^{-1}, and

$$V_0 \sim \left(\frac{\Lambda_\chi}{m_\phi}\right)^3 \frac{g_\chi (10 g_\text{n})}{m_\phi^{-1}} \tag{A.11}$$

for SM nuclei with mass number $A \sim 10$. As a result, from the perspective of a nucleus the UHDM is just a constant potential hill moving at a velocity $v_\text{DM} \sim 10^{-3} c$.

Since the de Broglie wavelengths $(10\,\text{MeV})^{-1}$ of the SM nuclei are smaller than the

mediator ranges m_ϕ^{-1} of interest, we can treat the UHDM-nucleus interactions classically. When $V_0 \gtrsim 10\,\mathrm{keV}$, the potential V_0 prevents any nucleus from entering the UHDM. The UHDM-nucleus collisions are thus elastic, and the energy E_1 transferred to a nucleus saturates the kinematical limit $E_1 \sim 10\,\mathrm{keV}$. If $V_0 \lesssim 10\,\mathrm{keV}$, on the other hand, the nuclei can easily climb the potential hill, and the collisions between a nucleus and the UHDM's surface will be inelastic. When a nucleus encounters the surface of the UHDM, it receives a force $F \sim V_0/m_\phi^{-1}$ due to the gradient of the Yukawa potential. This force is exerted throughout the duration $\tau \sim m_\phi^{-1}/v_{\mathrm{DM}}$ of the collision, resulting in a nearly-instantaneous momentum kick $p_1 \sim F\tau$ which translates to the kinetic energy $E_1 \sim 10\,\mathrm{keV}\,(V_0/10\,\mathrm{keV})^2$ per nucleus. To sum up, the energy imparted to a nucleus after the passage of a UHDM is

$$E_1 \sim 10\,\mathrm{keV} \times \min\left[1, \left(\frac{V_0}{10\,\mathrm{keV}}\right)^2\right]. \tag{A.12}$$

Using a lattice spacing of about 5Å for quartz, the energy deposition rate then follows:

$$\frac{dE}{dx} \sim \frac{E_1}{5\text{Å}}\left(\frac{R}{5\text{Å}}\right)^2. \tag{A.13}$$

Having linked the model parameters with the quantities characterizing quartz damage tracks, the detectable parameter space can be evaluated based on the considerations in Sec. A.2.4 (see Figure A.1b).

A.3.2 Existing Constraints

A.3.2.1 The mediator

Past experiments and observations have placed limits on the coupling g_{n} of the mediator ϕ to standard model nucleons with varying severity for different masses m_ϕ of the mediator.

These include: collider constraints on the meson decay rate, laboratory *fifth-force* searches, and stellar cooling bounds from observations of the SN1987A event and horizontal branch (HB) stars. Note, however, that the stellar cooling bounds are model-dependent [148]. The following parameter space is thus ruled out [207]:

- Meson decay: $g_{\rm n} \gtrsim 10^{-6}$, $m_\phi \lesssim 100\,{\rm MeV}$.
- Fifth force: $g_{\rm n} \gtrsim 10^{-12}(m_\phi/{\rm eV})^3$, $m_\phi \lesssim 100\,{\rm eV}$.
- SN1987A: $3\times10^{-10} \lesssim g_{\rm n} \lesssim 3\times10^{-7}$, $m_\phi \lesssim 30\,{\rm MeV}$.
- HB stars: $g_{\rm n} \gtrsim 10^{-13}$, $m_\phi \lesssim 100\,{\rm keV}$.

Furthermore, the couplings of UHDM constituents χ to the mediator ϕ add extra self-interactions among χ that may destabilize the UHDM. In order for the UHDM to be stable the mediated self-interaction potential $g_\chi^2\Lambda_\chi^3 m_\phi^{-2}$ of a single χ must not exceed the binding energy Λ_χ. This puts an upper bound on the coupling g_χ of χ to the mediator ϕ:

$$g_\chi \lesssim \frac{m_\phi}{\Lambda_\chi}. \tag{A.14}$$

A.3.2.2 Direct detection

Of the currently and previously running direct-detection DM experiments, MACRO puts a strong constraint on our scenario due to its large volume. MACRO is a scintillator experiment with exposure of about 10^3 m$^2 \times 10$ years corresponding to $m_{\rm DM} \lesssim 10^{22}\,{\rm GeV}$ for 1 event over its decade-long lifespan. It is sensitive to energy depositions $\gtrsim 10\,{\rm MeV/cm}$ *to electrons* [31]. When a nucleus receives energy E_1 from interaction with a UHDM, only some fraction $Q(E_1)$, called the quenching factor, of that energy effectively goes to the electrons tied to the nucleus. It is this relatively small fraction of energy that is responsible for

the processes of scintillation and ionization that may occur subsequently. We can translate MACRO's $10\,\mathrm{MeV/cm}$ detection threshold to a sensitivity *to nuclear energy depositions* via effecting an increase by the quenching factor $Q(E_1)$ [393].

An even more stringent bound on our model arises from direct searches for long damage tracks in muscovite mica crystals [358]. The non-observation of tracks extending beyond naturally occurring defects and radioactivity damage was originally used to constrain the abundance of magnetic monopoles, but also limits the UHDM parameter space. This past mica search involved total sample area $\sim 1200\ \mathrm{cm}^2$ with sample ages $\simeq 5\times10^8\,\mathrm{yr}$, corresponding to a DM reach of $m_{\mathrm{DM}} \lesssim 10^{26}$ GeV. The energy deposition threshold for detection in this experiment via etching and optical microscopy was identified as $dE/dx \gtrsim 6\ \mathrm{GeV/cm}$.

A.3.2.3 Astrophysical and Cosmological limits

Indirect limits can also be placed on the couplings g_{n} and g_χ from the limits on DM-baryon and DM-DM cross sections. DM-baryon interactions in the early universe can affect baryon acoustic oscillations and is therefore constrained by CMB and LSS observations. This puts an upper bound on the DM-baryon momentum-transfer cross section that would be observed today: $\sigma_{\chi\mathrm{b}}/m_{\mathrm{DM}} \lesssim 10^{-3}\ \mathrm{cm}^2/\mathrm{g}$ [158]. Astronomical observations of the Bullet Cluster also place a limit on the DM-DM momentum-transfer cross section: $\sigma_{\chi\chi}/m_{\mathrm{DM}} \lesssim 1\ \mathrm{cm}^2/\mathrm{g}$ [422]. Since we are mainly interested in UHDMs with geometrical cross sections of order $\mu\mathrm{m}^2$ and masses up to $10^{29}\ \mathrm{GeV}(100\ \mathrm{kg})$, these astrophysical and cosmological observations only impose significant constraints on the low mass side of our parameter space. Moreover, these constraints are alleviated if UHDMs constitute less than 10% of the total DM mass, in which case the maximum detectable mass would also be lowered by an order of magnitude.

A.4 Conclusion and Outlook

Given the diverse range of theoretically well-motivated dark sectors, it is critical to perform searches with techniques that are sensitive to a broad class of dark-sector phenomena. In this paper, we propose a detection method for ultra-heavy composite dark matter particles (UHDMs). Our proposed experiment is based on mapping damage tracks in ancient quartz samples with SEM-CL scanning. This method has two significant advantages: (1) the billion-year exposure time of such samples enables us to probe DM candidates with masses as high as 10^{29} GeV(100 kg), surpassing the reach of existing direct-detection experiments, and (2) the distinctly-long cylindrical damage trails left by such UHDMs are easily distinguished from other features at the relevant scales.

In this work, we focus on detecting long tracks of amorphous silica in quartz samples expected from passing UHDMs that impart enough energy to cause melting. In future work, we will consider the feasibility of extending the experimental sensitivity to energy deposition rates below the melting threshold. For that purpose, we intend to carry out a number of studies including: (i) signal calibration by artificially creating damage tracks in synthetic quartz samples with a high-power pulsed laser of variable intensity and comparing it with the resulting CL signal levels; and (ii) noise calibration by preparing a set of quartz samples, natural and synthetic, with different concentrations of CL activators and analysing their CL emission rates. These studies will provide us a better understanding of the signal-to-noise ratio as seen in SEM-CL imaging, which will allow us to better estimate the detection threshold.

We focus here on quartz as a promising target mineral for UHDM detection because of the availability of abundant high-quality, old samples and the suitability of SEM-CL as a high-resolution, fast readout method. However, any mineral satisfying these two criteria is a potential target material; identifying such targets is valuable in verifying putative UHDM

signals in a complementary search, possessing different systematics.

Our proposed experiment is largely agnostic to the detailed microphysics of the dark sector, as long as it results in long damage tracks in geological quartz. To demonstrate the projected reach of the proposed approach, we considered a QCD-like dark sector that interacts with the standard model repulsively via a light mediator. The particle spectrum of this theory includes heavy bound states, composed of a large number of elementary dark fermions, which could create interesting targets for detection. We identified experimentally-detectable regions of the parameter space that satisfy various limits derived from phenomenological considerations as well as past observations. In future work, it would be interesting to delineate a broader range of DM models than can lead to similar damage patterns in ancient rock.

Appendix B: Published Article: LISA Double White Dwarf Binaries As Galactic Accelerometers

Note: We reproduce ref. [164] in this appendix. Content of this appendix also appears in the PhD thesis at Johns Hopkins University of one of the co-authors, Vladimir Strokov, titled 'Open Mic with LISA: Intermediate-Mass Black Holes and Double White Dwarfs'.

B.1 Introduction

The Laser Interferometer Space Antenna (LISA) [28, 30] is expected to detect the gravitational-wave (GW) signals of $\sim 10^4$ detached double white dwarfs (DWD) that reside primarily in the Milky Way galaxy [257, 259, 274] and its satellites [247, 255, 256, 373, 377]. Several tens of these DWDs have been identified through electromagnetic (EM) observations and are targets of particular significance for LISA, usually referred to as "verification binaries" [259, 268, 284].

One distinct advantage of GW observations is that they are unaffected by dust and stellar crowding, enabling probes of parts of the Galaxy that are challenging to access electromagnetically, such as those near or behind the Galactic Center [379, 389, 459, 481]. For this reason, several studies consider GWs from both the resolvable [194, 258] and unresolvable [67, 94] populations of DWDs as probes of Milky Way structures, complementary to EM observations. These studies propose using spectral and spatial features of the ensemble of Galactic GW signals from DWDs to infer the present *spatial* distributions of

Galactic DWDs, which are assumed to trace the underlying Milky Way structures (subject to inevitable biases from star formation rates, binary evolution, and observational selection). After the biases are modeled and removed, one can extract information about Milky Way structures, such as stellar mass, relative normalization, and morphology.

In addition to locating DWDs [430], GW measurements can also be used to determine the *relative motion* of resolved DWDs. While the motion of a DWD with constant velocity along the line of sight is completely degenerate with its intrinsic GW frequency, an *apparent acceleration* along the line of sight can lead to a time-dependent Doppler shift (i.e., a frequency "chirp") in the emitted GWs that is, at least in principle, detectable [81, 233, 307, 369, 376, 427, 433, 457, 481, 492]. We stress that, here and throughout the paper, what we refer to as the "apparent acceleration" along the line of sight $\hat{n}$ of a DWD at a distance D from the Sun is the sum of the its line-of-sight acceleration $a \cdot \hat{n}$ and the perspective acceleration $\mu^2 D$ due to its proper motion μ on the sky (also known as the "Shklovskii effect" [410]).

Provided that one can measure both the location and the apparent acceleration of a DWD, there is the tantalizing prospect of effectively using a population of DWDs as "test mass" accelerometers to probe Galactic structures. The motions of DWDs inferred from GW measurements encode different and, in principle, more direct information about the underlying Galactic gravitational potential compared to what can be inferred from their spatial distribution alone. There is, however, an important challenge to the practical application of this technique: GW phase changes due to the apparent acceleration of a DWD can be confused with its intrinsic frequency chirp due to GW emission. That said, additional information from EM observations of the same sources (before, during, and after GW measurements) may be used to break this degeneracy.

Motivated by the prospect of Galactic accelerometry via LISA measurements of GWs from DWDs–and by the anticipation of finding the EM counterparts to LISA sources–in

this paper we address the following questions:

(1) Under what circumstances, and to what degree, can we recover the apparent acceleration of individual DWDs from their gravitational waveforms, as observed by LISA?

(2) How well can we characterize large-scale Milky Way mass profiles (distributions) by including in the analysis the apparent acceleration of the large number of DWDs that LISA will resolve?

In the process, we also shed light on how the inclusion of apparent acceleration in the GW template affects the inferred DWD binary parameters.

The rest of the paper is organized as follows. In Sec. B.2 we provide a model map of the Galactic acceleration and describe the synthetic DWD population used for subsequent estimates. In Sec. B.3 we discuss the measurability of the center-of-mass acceleration of a DWD by carrying out a Fisher matrix analysis with GW observations alone. Then we consider the case in which some parameters of the source are assumed to be known from EM observations. In Sec. B.4 we consider the prospect of using LISA for detection of Galactic acceleration, and of leveraging the large number of observable DWDs to improve measurement uncertainties. In Sec. B.6 we present our conclusions. To improve readability, some technical material is relegated to the Appendices. In Appendix B.7 we briefly review the notion of perspective acceleration due to the proper motion of a source on the sky (the "Shklovskii effect"). In Appendix B.8 we perform a comparison of frequency domain (FD) and time domain (TD) results, showing that they are in good agreement.

Table B.1 provides a list of frequently used symbols used in this paper and of their definitions. In what follows we use geometrical units $G = c = 1$, where G is the gravitational constant and c is the speed of light.

Table B.1: List of frequently used symbols. Variations thereof and symbols used in passing are defined in the text.

Quantity	Symbol	Definition
Galactocentric radius	r	$\sqrt{x^2+y^2+z^2}$
Galactocentric radius projected onto the Galactic plane	R	$\sqrt{x^2+y^2}$
Source distance from Sun	D	
Galactic gravitational potential	Φ	
Galactic potential normalization	$\mathscr{N}$	$\Phi = \mathscr{N}\Phi_{\rm model}$
Line-of-sight unit vector	$\hat{n}$	
Total source velocity	v	
Source velocity in the sky plane	$v_\perp$	
Local acceleration	$a_\odot$	
Galactic line-of-sight acceleration	$a_\parallel$	$(-\nabla\Phi - a_\odot)\cdot\hat{n}$
Perspective acceleration	–	$v_\perp^2/D$
Apparent acceleration	a	$a_\parallel + v_\perp^2/D$
Observer frame time	t	
Source frame time	τ	
Coalescence time	$\tau_{\rm c}$	
Observer frequency	f	
Source frequency	$f_{\rm s}$	
GW phase	ψ	
Coalescence phase	$\psi_{\rm c}$	
DWD chirp mass	$\mathscr{M}$	
Time domain waveform	$h(t)$	
Frequency domain waveform	h_F	
Fourier frequency	F	
LISA observation time	$T_{\rm obs}$	
Error of θ_i in parameter inference	σ_{θ_i}	
Fractional error	ε_{θ_i}	$\sigma_{\theta_i}/\theta_i$

B.2 Galactic acceleration and the DWD population

In this section we present a simplified model of the Milky Way gravitational potential, from which we produce a model map of the Galactic acceleration contributing to the frequency chirp of GW sources. We also describe a synthetic population of Galactic DWDs that is used for Fisher calculations presented in subsequent sections.

B.2.1 Galactic acceleration

We assume a model for the coarse-grained gravitational potential of the Milky Way, $\Phi_{\rm model}$, which comprises a stellar disk, a bulge, and a dark matter (DM) halo:

$$\Phi_{\rm model} = \Phi_{\rm disk} + \Phi_{\rm bulge} + \Phi_{\rm DM}\,, \tag{B.1}$$

where the three components $\Phi_{\rm disk}$, $\Phi_{\rm bulge}$, and $\Phi_{\rm DM}$ are respectively modeled as a Miyamoto–Nagai stellar disk [311], a Hernquist sphere bulge [220], and a Navarro–Frenk–White DM halo [320]:

$$\Phi_{\rm disk} = -\frac{M_{\rm disk}}{\sqrt{r^2 + (c_1 + \sqrt{z^2 + c_2^2})^2}}\,, \tag{B.2a}$$

$$\Phi_{\rm bulge} = -\frac{M_{\rm bulge}}{r + c_3}\,, \tag{B.2b}$$

$$\Phi_{\rm DM} = -\frac{4\pi\rho_0 r_s^3}{r} \ln\left(1 + \frac{r}{r_s}\right)\,. \tag{B.2c}$$

Here (x, y, z) are the Galactocentric coordinates, and $r = \sqrt{x^2 + y^2 + z^2}$. The free parameters are assumed to be $M_{\rm disk} = 7 \times 10^{10} M_\odot$, $c_1 = 3\,{\rm kpc}$, $c_2 = 0.28\,{\rm kpc}$, $M_{\rm bulge} = 5 \times 10^9 M_\odot$, $c_3 = 0.6\,{\rm kpc}$, $\rho_0 = 9 \times 10^{-3}\, M_\odot\ {\rm pc}^{-3}$, and $r_s = 16\,{\rm kpc}$ [87, 88].

Given this model of the Milky Way gravitational potential, the Galactocentric acceler-

ation of a source is simply $-\nabla\Phi_{\rm model}$. In the observer frame, a time-dependent Doppler modulation of the GW phase results from the line-of-sight component of the *apparent* acceleration of the source. We assume for simplicity that the motion of the observer follows that of the Sun, with position, velocity, and acceleration relative to the Galactic center given by $R_\odot = 8.12\,{\rm kpc}\,\hat{x}$ [206], $v_\odot = 223\,{\rm km/s}\,\hat{y}$, and $a_\odot = \nabla\Phi|_{R_\odot} = -1.9\times10^{-10}\,{\rm m/s^2}\,\hat{x}$, respectively. (Small corrections to account for the motion of LISA relative to the Sun can be made in future work.) Here we assume that the Sun follows a circular orbit, with velocity given by the Galactic rotation curve:

$$v^2 = v_{\rm circ}^2 = R\frac{\partial\Phi}{\partial R}\,, \tag{B.3}$$

with $R = \sqrt{x^2+y^2}$ being the Galactocentric radius projected onto the Galactic plane.

The apparent acceleration of a Galactic source has two contributions: the line-of-sight projection of the Galactic acceleration w.r.t. the observer, $(-\nabla\Phi_{\rm model} - a_\odot)\cdot\hat{n} \equiv (\dot{v}-\dot{v}_\odot)\cdot\hat{n}$, and the perspective acceleration $a_{\rm Sh} = \mu^2 D$ due to the source's proper motion $\mu = v_\perp/D$ on the sky (otherwise known as the Shklovskii effect [410]); here, $\hat{n}$ is the unit vector along the line-of-sight, D is the distance to the source, and $v_\perp$ is the component of the source's velocity w.r.t. to the observer perpendicular to $\hat{n}$. In order to estimate $v_\perp$, and thus the contribution of the perspective acceleration, we distribute DWDs in the stellar disk and bulge following Refs. [257, 259]; and assume that the DWDs follow near-circular orbits in accordance with Eq. (B.3). Hence, the apparent acceleration reads

$$a = (-\nabla\Phi_{\rm model} - a_\odot)\cdot\hat{n} + \frac{v_\perp^2}{D}\,, \tag{B.4}$$

where $v_\perp$ is the component of $v_{\rm circ} - v_\odot$ perpendicular to $\hat{n}$, and the vector $v_{\rm circ}$ is tangential to the orbit of the source.

Figure 5.1 shows maps of the line-of-sight acceleration $a_{\parallel} = (-\nabla\Phi_{\rm model} - a_{\odot}) \cdot \hat{n}$, perspective acceleration $v_{\perp}^2/D$, and their sum a (the apparent acceleration) following from the model of the Milky Way potential given by Eqs. (B.1) and (B.2). The $x \leftrightarrow -x$ asymmetry of the maps is due to the off-center position of the Solar System, where the observer (e.g., LISA) resides. The line-of-sight acceleration is negative on the far side of the Galactic center ($x < 0$) and can be either positive or negative on the observer's side ($x > 0$). The magnitude of the acceleration generally grows towards the Galactic Center and decreases near the Sun. The perspective acceleration is always positive: it is strongest near the Galactic Center on the far side, where the y-component of the circular velocity is opposite to that of the Sun; and weakest in the Sun's vicinity, where the relative velocity with respect to the Sun almost vanishes. Depending on location, the two contributions to the total acceleration may amplify or cancel each other. Most importantly, the typical apparent acceleration is of the order of $\sim 10^{-10}$ m/s^2.

In general, stellar populations also undergo random peculiar motions v_p relative to the local $v_{\rm circ}$, with the typical components of v_p given by their respective velocity dispersions. For instance, the Sun has an oblique peculiar velocity of magnitude $v_p = 10.5 \pm 1.5$ km/s relative to the circular rotation velocity at the Sun $v_{{\rm circ},\odot} = 238 \pm 15$ km/s (the local standard of rest) [78]. Stars in the disk are subject to a multitude of scattering mechanisms that increase their velocity dispersions over time [35], and consequently the random stellar motions of the current stellar populations depend strongly on their age, metallicity, and locations of the population in question [408]. Among the assortment of stars, the kinematics of white dwarfs is relatively less understood, since their characteristically strong surface gravity and pressure lead to line broadening that makes the extraction of their radial velocities challenging [364]. The reported values of the RMS sum of the velocity dispersions in different directions of both isolated white dwarfs and DWDs in the disk typically do not exceed 60 km/s [34, 196, 364, 465], which amounts to $\lesssim 5\%$ corrections to the perspec-

tive acceleration when added in quadrature to the ~ 250 km/s circular rotation velocity at $R \gtrsim 5$ kpc [78]. Since the peculiar motion of DWDs appears to have little effect on their perspective accelerations, we neglect it in our analysis. The peculiar motion of stars may also slightly modify the mean azimuthal velocity of the population at a given location – an effect known as asymmetric drift [78], which we also neglect.

Also, while we adopt a simplified equilibrium and axisymmetric Galactic model in our analysis, it is known that the Milky Way exhibits non-equilibrium and non-axisymmetric properties, such as stellar streams, and bar and spiral structures of the stellar disk [77]. For example, in the N-body model GALAKOS of a Milky Way-like galaxy [154], the contribution of a bar and spiral arms to the number density is at most comparable with the axisymmetric part (see Figure 6 of Ref.[472]), and therefore it does not affect the order of magnitude obtained assuming axial symmetry. Once the main effect is detected (i.e., acceleration contribution to the frequency chirp of DWD GW signals), these details can be taken into account in future work through more realistic models of the Milky Way.

B.2.2 Synthetic DWD population

Simulations of the Galactic binary population in the LISA band have improved in recent years [259, 275, 324, 438, 458, 490]. These simulations typically predict $\mathcal{O}(10^4)$ resolvable DWDs, making them the most abundant LISA sources. Additionally, dozens of black hole and neutron star binary systems are expected to be detected by LISA [458]. In this work we consider a synthetic population of DWD GW sources following Thiele *et al.* [438], where the authors use simulations of Milky Way-like galaxies and stellar evolution codes to generate a present-day Galactic binary population. We adopt their model FZ [438], which relies on a metallicity-dependent initial binary fraction, as suggested by electromagnetic observations in the solar neighborhood. Due to tidal effects and mass transfer at play in

the progenitor binaries, all DWDs in the population are circular. This gives a typical GW emission timescale of $\gtrsim 10^4$ yr.

Figure 5.2 illustrates the characteristics of the synthetic DWD population. We choose the resolvable sources for a 10 yr LISA mission by requiring a position-, orientation- and polarization-angle averaged SNR > 7, which results in about $16,000$ resolvable sources. The subset of the DWD population usually referred to as "verification binaries" consists of sources known from prior EM observations, and guaranteed to generate detectable GW signals in LISA. The current collection of verification binaries includes ~ 10 detached double white dwarfs [178, 268, 269] expected to have SNR > 7, and marked by red stars in Figure 5.2.

B.3 Fisher analysis

The ubiquity of DWDs suggest they are well suited to serving as Galactic accelerometers, enabling mapping of the Galactic gravitational potential. However, as we first motivate with a "back-of-the-envelope" argument (Section B.3.1), it is challenging to determine the center-of-mass acceleration of a DWD via GW measurements. In Section B.3.2 we confirm the back-of-the-envelope estimates with a Fisher matrix analysis for a few representative cases.

B.3.1 DWDs as accelerometers

If a DWD is moving with an apparent acceleration $a \equiv \dot{v}_{||}$, the time dependence of the GW frequency $f(t)$ registered by LISA (i.e., at the "observer") will be different from the intrinsic chirping $f_s(\tau)$ of the GW signal emitted by the DWD (i.e., at the "source"). We will assume that the observer's clock and the clock at the source are synchronized at the beginning of the observation – i.e., a GW signal that the observer starts receiving at

the initial time $t = 0$ was emitted at $\tau = 0$ by the source's clock. In this work we only consider effects linear in the (assumed small) DWD acceleration a. For simplicity we also assume the DWD orbits to be circular, and their inspiral to be driven purely by gravitational radiation.

The GW frequency drift exprienced by DWDs is slow, as evidenced by their long coalescence times:

$$\begin{aligned} \tau_{\rm c} &= \frac{5\mathscr{M}}{256}(\pi\mathscr{M} f_{\rm s0})^{-8/3} \\ &\approx 1.3\times 10^6\ {\rm yr}\left(\frac{\mathscr{M}}{0.44 M_\odot}\right)^{-5/3}\left(\frac{f_{\rm s0}}{2\ {\rm mHz}}\right)^{-8/3}, \end{aligned} \tag{B.5}$$

where $f_{\rm s0} = f_{\rm s}|_{\tau=0}$ is the initial frequency of the source, and $\mathscr{M} = (m_1 m_2)^{3/5}(m_1+m_2)^{-1/5}$ is the chirp mass, a function of the individual masses m_1 and m_2 of the binary components (e.g., $\mathscr{M} = 0.44 M_\odot$ for $m_1 = m_2 = 0.5 M_\odot$). From the (long) coalescence time and the nominal LISA observation time $T_{\rm obs} = 10$ yr [28–30] we can define a small parameter $\tau/\tau_{\rm c} \leq T_{\rm obs}/\tau_{\rm c} \sim 10^{-5}$, which gives rise to the expansion of the GW frequency at the source:

$$f_{\rm s}(\tau) = f_{\rm s0} + \dot{f}_{\rm s0}\tau + \ddot{f}_{\rm s0}\tau^2/2 + \ldots . \tag{B.6}$$

Indeed, if we estimate the derivatives $\dot{f}_{\rm s0} \sim f_{\rm s0}/\tau_{\rm c}$, $\ddot{f}_{\rm s0} \sim f_{\rm s0}/\tau_{\rm c}^2, \ldots$, the respective terms are $\dot{f}_{\rm s0}\tau \lesssim T_{\rm obs}/\tau_{\rm c}$, $\ddot{f}_{\rm s0}\tau^2 \lesssim (T_{\rm obs}/\tau_{\rm c})^2$, etc. More precisely, at the lowest post-Newtonian order [348, 349],

$$\begin{aligned} f_{\rm s}(\tau) &= f_{\rm s0}\left(1-\frac{\tau}{\tau_{\rm c}}\right)^{-3/8} \\ &= f_{\rm s0} + \frac{3}{8}(f_{\rm s0}/\tau_{\rm c})\,\tau + \frac{33}{128}(f_{\rm s0}/\tau_{\rm c}^2)\,\tau^2 + \ldots \end{aligned} \tag{B.7}$$

$$\Rightarrow \qquad \dot{f}_{\rm s0} = \frac{3}{8}\frac{f_{\rm s0}}{\tau_{\rm c}}, \quad \ddot{f}_{\rm s0} = \frac{33}{64}\frac{f_{\rm s0}}{\tau_{\rm c}^2}, \quad \ldots . \tag{B.8}$$

Apparent DWD acceleration causes the observed derivatives $\dot{f}_0$, $\ddot{f}_0, \ldots$, to differ from their counterparts at the source. In analogy with the well-known degeneracy between $f_{\rm s0}$ and a constant relative velocity $v_{||}$ (and the chirp mass), the first derivative $\dot{f}_{\rm s0}$ is fully degenerate with the apparent acceleration, as long as the motion is nonrelativistic. This can be illustrated by a source that is receding just fast enough to compensate for the GW frequency drift: the linear growth of the frequency due to the chirp $\dot{f}_{\rm s0}$ is balanced by the Doppler shift, which is also linear in case of a constant acceleration. Therefore, in order to break this degeneracy and determine the apparent acceleration from the GW signal alone, it is necessary to measure at least the second derivative $\ddot{f}_0$.

We now consider the observed frequency $f(t) = f_0 + \dot{f}_0 t + \ddot{f}_0 t^2/2 + \ldots$ and estimate how realistic it is to measure, more generally, the kth derivative $f_0^{(k)}$. We do so by calculating the respective dephasing, i.e., the contribution of a given derivative term to the GW phase

$$\psi(t) = 2\pi \int_0^t f(t')\,\mathrm{d}t' = 2\pi \left(f_0 t + \frac{1}{2!}\dot{f}_0 t^2 + \frac{1}{3!}\ddot{f}_0 t^3 + \ldots \right) . \tag{B.9}$$

Of course, the GW signal must be loud enough to be detected, but this is always the case for the population of resolved DWDs with SNR > 7 (see Section B.2.2). The contribution to the dephasing accumulated by the term proportional to $f_0^{(k)}$ during the observation time $T_{\rm obs}$ can be estimated from:

$$\delta\psi_k \equiv \frac{2\pi}{(k+1)!} f_0^{(k)} T_{\rm obs}^{k+1} = \frac{2\pi\,\delta f_k\, T_{\rm obs}}{k+1} \gtrsim 2\pi\,, \tag{B.10}$$

where we introduce the respective frequency drift $\delta f_k = f^{(k)} T_{\rm obs}^k/k!$, which is likely to be detected if it exceeds the typical size of a frequency bin, $\delta f_k \gtrsim 1/T_{\rm obs}$. Once again, estimating the derivatives as $f^{(k)} \sim f_0/\tau_{\rm c}^k$, we recast the above formula in terms of the

zeroth-order contribution:

$$\delta\psi_k \sim \frac{2\pi f_0 T_{\rm obs}}{(k+1)!}\left(\frac{T_{\rm obs}}{\tau_{\rm c}}\right)^k \sim 10^{6-5k}\left(\frac{f_0 T_{\rm obs}}{10^6}\right)\left(\frac{T_{\rm obs}/\tau_{\rm c}}{10^{-5}}\right)^k, \tag{B.11}$$

where the normalization values are typical of a $0.5M_\odot + 0.5M_\odot$ DWD that emits at 2 mHz (see Eq. (B.5)). For such a binary, the chirp $\dot{f}_0$ is likely measurable ($\delta\psi_1 \gtrsim 1$), whereas the second derivative $\ddot{f}_0$ is not ($\delta\psi_2 \ll 1$).

Figure 5.3 shows the GW frequency–chirp mass plane with three contours of constant $\delta\psi_k = 2\pi$ for $k = 1$ (solid red line), $k = 2$ (dashed), and $k = 3$ (dotted). The contours correspond to the criterion of sufficient dephasing for reliable measurement of the kth derivative, Eq. (B.10), with sources with a smaller dephasing lying to the left of the respective line. We also overlay the synthetic population described in Section B.2.2. In addition to the DWDs and verification binaries (VB), here we also include binary neutron stars (BNS), black hole–neutron star binaries (BH–NS), and binary black holes (BBH). There is clearly a sizeable portion of the DWD population (as well as a few compact binaries) with measurable $\dot{f}_0(k=1)$. By contrast, one can hope to measure $\ddot{f}_0(k=2)$ only for a few DWDs, while measuring the higher derivative $f_0^{(3)}(k=3)$ seems unlikely with LISA over a 10 yr observation period. For other types of compact binaries, $\ddot{f}_0$ may be detectable for ~ 1 source, whereas detecting higher derivative is unlikely. Note, however, that the dephasing criterion is approximate, so measurements may still be possible for sources with high SNR.

To summarize: out of all resolved DWDs observable by LISA, there is likely only a few for which the derivative parameter $\ddot{f}_0$ can be measured independently of $\dot{f}_0$ from GWs alone, thereby lifting the degeneracy between the GW chirp $\dot{f}_{\rm s0}$ and the acceleration a, and enabling DWD accelerometry. We now proceed to provide quantitative estimates of the measurement uncertainties.

B.3.2 Fisher uncertainties

We can make the previous arguments more quantitative by calculating the apparent acceleration uncertainty for a few representative DWD sources using the Fisher information matrix. We begin with the conservative case in which we try to determine the acceleration using only GW observations. As discussed in the previous section, this amounts to measuring the second derivative $\ddot{f}_0$ and lifting the $\dot{f}_{s0}$–a degeneracy. We then consider another way to break that degeneracy, which is to ascertain one of the characteristic parameters of a DWD from EM observations. We consider both the case in which only the DWD chirp mass $\mathscr{M}$ is assumed to be known, as well as a "best-case scenario" in which all parameters are known except for the acceleration.

For the Fisher matrix analysis, we assume a TD waveform

$$h(t) = A\cos\psi(t)\,, \tag{B.12}$$

$$\psi(t) = \psi_0 + 2\pi\left(f_0 t + \frac{1}{2}\dot{f}_0 t^2 + \frac{1}{6}\ddot{f}_0 t^3\right), \tag{B.13}$$

where the amplitude A is approximately constant, and ψ_0 is the initial phase. The GW signal is also assumed to have been averaged over the angles that characterize the sky position of the source and its orbital orientation. In what follows we carry out the calculation in the FD, where the waveform reads

$$h_F = \begin{cases} \dfrac{1}{2}\dfrac{A}{\sqrt{\dot{f}\,[t(F)]}}e^{i\frac{\pi}{4}+i(\psi_0+\psi_F)}\,, & f_0 \le F \le f(T_{\rm obs})\,, \\ \\ 0\,, & \text{otherwise}\,. \end{cases} \tag{B.14}$$

Here we use the uppercase F for the Fourier frequency, and we denote the FD waveform by the subscript F. Explicit expressions for the functions $t(F)$ and ψ_F are provided in

Appendix B.8, where we also describe our numerical setup and compare three different versions of the Fisher matrix calculation (the FD, the TD, and a discretized version that emulates data processing in LISA).

The Fisher matrix F_{ij} for a source with characteristic parameters θ_i is defined in terms of the inner product between two FD waveforms as follows:

$$\left(h_F^{(1)}\middle|h_F^{(2)}\right) = \mathscr{C}^2 \mathrm{Re}\int_0^{+\infty} \frac{h_F^{(1)}\left(h_F^{(2)}\right)^*}{S_\mathrm{n}(F)}\,\mathrm{d}F\,, \tag{B.15}$$

$$F_{ij} \equiv \left(\frac{\partial h_F}{\partial\theta_i}\middle|\frac{\partial h_F}{\partial\theta_j}\right), \tag{B.16}$$

where S_n is the noise power spectral density measured by LISA [48, 375], and the factor $\mathscr{C}$ absorbs all non-essential numerical constants. The inverse of the Fisher matrix (or "correlation matrix") is

$$\langle\sigma_i\sigma_j\rangle = \left(F^{-1}\right)_{ij}, \tag{B.17}$$

where the angular brackets stand for the expectation value over realizations of the noise, and its diagonal components yield the uncertainties σ_i on each of the parameters θ_i. In what follows we also use ε_i to denote the relative uncertainty of a parameter, or equivalently, the uncertainty on the logarithm of the parameter:

$$\varepsilon_i \equiv \frac{\sigma_i}{\theta_i} = \sigma_{\ln\theta_i}\,. \tag{B.18}$$

For the quasimonochromatic sources under consideration, it is convenient to normalize

the uncertainties by the SNR [401, 431]:

$$\begin{aligned} \mathrm{SNR}^2 &\equiv (h_F|h_F) = \mathscr{C}^2 \int_{f_0}^{f_0+\delta f} \frac{|h_F|^2}{S_\mathrm{n}(F)}\,\mathrm{d}F \\ &\approx \left(\frac{1}{2}\mathscr{C}A\right)^2 \frac{\delta f}{\dot{f}_0 S_\mathrm{n}(f_0)} \approx \left(\frac{1}{2}\mathscr{C}A\right)^2 \frac{T_\mathrm{obs}}{S_\mathrm{n}(f_0)}\,, \end{aligned} \tag{B.19}$$

or

$$\mathrm{SNR} = \frac{1}{2}\mathscr{C}A\sqrt{\frac{T_\mathrm{obs}}{S_\mathrm{n}(f_0)}}\,, \tag{B.20}$$

where δf is the total change in frequency during the observation time, and we have neglected terms of the order of $\delta f/f_0 \sim T_\mathrm{obs}/\tau_\mathrm{c} \ll 1$. Note that the amplitude A is constant in the same approximation (see e.g. Ref. [426]).

We compute Fisher matrices and the respective uncertainties for the following sets of parameters:

(1) $\theta_i^{(1)} = \{\ln A, \ln f_0, \ln \dot{f}_0, \ln \ddot{f}_0, \psi_0\}$.

(2) $\theta_i^{(2)} = \{\ln A, \ln f_{\mathrm{s}0}, \ln \dot{f}_{\mathrm{s}0}, a, \psi_0\}$.

In order to obtain the change of variables between $\theta_i^{(2)}$ and $\theta_i^{(1)}$, we relate the observed frequency and its derivatives to their counterparts at the source. Since a constant velocity can be absorbed into redefinitions of the GW frequency and acceleration, we set the initial velocity $v_{||,0} = 0$. Then, as shown in Appendix B.7, the line-of-sight distance to the source is

$$D(\tau) = D_0 + \frac{1}{2}a\tau^2\,, \tag{B.21}$$

where D_0 is the distance at which the GW signal is first detected. Due to the light travel time effect [234, 235] (see also [33]), the times at the observer and at the source

are related as follows (see Fig. B.1):

$$\begin{aligned} t &= \tau + D(\tau) - D_0\,, \\ t &= \tau + \frac{1}{2} a\tau^2\,. \end{aligned} \tag{B.22}$$

Since the number of full-period waves emitted by the source is the same as the number received by the observer, the GW phase is invariant:

$$\begin{aligned} \psi(t) &= \psi_{\rm s}(\tau)\,, \\ 2\pi \int_0^t f(t')\,{\rm d}t' &= 2\pi \int_0^\tau f_{\rm s}(\tau')\,{\rm d}\tau'\,, \end{aligned} \tag{B.23}$$

where t and τ are related by Eq. (B.22). Differentiating both sides w.r.t. the observer's time t, we obtain [81, 307, 376, 433]:

$$f(t) = \frac{f_{\rm s}(\tau)}{{\rm d}t/{\rm d}\tau} = \frac{f_{\rm s}\left[\tau(t)\right]}{1 + a\tau(t)}\,, \tag{B.24}$$

where $\tau(t)$ is the inverse of $t(\tau)$. Therefore,

$$f_0 = f_{\rm s0}\,, \tag{B.25}$$

$$\dot{f}_0 = \dot{f}_{\rm s0} - a f_{\rm s0}\,, \tag{B.26}$$

$$\begin{aligned} \ddot{f}_0 &= \ddot{f}_{\rm s0} - 3a\dot{f}_{\rm s0} + \mathscr{O}(a^2 f_{\rm s0}) \\ &\approx \frac{11}{3}\frac{\dot{f}_{\rm s0}^2}{f_{\rm s0}} - 3a\dot{f}_{\rm s0}\,, \end{aligned} \tag{B.27}$$

where we used Eq. (B.8) to relate the derivatives at the source. We can estimate the relative correction due to acceleration as $a f_{\rm s0}/\dot{f}_{\rm s0} \sim a\tau_{\rm c} \ll 1$. Note that an overdot means that the frequencies are differentiated with respect to their own times: t for the

observer and τ for the source.

The final change of variable reads:

$$\ln f_0 = \ln f_{s0}\,, \tag{B.28}$$

$$\ln \dot{f}_0 = \ln \dot{f}_{s0} - a e^{\ln f_{s0} - \ln \dot{f}_{s0}}\,, \tag{B.29}$$

$$\ln \ddot{f}_0 = 2\ln \dot{f}_{s0} - \ln f_{s0} - \frac{9}{11} a e^{\ln f_{s0} - \ln \dot{f}_{s0}}\,, \tag{B.30}$$

where we have omitted a constant that does not contribute to the Jacobian between $\theta_i^{(2)}$ and $\theta_i^{(1)}$.

(3) $\theta_i^{(3)} = \{\ln \mathscr{M}, \ln D, \ln \tau_c, a, \psi_c/\beta\}$, with

$$\psi_c \equiv \psi_0 + \frac{1}{16}(\pi \mathscr{M} f_{s0})^{-5/3}\,, \tag{B.31}$$

$$\beta \equiv 2\pi f_{s0} \tau_c = \frac{5}{128}(\pi \mathscr{M} f_{s0})^{-5/3}\,, \tag{B.32}$$

where ψ_c is the coalescence phase, and the factor β is introduced for numerical convenience. Using Eq. (B.5) and $A \approx \mathscr{M}^{5/3} f_{s0}^{2/3}/D$, the change of variables between $\theta_i^{(3)}$ and $\theta_i^{(2)}$ (to within an additive constant) reads

$$\ln A = \frac{5}{4}\ln \mathscr{M} - \frac{1}{4}\ln \tau_c - \ln D\,, \tag{B.33}$$

$$\ln f_{s0} = -\frac{5}{8}\ln \mathscr{M} - \frac{3}{8}\ln \tau_c\,, \tag{B.34}$$

$$\ln \dot{f}_{s0} = -\frac{5}{8}\ln \mathscr{M} - \frac{11}{8}\ln \tau_c\,, \tag{B.35}$$

$$\psi_0 = \beta\left(\frac{\psi_c}{\beta} - \frac{8}{5}\right). \tag{B.36}$$

GWs alone. Table B.2 shows the results of a FD calculation of Fisher uncertainties for the sets of parameters $\theta_i^{(1)}$ (top) and $\theta_i^{(2)}$ (bottom), assuming no additional information beyond

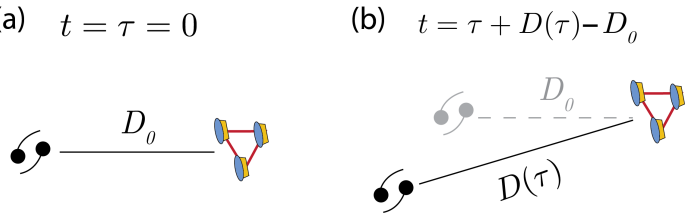

Figure B.1: (a) Beginning of DWD GW observation by LISA. (b) Time t_s passes according to a clock at the source. We assume that the displacement of the source is much less than the source distance D at any point during the LISA observation.

Table B.2: Fisher uncertainties (diagonal) and correlation coefficients (off-diagonal) for two sets of characteristic DWD GW parameters, respectively: $\theta_i^{(1)} = \left\{\ln A, \ln f_0, \ln \dot{f}_0, \ln \ddot{f}_0, \psi_0\right\}$ (top) and $\theta_i^{(2)} = \left\{\ln A, \ln f_{s0}, \ln \dot{f}_{s0}, a, \psi_0\right\}$ (bottom). We assume SNR $= 1000$, with $\mathscr{M} = 0.44 M_\odot$, $f_0 = 2$ mHz, $T_{\rm obs} = 10$ yr.

$\theta_i^{(1)}$	ε_A	ε_{f_0}	$\varepsilon_{\dot{f}_0}$	$\varepsilon_{\ddot{f}_0}$	σ_{ψ_0}
ε_A	0.001^*	0^*	0^*	0^*	0^*
ε_{f_0}		8.741×10^{-9}	-0.97	0.92	-0.87
$\varepsilon_{\dot{f}_0}$			**0.01375**	**−0.99**	0.75
$\varepsilon_{\ddot{f}_0}$				**2504**	-0.66
σ_{ψ_0}					0.004
$\theta_i^{(2)}$	ε_A	$\varepsilon_{f_{s0}}$	$\varepsilon_{\dot{f}_{s0}}$	σ_a [m/s^2]	σ_{ψ_0}
ε_A	0.001^*	0^*	0^*	0^*	0^*
$\varepsilon_{f_{s0}}$		8.741×10^{-9}	0.92	0.92	-0.87
$\varepsilon_{\dot{f}_{s0}}$			**2119**	**1**	-0.66
σ_a [m/s^2]				**0.006**	-0.66
σ_{ψ_0}					0.004

the measured GW waveform. Recall that the first set includes the observed derivatives $\dot{f}_0$ and $\ddot{f}_0$, while in the second set they are converted to the source value $\dot{f}_{s0}$ and the acceleration a. Uncertainties on these parameter sets are related by the Jacobian for the change of variables given in Eqs. (B.28)–(B.30), and the calculation is performed for a loud quasi-monochromatic source with $\mathscr{M} = 0.44 M_\odot$, $f_0 = 2$ mHz, $T_{\rm obs} = 10$ yr, and SNR $= 1000$. Comparing the values highlighted in bold makes emphasizes quantitatively that the double derivative $\ddot{f}_0$ is difficult to measure, resulting in a high uncertainty for the apparent acceleration. To reiterate: if we do not include $\ddot{f}_0$ in the set of Fisher matrix parameters, there is complete degeneracy between $\dot{f}_{s0}$ and a, because we can only measure their combination $\dot{f}_0$, Eq. (B.26). The inclusion of $\ddot{f}_0$ introduces a linearly independent combination, Eq. (B.27), breaking the degeneracy in principle, but this additional parameter is poorly determined for realistic DWD parameters: while $\dot{f}_0$ is measured well ($\approx 1\%$), there are large uncertainties for $\dot{f}_{s0}$ and a from the inversion of Eqs. (B.26) and (B.27).

GWs + EM observations. The situation improves significantly if an independent measurement of either the DWD chirp mass $\mathscr{M}$ or distance D is available from EM observations. If the chirp mass is known, it relates the time derivative $\dot{f}_{s0}$ to the frequency $f_{s0} = f_0$, which is always measured very well. A reasonably good measurement of $\dot{f}_0$ then leads to a dramatic improvement in σ_a. If, instead, the distance is known, the chirp mass can be inferred from the amplitude A, whose uncertainty is relatively low (see Table B.2). Knowing the chirp mass again makes it possible to infer the acceleration with low uncertainty (i.e., small σ_a).

Tables B.3 and B.4 show the apparent acceleration uncertainty σ_a at SNR $= 1000$ when the chirp mass $\mathscr{M}$ is either included or excluded from the vector of parameters $\theta_i^{(3)}$. For the fiducial values of the parameters, we choose the combinations $\mathscr{M} = 0.44 M_\odot$, $f_0 = 2$ mHz and $\mathscr{M} = M_\odot$, $f_0 = 5$ mHz, while for the observation time we use either $T_{\rm obs} = 4$ yr or $T_{\rm obs} = 10$ yr. Note that the uncertainty improves $\propto T_{\rm obs}^{-2}$ (at fixed SNR, i.e., not accounting for the scaling SNR$^{-1} \propto T_{\rm obs}^{-1/2}$) as one may expect from dimensional considerations. We

Table B.3: Apparent acceleration uncertainty $\sigma_{\rm a}$ [m/s^2] for a set of characteristic DWD GW parameters with the chirp mass *included*: $\theta_i^{(3)} = \{\ln \mathscr{M}, \ln D, \ln \tau_{\rm c}, \psi_{\rm c}/\psi_0, a\}$. Fiducial values of the chirp mass, GW frequency, and observation time are shown; we assume SNR $= 1000$ and $\psi_0 = 0$.

Time domain, $\mathscr{M} \in \theta_i^{(3)}$	$\mathscr{M} = 0.44 M_\odot$ $f_0 = 2$ mHz	$\mathscr{M} = 1 M_\odot$ $f_0 = 5$ mHz
$T_{\rm obs} = 4$ yr	6.73×10^{-2}	5.47×10^{-4}
$T_{\rm obs} = 10$ yr	4.30×10^{-3}	2.04×10^{-5}

Table B.4: Apparent acceleration uncertainty $\sigma_{\rm a}$ [m/s^2] for a set of characteristic DWD GW parameters with the chirp mass *excluded*: $\theta_i^{(3)} = \{\ln D, \ln \tau_{\rm c}, \psi_{\rm c}/\psi_0, a\}$. Fiducial values of the chirp mass, GW frequency, and observation time are shown; we assume SNR $= 1000$ and $\psi_0 = 0$.

Time domain, $\theta_i^{(3)} \setminus \{\mathscr{M}\}$	$\mathscr{M} = 0.44 M_\odot$ $f_0 = 2$ mHz	$\mathscr{M} = 1 M_\odot$ $f_0 = 5$ mHz
$T_{\rm obs} = 4$ yr	2.84×10^{-8}	1.14×10^{-8}
$T_{\rm obs} = 10$ yr	4.54×10^{-9}	1.82×10^{-9}

also find that the uncertainty barely depends on the exact value of a as long as Galactic accelerations are concerned, which is why we assume $a = 0$ in this calculation.

A best-case scenario. In an ideal situation, all parameters of the source would be known exactly, except for the acceleration. The TD Fisher "matrix" (see Appendix B.8) then

consists of a single element:

$$\begin{aligned} F_{\rm aa} &= \mathscr{C}^2 \int_0^{T_{\rm obs}} \frac{(\partial_a h)^2}{S_n[f(t)]}\,{\rm d}t \approx \frac{(\mathscr{C}A)^2}{2S_n(f_0)}(\pi f_0)^2 \int_0^{T_{\rm obs}} {\rm d}t\, t^4 \sin^2\psi \\ &\approx {\rm SNR}^2 \times \frac{(\pi f_0)^2}{T_{\rm obs}} \int_0^{T_{\rm obs}} {\rm d}t\, t^4 (1-\cos 2\psi) \\ &\approx {\rm SNR}^2\, T_{\rm obs}^4 \times \frac{(\pi f_0)^2}{5}, \end{aligned} \tag{B.37}$$

where we neglect $t/\tau_{\rm c} \lesssim T_{\rm obs}/\tau_{\rm c} \ll 1$ and $\mathscr{O}[(f_0 T_{\rm obs})^{-1}] \ll 1$ terms. Then, the acceleration uncertainty is given by:

$$\begin{aligned} \sigma_{\rm a} &= \frac{1}{\sqrt{F_{\rm aa}}} = \frac{1}{\rm SNR}\frac{1}{T_{\rm obs}^2}\frac{\sqrt{5}}{\pi f_0} \\ &\approx 10^{-9}\ {\rm m/s^2} \left(\frac{\rm SNR}{1000}\right)^{-1} \left(\frac{T_{\rm obs}}{10\ {\rm yr}}\right)^{-2} \left(\frac{f_0}{2\ {\rm mHz}}\right)^{-1}. \end{aligned} \tag{B.38}$$

This estimate gives a lower limit on the uncertainty. Indeed, as we include more parameters in the Fisher matrix we introduce more correlations, which leads to higher uncertainties on the individual parameters.

As the results of this section suggest, measuring the Galactic acceleration with GWs alone appears to be unlikely with LISA. The typical values of the uncertainty in this case (see Table B.3) are orders of magnitudes higher than the typical acceleration: see Fig. 5.1. When the chirp mass is known, the uncertainty improves dramatically, although it is still an order of magnitude worse than the typical magnitude of Galactic acceleration.

There is still some hope: since we are interested in large-scale Galactic accelerations, the accelerations of the individual DWDs in the population must be correlated, which should allow improvement of the overall uncertainty. We discuss this possibility in the

next section.

B.4 Galactic accelerometry with gravitational waves

In this section we present the distribution of measurement uncertainties for the synthetic DWD population described in Section B.2.2 above. We then discuss the prospects of measuring their acceleration by leveraging the large number of Galactic DWDs and using additional information from EM observations. To model the correlation between the accelerations of individual DWDs, we introduce an overall normalization factor, $\mathscr{N}$, of the Galactic gravitational potential. Effectively, the parameter $\mathscr{N}$ encodes a linear scaling with the total mass of the Milky Way:

$$\Phi = \mathscr{N}\Phi_{\rm model}\,, \tag{B.39}$$

where $\Phi_{\rm model}$ is defined in Eqs. (B.1) and (B.2). Since $a = -\nabla\Phi$ and $v^2 = R\,\partial\Phi/\partial R$ (see Section B.2.1), normalizing the gravitational potential also normalizes the apparent acceleration as $a = \mathscr{N}\,a_{\rm model}$.

The GW signals from multiple resolvable DWDs located at different distances from the Galactic center can be used to collectively pin down the parameter $\mathscr{N}$ as follows. Consider a number n of DWDs that are used to determine $\mathscr{N}$. Then, if each DWD source is described by k parameters (chirp mass, distance, etc.), we can calculate a large Fisher matrix of size $(nk+1)\times(nk+1)$ for the global parameter vector $(\mathscr{N},\theta_1,\theta_2,\ldots,\theta_n)$, where θ_i is the parameter vector of the ith source. If we assume that the narrow GW frequency bands swept by any two DWDs do not overlap, the Fisher matrix reduces to n blocks of individual $k\times k$ Fisher matrices, with the first row and column (of "size" $1\times(nk+1)$ and $(nk+1)\times 1$, respectively) encoding correlations between the parameter $\mathscr{N}$ and the individual

sets of parameters θ_i $(i = 1, \ldots, n)$. It then follows that the reciprocals of the individual uncertainties add in quadrature to provide an improvement that scales with $1/\sqrt{n}$. The parameter $\mathscr{N}$ is considered measurable if the fractional error $\varepsilon_{\mathscr{N}} = \sigma_{\mathscr{N}}/\mathscr{N} < 1$, where $\mathscr{N} = 1$ corresponds to a fiducial model of the Milky Way such that $\Phi = \Phi_{\rm model}$. Conversely, if $\varepsilon_{\mathscr{N}} > 1$, the measurement only places an upper bound on the parameter $\mathscr{N}$.

We now proceed to present the results of our calculation; the details of our fast implementation can be found in Appendix B.8.

B.4.1 Distribution of measurement uncertainties

GWs alone. In Fig. 5.4 we show the distribution of measurement uncertainties for the synthetic DWD population. The left panel illustrates how the uncertanties change if the set of 4 parameters $(A, f_0, \dot{f}_0, \psi_0)$, shown in blue, is extended to include $\ddot{f}_0$ (red). The right panel is obtained by the change of variables defined by Eqs. (B.26)–(B.27) from the set of parameters $(f_0, \dot{f}_0, \ddot{f}_0)$, shown in red as before, to $(f_{\rm s0}, \dot{f}_{\rm s0}, \mathscr{N})$, now shown in purple; it illustrates the effect of including $\mathscr{N} = a/a_0$ as an extra parameter in the set $(A, f_{\rm s0}, \dot{f}_{\rm s0}, \psi_0)$. Here a_0 stands for the acceleration in a fiducial Milky Way model. The relative uncertainties quoted above the top-right subplots correspond to the extended parameter sets (distributions in purple).

As is evident from the left panel, while the parameter $\ddot{f}_0$ is far from being measurable, its inclusion in the Fisher matrix has little effect on the inference of other parameters. The parameters A and f_0 are well measured for most of the sources (at the level of $\varepsilon_A \lesssim 10\%$ and $\varepsilon_{f_0} \lesssim 10^{-6}$, respectively). The parameter $\dot{f}_0$ is only measurable at the level of $\varepsilon_{\dot{f}_0} \lesssim 10\%$ for some of the sources. However, as we change variables from $(f_0, \dot{f}_0, \ddot{f}_0)$ to $(f_{\rm s0}, \dot{f}_{\rm s0}, \mathscr{N})$, the source frequency $\dot{f}_{\rm s0}$ and normalization factor $\mathscr{N}$ become essentially unmeasurable. By contrast, the observed time derivative $\dot{f}_0$ can be measured at the 10% level or better for

a significant fraction of the sources. This is once again a manifestation of the degeneracy between f_{s0} and a: the linear combination $\dot{f}_0 = \dot{f}_{s0} - \mathscr{N} a_0 f_{s0}$ is measured more precisely than the individual parameters of interest.

GWs + EM observations. In Fig. 5.5 we show a comparison of the distribution of measurement uncertainties for the same synthetic DWD population, for the case of five parameters $(\mathscr{N}, \mathscr{M}, D, f_{s0}, \psi_0)$ (purple) and the case of four parameters in which the chirp mass $\mathscr{M}$ is known (from EM observations) but has been excluded (green) from the Fisher matrix calculation. Note that the uncertainty in chirp mass is not shown, and the five-parameter case is the same as in right panel of Fig. 5.4 (red), but with the parameters $(A, \dot{f}_{s0})$ traded for $(\mathscr{M}, D)$.

Clearly, as the number of parameters is reduced, the uncertainties improve dramatically. When the chirp mass is included in the parameter set to be estimated, neither $\mathscr{N}$ nor $\mathscr{M}$ can be determined with significance, which is another manifestation of the degeneracy between $\dot{f}_{s0}$ and a. Since $\dot{f}_{s0}$ is not easy to measure, there is hardly a way to determine $\mathscr{M}$ from GWs alone. This translates into a large uncertainty in the source distance D, even though the amplitude $A \propto \mathscr{M}^{5/3} f_{s0}^{2/3} / D$ is known to within $\approx 10\%$ (the GW frequency f_{s0} itself can always be measured). However, if we know $\mathscr{M}$ (for example, from optical observations), those degeneracies are lifted.

The fact that the parameter $\mathscr{N}$ gives rise to correlations among the accelerations of individual DWDs does not remedy the problem. The uncertainty on the normalization parameter is $\varepsilon_{\mathscr{N}} \sim 10^9$ (see Fig. 5.4, right panel), and we can only expect an improvement by a factor of order $\sqrt{n} \sim 10^2$ times if we take the whole LISA DWD population into account. Given that determining the Galactic acceleration from GWs alone does not appear to be feasible, the role of combined GW–EM observations becomes crucial.

B.4.2 Prospects for multimessenger Galactic accelerometry

Additional information inferred from EM measurements can help to break degeneracies in DWD parameters inferred through GWs only. For example, depending on the inclination angle ι of the source, EM data can improve the estimate on the GW amplitude. It is also possible to have precise EM measurements of DWD GW chirp rate $\dot{f}_0$, e.g., via photometric time variability or spectroscopic radial-velocity shift measurements [404, 406]. In addition, astrometric measurements of source distance D (e.g., from Gaia), in combination with GW amplitudes A and frequencies f_0 observed by LISA, may enable inference of DWD chirp mass $\mathscr{M}$ [269].

EM counterparts of GW sources may be identified before, during, or after the LISA observation period. Prior to the start of LISA observation, detached DWDs can be discovered in high-cadence photometric surveys as periodically variable sources, if they are sufficiently edge-on. Mass-transferring and tidal-deforming DWDs will in general show photometric time variability; however we only consider detached DWDs in this work. With new data from current and upcoming astrometric [359], photometric [138, 141, 253, 291, 359, 497], and spectroscopic [160, 359, 440] surveys, the number of verification binaries is expected to grow to a significantly larger number by the time of LISA launch. The increased number of verification binaries will also increase the likelihood of finding several high-SNR (SNR $\sim 100-1000$) GW sources in the collection. Furthermore, the DWD localization provided by GW measurements, if accurate enough, may allow identification of the EM counterparts through EM follow-up observations after LISA's launch. The analysis of Ref. [285] shows that up to several hundreds of EM counterparts can be found in this way. We suggest that an efficient approach involves GW localization followed by targeted EM follow-up, focusing on high-SNR, well-localized sources (since the highest SNR sources dominate the accelerometry analysis, as discussed below). According to Ref. [430],

the GW localization volume for high-SNR ($\gtrsim 100$) DWD sources is typically $\lesssim 10$ pc^3. The expected number of enclosed DWDs within this localization volume is less than one, based on their number density [225]. Therefore, such a localization range offers a feasible target for coordinated EM observations. Further characterization of this proposed method is part of ongoing work to support future multimessenger observations.

We now forecast how the relative error in the normalization of the Galactic potential $\varepsilon_{\mathscr{N}} = \sigma_{\mathscr{N}}/\mathscr{N}$ improves as surveys of the EM counterparts of LISA sources become more complete. For this estimate, we use the synthetic DWD population discussed in Sec. B.2.2. LISA sources located closer to the Sun will presumably have EM counterparts discovered earlier in magnitude-limited surveys. We assume for simplicity that at any given time the EM surveys have a certain coverage distance; and, as such, there is a spherical volume centered at the Sun (with radius given by this coverage distance) within which *all* LISA sources have their EM counterparts identified.

Figure 5.6 shows how $\varepsilon_{\mathscr{N}}$ improves as a function of the coverage distance, assuming that EM measurements determine either (1) $\mathscr{M}$ only (left panel), or (2) all parameters except $\mathscr{N}$ (right panel), i.e., $\{\mathscr{M}, D, f_{s0}, \psi_0\}$. In both cases we see that, as the coverage distance grows, the relative error $\varepsilon_{\mathscr{N}}$ decreases, owing to the growing number of EM counterparts (recall that the reciprocals of individual uncertainties add in quadrature: see Section B.4). The gradual decrease in the cumulative error is occasionally interrupted by sharp drops whenever a DWD with very high SNR (up to ~ 1000) is included in the coverage. In case (1), we find that the relative error asymptotes to $\varepsilon_N \approx 2$ at coverage distance $\gtrsim 10$ kpc. This suggests that even after all of the EM counterparts have been found, the parameter $\mathscr{N}$ is not quite measureable (but almost so). On the other hand, in case (2), the estimated value of $\varepsilon_{\mathscr{N}}$ is about one order magnitude lower than in case (1), and the parameter $\mathscr{N}$ is measurable once there is identification of $\sim 10^3$ EM counterparts within a few kpc. This is an encouraging result, as the current catalog of verification binaries already

includes DWDs with distances of a few kpc [269].

Given this analysis, using LISA observations for Galactic accelerometry appears feasible as part of a multimessenger effort. Another avenue for improvement is to take into account the correlation between the acceleration and location of a GW source in the Galaxy, encoded in its distance and sky position; we leave this more sophisticated analysis to future work. Also, our forecast is based on current expectations for LISA sensitivity and observation period. If the level of noise in LISA is lower than assumed here, which is possible given the encouraging results from LISA Pathfinder [43], this will further reduce measurement uncertainties. We also note that using synthetic DWD populations models different from the one discussed in Sec. B.2.2 would yield slightly different results. For example, the exact distances of the highest-SNR sources can vary among different DWD populations. Nevertheless, we expect the general trends described above to remain the same.

B.5 Systematics

Here we discuss various effects not included in our analysis that may affect the binary evolution and the resulting gravitational waveform. Many sources of systematics relevant to our analysis are also found in the context of pulsar timing [167].

Tertiary perturber. While all DWDs in our Galaxy are under the influence of the overall Galactic gravitational potential, the local gravitational environment for a given DWD may be dominated by the presence of nearby tertiary objects. These could be any relatively small-scale inhomogeneities in the Galaxy, such as satellite galaxies, globular clusters, stars, or planets.

The possible effects of a single tertiary object on the GW signal emitted by a binary have been quantified in the past by several authors (see, e.g., [307, 376, 402, 403, 427, 432,

433, 484]). In summary, the gravitational influence of a tertiary object causes the center of mass of the GW-emitting binary to follow a Keplerian orbit whose period can be shorter or longer than the 4-10 yr LISA observation time. Roughly speaking, in the former case the tertiary perturber will induce a distinct, periodic signal, which can in principle be modeled; while in the latter case the induced acceleration is nearly constant, and can mimic the Galactic acceleration if the magnitude of the induced acceleration is $\sim 10^{-10}$ m/s^2. A star of typical mass $m_3 \sim M_\odot$ located at a typical distance $r_3 \sim 1$ pc from a DWD imparts only a tiny acceleration of order $m_3/r^2 \sim 10^{-13}$ m/s^2. However, in a fraction of cases, stars or other objects lie close enough to yield significant accelerations to DWDs of interest during the LISA observation period. In particular, recent population-synthesis simulations suggest that $\mathcal{O}(1)$ fraction of nearby DWDs within 20 pc from the Sun are part of a hierarchical triple with a distant tertiary companion [376, 441]. That said, the statistics of three-body systems involving DWDs are yet to be confirmed–nor has the resulting effect on GW estimates of Galactic acceleration–since only a small number of such systems have been observed so far.

Relativistic and propagation effects. A key step in deriving the apparent GW phase, as discussed above, is mapping the proper time of the GW-emitting binary to the corresponding arrival time at the solar system. The pulsar timing community routinely takes into account several effects that can result in a dephasing of the associated EM signal, in particular: (1) *Einstein delay*, i.e., the special relativistic and gravitational time dilation of the source's inner orbital period; (2) *Romer delay*, i.e., the variation in the path length of light due to the source's motion relative to the solar system; and (3) *Shapiro delay*, i.e., the delay in the arrival time of GWs when they are affected by the gravitational field of a massive body along their propagation path. The first time derivatives of these delays and the intrinsic frequency of the binary together determine the reference frequency f_0 of the GW signal, which, in the analysis above, we take to be the observed GW frequency at the beginning of

the LISA observation. In other words, the first time derivative effects of these delays are absorbed into the definition of f_0.

Non-gravitational interactions. We assume in our analysis that DWD binary evolution is driven purely by gravitational radiation. While most of the DWDs in the LISA band are expected to be compact and detached, some may undergo significant non-gravitational binary interactions [286]. Lower mass (i.e., less compact) WDs that reside in binaries with smaller orbital separations are prone to tidal deformations [405, 473] and mass transfers. Note, however, that although binary mass transfer contributes to systematic errors if not properly modeled, it can potentially be utilized to infer the individual masses of the WDs in a binary [480, 488], enabling inference of the chirp mass. The orbital evolution of DWDs may also be altered by EM radiation if at least one of the WDs is magnetic (about 20% of the total white dwarf population is expected to have strong magnetic fields, in the range $10^6 - 10^9$ G [86, 116, 294, 460]). In addition, DWD interactions with ambient matter (and possibly dark matter) can contribute to the dissipation of their orbital energies [112, 129, 200, 344]. The aforementioned effects would complicate the orbital evolution beyond what is expected from a purely GW-driven binary orbit shrinkage. There are, in fact, examples of known DWDs in the current catalog of LISA verification binaries whose evolution is inadequately described by gravitational radiation alone [294, 317]. A more complete modeling of the gravitational waveform should take into account such non-gravitational effects.

B.6 Conclusions

In this paper we explore the prospect of using the $\mathcal{O}(10^4)$ resolved double white dwarf (DWD) binaries that LISA is expected to observe as test mass accelerometers for probing the Milky Way gravitational potential. We assume a simple model for the Milky Way

gravitational field profile composed of a Miyamoto-Nagai disk, a Hernquist bulge, and a Navarro-Frenk-White dark matter halo. In order to realistically assess whether this technique can work in practice, we construct an artifical catalog of LISA-detectable DWDs using the FZ binary population synthesis model of Ref. [438]. We let the DWD binary motion follow the Galactic rotation curve as defined by the balance between their centrifugal force and the Galactic potential gradient, neglecting their velocity dispersions. The apparent line-of-sight acceleration of each source, namely the sum of its actual line-of-sight acceleration (assumed to follow the Milky Way gravitational field model) and the perspective acceleration due to its proper motion (assumed to follow the Galactic rotation curve), cause time-dependent changes to the arrival time of the associated GW signals, which manifest as Doppler modulations in the measured GW phase.

We quantify LISA's sensitivity to the motions of these sources with a Fisher matrix analysis, both in the time-domain and in the frequency domain. We first derive the time-domain gravitational waveform by relating it to the source-frame phase via a mapping between the observation time and the source-frame time. We then obtain the frequency-domain waveform using the stationary phase approximation. We perform the Fisher matrix analysis in both domains and find that the results agree. Our results show that strong correlations between the apparent acceleration of a source and its binary parameters undermine the ability to recover the apparent acceleration via GW-only measurements. This suggests the need of combining the GW analysis with other (independent) information about the binary parameters, e.g. by using detailed models of binary interactions [480, 488] or EM observations of the same sources [93, 258, 259, 405]. If we assume that (1) EM observations can provide independent and accurate measurements of DWD chirp masses and (2) the EM counterparts to all these LISA sources are identified and observed, our analysis indicates that it is nearly possible to determine the normalization $\mathscr{N}$ of the Milky Way gravitational potential model. If all DWD parameters other than $\mathscr{N}$ are measured electromagnetically, then $\mathscr{N}$

can be determined after finding about 10^3 EM counterparts. A more sophisticated analysis that accounts for correlations between the acceleration and position of a GW source in the Milky Way can further reduce measurement uncertainties. We also comment on possible sources of systematics that should be accounted for in more realistic future studies.

Previous works based on EM observations have utilized a variety of *dynamic* tracers to study different aspects of the Milky Way. These include radial stellar acceleration measurements through precision spectrographs [121, 177, 372, 413], angular stellar acceleration measurements through Gaia astrometry [103], peculiar acceleration measurements of globular clusters [361], pulsar timing [120, 219, 301, 315, 352], and the timing of eclipses in binaries [121]. Different tracers have different kinematic distributions and biases, with some correlation to their age, metallicity, and location. These tracers offer different trade-offs, and so provide complementary information when considered collectively.

B.7 Appendix: Perspective acceleration

For a small source displacement $\Delta D = |D(\tau) - D_0| \ll D_0$, we can approximately write

$$\begin{aligned} D &= \sqrt{\left(D_0 + \Delta D_\parallel\right)^2 + \Delta D_\perp^2} \\ &\approx D_0 \left(1 + \frac{\Delta D_\parallel}{D_0} + \frac{1}{2}\frac{\Delta D_\perp^2}{D_0^2}\right), \end{aligned} \tag{B.40}$$

where $\Delta D_\parallel$ and $\Delta D_\perp$ are the source displacements parallel and perpendicular to the line of sight given by the initial position D_0, and we have also neglected higher-order terms $\sim (\Delta D/D_0)^3$. If the source is moving with a constant acceleration $\mathbf{a}$ in its local frame,

$$\Delta D(\tau) = v_0 \tau + \frac{1}{2} a \tau^2, \tag{B.41}$$

where $\mathbf{v}_0$ is the initial velocity in its local frame, then the change in the distance reads

$$D(\tau) - D_0 = v_{\parallel,0}\tau + \frac{1}{2}\left(a_{\parallel,0} + \frac{v_{\perp,0}^2}{D_0}\right)\tau^2 + \mathscr{O}(\tau^3)\,, \tag{B.42}$$

where the higher-order terms in time can be neglected, because a typical increment in the velocity during the observation time is much smaller than the Galactic velocity dispersion:

$$\begin{aligned} \Delta v &\sim a T_{\rm obs} \sim 10^{-10}\,{\rm m/s^2} \times 10\,{\rm yr} \\ &\sim 1\,{\rm cm/s} \ll v_0 \sim 100\,{\rm km/s}\,. \end{aligned} \tag{B.43}$$

B.8 Appendix: Details of the Fisher matrix calculation

Frequency-domain waveforms

Here we collect the FD counterparts of the sky-averaged TD waveforms used in this work. Recall that we use a capital F for the GW Fourier frequency, while $f = f(t)$ is reserved for the varying GW frequency in the TD. Also, the subscript F indicates a FD waveform which, in the stationary phase approximation, is obtained as follows:

$$\begin{aligned} h_F &= \int_0^{T_{\rm obs}} {\rm d}t\, A\,[f(t)] \cos\left(\psi_0 + 2\pi\int_0^t {\rm d}t' f(t')\right) e^{-2\pi i F t} \\ &= \frac{1}{2}\int_0^{T_{\rm obs}} {\rm d}t\, A\,[f(t)] \exp\left\{ i\psi_0 + 2\pi i\int_0^t {\rm d}t' f(t') - 2\pi i F t \right\} \\ &\quad + \frac{1}{2}\int_0^{T_{\rm obs}} {\rm d}t\, A\,[f(t)] \exp\left\{ -i\psi_0 - 2\pi i\int_0^t {\rm d}t' f(t') - 2\pi i F t \right\} \\ &\approx \frac{1}{2} A\,[f(t_0)] \exp\left\{ i\psi_0 + 2\pi i\int_0^{t_0} {\rm d}t' f(t') - 2\pi i F t_0 \right\} \int_0^{T_{\rm obs}} {\rm d}t\, e^{i\pi\dot{f}(t_0)(t-t_0)^2}\,, \end{aligned} \tag{B.44}$$

where t_0 is the stationary point,

$$f(t_0) = F \quad \Leftrightarrow \quad t_0 = t(F)\,. \tag{B.45}$$

The stationary phase approximation also implies that, as long as $0 \leq t_0 \leq T_{\rm obs}$, we can extend the limits of integration in the last integral to infinity, whereas outside of that range, the integral, and therefore, the FD waveform, vanishes. Computing the resulting Gaussian integral and integrating by parts in the phase, we obtain:

$$h_F = \begin{cases} \dfrac{1}{2}\dfrac{A(F)}{\sqrt{\dot{f}\,[t(F)]}} e^{i\frac{\pi}{4}+i(\psi_0+\psi_F)}\,, & f_0 \leq F \leq f(T_{\rm obs})\,, \\ \\ 0\,, & \text{otherwise}\,, \end{cases} \tag{B.46}$$

$$\psi_F = -2\pi \int_{f_0}^{F} {\rm d}f'\, t(f')\,, \quad f_0 \equiv f(t=0)\,, \tag{B.47}$$

where $t(f)$ is the inverse of $f(t)$. For effects of windowing in the case of slowly chirping GW sources such as DWDs, see, for example, Appendix D of Ref. [426].

In a phenomenological framework, the GW frequency is represented as a Taylor expansion in time. For the purposes of this paper, we are only interested in the following two cases:

- $\underline{\dot{f} = \text{const}}$:

$$f = f_0 + \dot{f}_0 t \quad \Rightarrow \quad t(f) = \frac{f - f_0}{\dot{f}_0}\,, \tag{B.48}$$

$$\psi_F = -\frac{\pi\,(F - f_0)^2}{\dot{f}_0}\,. \tag{B.49}$$

- $\underline{\ddot{f} = \text{const}}$:

$$f = f_0 + \dot{f}_0 t + \frac{1}{2}\ddot{f}_0 t^2 \,, \tag{B.50}$$

$$t(f) = \frac{-\dot{f}_0 + \sqrt{\dot{f}_0^2 + 2\ddot{f}_0(f - f_0)}}{\ddot{f}_0}$$

$$\approx \frac{f - f_0}{\dot{f}_0} - \frac{1}{2}\frac{\ddot{f}_0 (f - f_0)^2}{\dot{f}_0^3} \,. \tag{B.51}$$

$$\psi_F \approx -\frac{\pi (F - f_0)^2}{\dot{f}_0} + \frac{\pi}{3}\frac{\ddot{f}_0 (F - f_0)^3}{\dot{f}_0^3} \,. \tag{B.52}$$

Implementation

In this section we provide details of our implementation of the Fisher matrix analysis. We also run a consistency check by comparing results from three versions of the calculation: the TD version, the FD version, and a version emulating the discrete nature of the LISA data stream.

To implement the calculation, we leverage the auto-differentiation and vectorization capabilities of the PYTHON package JAX [90]. Auto-differentiation makes use of the well-known derivative rules to evaluate arbitrarily complicated derivatives on the fly to within machine precision. JAX is also optimized for both CPUs and GPUs which, among other things, allows the user to vectorize a calculation, i.e., run it on all entries of an input array practically in parallel.

These properties make JAX a convenient tool for the Fisher matrix analysis on a population of DWDs. Indeed, the Fisher matrix for a GW signal, Eq. (B.16), can be recast as the Hessian of the scalar inner product, Eq. (B.15), and the operation of computing and

inverting the matrix can be vectorized and mapped across all DWDs in the population:

$$F_{ij} = \frac{1}{2}\frac{\partial^2}{\partial\theta_i\partial\theta_j}(\Delta h,\Delta h)\bigg|_{\theta=\overline{\theta}}, \tag{B.53}$$

$$\Delta h \equiv h(\theta)-h(\overline{\theta}), \tag{B.54}$$

where $h(\theta)$ is the waveform as a function of the parameters $\theta=\{\theta_i\}$, and the derivatives are evaluated at the fiducial values $\overline{\theta}$ of the parameters. As a side note, this Hessian form of the Fisher matrix is related to the linear-signal or high-SNR approximations (see e.g. [454]).

In a more realistic version, the integral is substituted for a sum over the data points, which takes into account the fact that the LISA data have to be discretely sampled with a timestep Δt. We assume $\Delta t = 1$ s. This results in a dataset of $T_{\rm obs}/\Delta t$ data points for a single datastream ($\approx 3\times10^8$ data points for the cadence $\Delta t = 1$ s and $T_{\rm obs} = 10$ yr).

We now provide the explicit expressions used in the TD version, the FD version, and the discretized version.

Time domain. The TD waveform $h(t)$, Eqs. (B.12) and (B.13), completes $\sim 10^5$ oscillations during the observation time, and the integration of such an oscillatory function can be challenging. For this reason we simplify the TD version of the Fisher matrix before we vectorize and evaluate it with JAX. The TD Fisher matrix reads:

$$\begin{aligned} F_{ij} &= \mathscr{C}^2\int_0^{T_{\rm obs}}\frac{\partial_i h(t)\partial_j h(t)}{S_n[f(t)]}\,{\rm d}t \\ &\approx \frac{{\rm SNR}^2}{A^2T_{\rm obs}}\int_0^{T_{\rm obs}}2(\partial_i h)(\partial_j h)\,{\rm d}t\,, \end{aligned} \tag{B.55}$$

where partial derivatives are taken w.r.t. the components of the parameter vector $\theta = \{\ln A, \ln f_0, \ln\dot{f}_0, \ln\ddot{f}_0, \psi_0\}$. If we neglect terms $\mathscr{O}(1/f_0T_{\rm obs})$, the matrix is effectively re-

duced to a 4×4 block. Indeed, for the cross-terms with $\ln A$ ($\theta_i \neq \theta_j = \ln A$),

$$F_{ij} \approx \mathrm{SNR}^2 \times \mathscr{O}\left(\frac{\partial_{\theta_i}\psi}{f_0 T_{\rm obs}}\right) \approx 0\,, \tag{B.56}$$

and the full matrix

$$F_{ij} \approx \mathrm{SNR}^2 \times \begin{pmatrix} 1 & 0 \\ & \\ 0 & F_{IJ} \end{pmatrix}, \tag{B.57}$$

where $\theta_{I,J} \neq \ln A$, and the 3×3 block

$$\begin{aligned} F_{IJ} &\equiv \int_0^{T_{\rm obs}} (\partial_I\psi)(\partial_J\psi)\frac{\mathrm{d}t}{T_{\rm obs}} \\ &= \frac{1}{2T_{\rm obs}}\left[\frac{\partial^2}{\partial\theta_i\partial\theta_j}\int_0^{T_{\rm obs}}(\Delta\psi)^2\mathrm{d}t\right]_{\theta=\overline{\theta}}, \end{aligned} \tag{B.58}$$

with $\Delta\psi \equiv \psi(\theta) - \psi(\overline{\theta})$.

Frequency domain. The inner product that goes into Eq. (B.53) reads

$$\begin{aligned} (\Delta h_F, \Delta h_F) &= \frac{1}{2}\mathrm{SNR}^2 \\ &\times \int_{-1}^{1}\left|e^{\ln A - (\ln\dot{f}_0 - \ln\overline{\dot{f}}_0)/2} e^{i\psi_F(\theta)} - e^{i\psi_F(\overline{\theta})}\right|^2 \mathrm{d}x\,, \end{aligned} \tag{B.59}$$

$$F = f_0 + \frac{1}{2}(x+1)\Delta f\,, \quad \Delta f \equiv f(T_{\rm obs}) - f_0\,, \tag{B.60}$$

where the phase is given by Eq. (B.52), and we have recast the integral in a form convenient for Gauss–Legendre quadrature. Note that we also neglect a variation in $\dot{f}$ in the amplitude,

which would result in a correction of the order of $T_{\rm obs}/\tau_{\rm c} \sim 10^{-5}$.

Discretized time domain. A discrete version of the TD inner product reads:

$$(\Delta h, \Delta h) \;\approx\; \mathrm{SNR}^2 \sum_{p=0}^{N} \Big(e^{\ln A} \cos\psi_p(\theta) - \cos\psi_p(\overline{\theta}) \Big)^2 \,, \tag{B.61}$$

where ψ_p is a TD phase evaluated at moments of time $t_p = p\Delta t$, and the number of datapoints N is given by the integer part of $T_{\rm obs}/\Delta t$. Again, we assume that the noise $S_{\rm n}[f(t_p)] \approx$ const for the quasimonochromatic sources considered in this paper. In the discrete TD version, we no longer neglect the off-diagonal terms as we did in the continuous case above, see Eqs. (B.56) and (B.57).

We compare Fisher matrix uncertainties obtained in the three approaches described above, and evaluated on the synthetic population of DWDs adopted in this paper. We find the following relative discrepancies (that can be thought of as "uncertainty on the uncertainties"):

- $\underline{\dot{f} = \text{const}}$, TD vs. FD: $\approx 10^{-11.5}$ across the parameter set $\{\ln A, \ln f_0, \ln \dot{f}_0, \psi_0\}$.
- $\underline{\dot{f} = \text{const}}$, TD vs. discretized TD: $\approx 10^{-7}$ for the same parameters.
- $\underline{\ddot{f} = \text{const}}$, TD vs. FD: $\approx 10^{-5}$ for the variables $\{\ln f_0, \ln \dot{f}_0, \ln \ddot{f}_0, \psi_0\}$, and $\approx 10^{-11}$ for $\ln A$.

In each of these cases, the scatter is ≈ 0.5 dex (i.e., less than an order of magnitude).

We also rely on JAX to switch between the sets of parameters $\theta^{(1)}$, $\theta^{(2)}$, $\theta^{(3)}$ listed in Section B.3.2. As is known, the results of a Fisher matrix calculation in one set of parameters θ_i can be converted to another set $\widetilde{\theta}_j$ by applying the Jacobian matrix $\widetilde{J}_{ij} \equiv \partial\widetilde{\theta}_i/\partial\theta_j$. Being a matrix of derivatives, the Jacobian naturally fits into the JAX autodifferentiation logic, as do the matrix transforms for a nonsingular Fisher matrix F and the

corresponding covariance matrix $\Sigma = F^{-1}$:

$$\widetilde{\Sigma} = \widetilde{J}\Sigma\widetilde{J}^{\mathrm{T}}, \qquad \widetilde{F} = \left(\widetilde{J}^{-1}\right)^{\mathrm{T}} F \widetilde{J}^{-1}. \tag{B.62}$$

All those operations are also easily vectorized in JAX.

Bibliography

[1] J. Aalbers, F. Agostini, M. Alfonsi, F.D. Amaro, C. Amsler, E. Aprile, L. Arazi, F. Arneodo, P. Barrow, L. Baudis, and et al. Darwin: towards the ultimate dark matter detector. *Journal of Cosmology and Astroparticle Physics*, 2016(11):017–017, Nov 2016.

[2] C. E. Aalseth, F. Acerbi, P. Agnes, I. F. M. Albuquerque, T. Alexander, A. Alici, A. K. Alton, P. Antonioli, S. Arcelli, R. Ardito, and et al. Darkside-20k: A 20 tonne two-phase lar tpc for direct dark matter detection at lngs. *The European Physical Journal Plus*, 133(3), Mar 2018.

[3] Benjamin P. Abbott et al. Sensitivity of the Advanced LIGO detectors at the beginning of gravitational wave astronomy. *Phys. Rev. D*, 93(11):112004, 2016. [Addendum: Phys.Rev.D 97, 059901 (2018)].

[4] L. F. Abbott and P. Sikivie. A Cosmological Bound on the Invisible Axion. *Phys. Lett. B*, 120:133–136, 1983.

[5] Mohammad Abdullah, Jonathan L. Feng, Sho Iwamoto, and Benjamin Lillard. Heavy bino dark matter and collider signals in the MSSM with vectorlike fourth-generation particles. *Phys. Rev. D*, 94(9):095018, 2016.

[6] C. Abel et al. Search for Axionlike Dark Matter through Nuclear Spin Precession in Electric and Magnetic Fields. *Phys. Rev. X*, 7(4):041034, 2017.

[7] Stefan Abel, Felix Eltes, J Elliott Ortmann, Andreas Messner, Pau Castera, Tino Wagner, Darius Urbonas, Alvaro Rosa, Ana M Gutierrez, Domenico Tulli, et al. Large pockels effect in micro-and nanostructured barium titanate integrated on silicon. *Nature materials*, 18(1):42–47, 2019.

[8] John Bishoy Sam Abraham, Brandon Adrian Aguirre, Jose L Pacheco, Gyorgy Vizkelethy, and E Bielejec. Fabrication and characterization of a co-planar detector in diamond for low energy single ion implantation. *Applied Physics Letters*, 109(6):063502, 2016.

[9] Javier F. Acevedo, Joseph Bramante, and Alan Goodman. Nuclear Fusion Inside Dark Matter. 12 2020.

[10] Michael R Ackerson, BO Mysen, ND Tailby, and EB Watson. Low-temperature crystallization of granites and the implications for crustal magmatism. *Nature*, 559(7712):94–97, 2018.

[11] Michael R Ackerson, Nicholas D Tailby, and E Bruce Watson. Trace elements in quartz shed light on sediment provenance. *Geochemistry, Geophysics, Geosystems*, 16(6):1894–1904, 2015.

[12] V. M. Acosta, E. Bauch, M. P. Ledbetter, C. Santori, K.-M. C. Fu, P. E. Barclay, R. G. Beausoleil, H. Linget, J. F. Roch, F. Treussart, S. Chemerisov, W. Gawlik, and D. Budker. Diamonds with a high density of nitrogen-vacancy centers for magnetometry applications. *Phys. Rev. B*, 80:115202, Sep 2009.

[13] V. M. Acosta, E. Bauch, M. P. Ledbetter, A. Waxman, L.-S. Bouchard, and D. Budker. Temperature dependence of the nitrogen-vacancy magnetic resonance in diamond. *Physical Review Letters*, 104(7), Feb 2010.

[14] C. B. Adams et al. Axion Dark Matter. In *Snowmass 2021*, 3 2022.

[15] N. Agafonova et al. Discovery potential for directional Dark Matter detection with nuclear emulsions. *Eur. Phys. J. C*, 78(7):578, 2018.

[16] R. Agnese et al. Demonstration of Surface Electron Rejection with Interleaved Germanium Detectors for Dark Matter Searches. *Appl. Phys. Lett.*, 103:164105, 2013.

[17] R. Agnese et al. Projected Sensitivity of the SuperCDMS SNOLAB experiment. *Phys. Rev. D*, 95(8):082002, 2017.

[18] A. Aguilar-Arevalo et al. Characterization of the background spectrum in DAMIC at SNOLAB. 10 2021.

[19] D. Akimov, J. B. Albert, P. An, C. Awe, P. S. Barbeau, B. Becker, V. Belov, I. Bernardi, M. A. Blackston, L. Blokland, and et al. First measurement of coherent elastic neutrino-nucleus scattering on argon. *Physical Review Letters*, 126(1), Jan 2021.

[20] D. Akimov, J. B. Albert, P. An, C. Awe, P. S. Barbeau, B. Becker, V. Belov, A. Brown, A. Bolozdynya, B. Cabrera-Palmer, and et al. Observation of coherent elastic neutrino-nucleus scattering. *Science*, 357(6356):1123–1126, Sep 2017.

[21] Mark S. Akselrod, R. Craig Yoder, and Gleb M. Akselrod. Confocal fluorescent imaging of tracks from heavy charged particles utilising new al2o3:c,mg crystals. *Radiation Protection Dosimetry*, 119(1–4):357–362, 2006.

[22] A. Aleksandrov et al. NEWS: Nuclear Emulsions for WIMP Search. 4 2016.

[23] D. Alesini et al. Search for invisible axion dark matter of mass $m_a = 43\ \mu$eV with the QUAX–$a\gamma$ experiment. *Phys. Rev. D*, 103(10):102004, 2021.

[24] Jim Alexander et al. The storage ring proton EDM experiment. 4 2022.

[25] W Brock Alexander, Paul H Holloway, Joseph Simmons, and Romulo Ochoa. Increased precision in strain measurement of diamond by microraman spectroscopy. *Journal of Vacuum Science & Technology A: Vacuum, Surfaces, and Films*, 12(5):2943–2945, 1994.

[26] A. Alexandrov, G. De Lellis, A. Di Crescenzo, A. Golovatiuk, and V. Tioukov. Directionality preservation of nuclear recoils in an emulsion detector for directional dark matter search. *Journal of Cosmology and Astroparticle Physics*, 2021(04):047, Apr 2021.

[27] Andrey Alexandrov, Takashi Asada, Giovanni De Lellis, Antonia Di Crescenzo, Valerio Gentile, Tatsuhiro Naka, Valeri Tioukov, and Atsuhiro Umemoto. Super-resolution high-speed optical microscopy for fully automated readout of metallic nanoparticles and nanostructures. *Sci. Rep.*, 10(1):18773, 2020.

[28] Pau Amaro Seoane et al. Laser Interferometer Space Antenna. *arXiv e-prints*, February 2017.

[29] Pau Amaro Seoane et al. The effect of mission duration on LISA science objectives. *General Relativity and Gravitation*, 54(1):3, January 2022.

[30] Pau Amaro Seoane et al. Astrophysics with the Laser Interferometer Space Antenna. *Living Rev. Rel.*, 26(1):2, 2023.

[31] M. Ambrosio et al. Final search for lightly ionizing particles with the MACRO detector. 2 2004.

[32] A. J. Anderson, J. M. Conrad, E. Figueroa-Feliciano, C. Ignarra, G. Karagiorgi, K. Scholberg, M. H. Shaevitz, and J. Spitz. Measuring active-to-sterile neutrino oscillations with neutral current coherent neutrino-nucleus scattering. *Phys. Rev. D*, 86:013004, Jul 2012.

[33] Guillem Anglada and Jordi Torra. Astrometric light-travel time signature of sources in nonlinear motion. 11 2005.

[34] B. Anguiano, A. Rebassa-Mansergas, E. García-Berro, S. Torres, K. C. Freeman, and T. Zwitter. The kinematics of the white dwarf population from the SDSS DR12. , 469(2):2102–2120, August 2017.

[35] Borja Anguiano, Steven R. Majewski, Christian R. Hayes, Carlos Allende Prieto, Xinlun Cheng, Christian Moni Bidin, Rachael L. Beaton, Timothy C. Beers, and Dante Minniti. The Stellar Velocity Distribution Function in the Milky Way Galaxy. , 160(1):43, July 2020.

[36] T Antoja, A Helmi, M Romero-Gómez, D Katz, C Babusiaux, Ronald Drimmel, DW Evans, F Figueras, Eloisa Poggio, C Reylé, et al. A dynamically young and perturbed milky way disk. *Nature*, 561(7723):360–362, 2018.

[37] D. Antonov, T. Häuβermann, A. Aird, J. Roth, H.-R. Trebin, C. Müller, L. McGuinness, F. Jelezko, T. Yamamoto, J. Isoya, S. Pezzagna, J. Meijer, and J. Wrachtrup. Statistical investigations on nitrogen-vacancy center creation. *Applied Physics Letters*, 104(1):012105, Jan 2014.

[38] E. Aprile, J. Aalbers, F. Agostini, S. Ahmed Maouloud, M. Alfonsi, L. Althueser, F. D. Amaro, S. Andaloro, V. C. Antochi, E. Angelino, and et al. Search for coherent elastic scattering of solar ^{8}b neutrinos in the xenon1t dark matter experiment. *Physical Review Letters*, 126(9), Mar 2021.

[39] E. Aprile, F. Agostini, M. Alfonsi, L. Arazi, K. Arisaka, F. Arneodo, M. Auger, C. Balan, P. Barrow, and et al. Lowering the radioactivity of the photomultiplier tubes for the xenon1t dark matter experiment. *The European Physical Journal C*, 75(11), Nov 2015.

[40] K. Arai, C. Belthangady, H. Zhang, N. Bar-Gill, S. J. DeVience, P. Cappellaro, A. Yacoby, and R. L. Walsworth. Fourier magnetic imaging with nanoscale resolution and compressed sensing speed-up using electronic spins in diamond. *Nature Nanotechnology*, 10(1010):859–864, Oct 2015.

[41] Paola Arias, Davide Cadamuro, Mark Goodsell, Joerg Jaeckel, Javier Redondo, and Andreas Ringwald. WISPy Cold Dark Matter. *JCAP*, 06:013, 2012.

[42] D. Aristizabal Sierra, V. De Romeri, L. J. Flores, and D. K. Papoulias. Impact of COHERENT measurements, cross section uncertainties and new interactions on the neutrino floor. *JCAP*, 01(01):055, 2022.

[43] M. Armano et al. Sub-Femto- g Free Fall for Space-Based Gravitational Wave Observatories: LISA Pathfinder Results. *Phys. Rev. Lett.*, 116(23):231101, 2016.

[44] Silvia Arroyo-Camejo, Marie-Pierre Adam, Mondher Besbes, Jean-Paul Hugonin, Vincent Jacques, Jean-Jacques Greffet, Jean-François Roch, Stefan W. Hell, and François Treussart. Stimulated emission depletion microscopy resolves individual nitrogen vacancy centers in diamond nanocrystals. *ACS Nano*, 7(12):10912–10919, Dec 2013.

[45] Asimina Arvanitaki, Amalia Madden, and Ken Van Tilburg. The Piezoaxionic Effect. 12 2021.

[46] Peter Athron et al. Global fits of GUT-scale SUSY models with GAMBIT. *Eur. Phys. J. C*, 77(12):824, 2017.

[47] Deniz Aybas et al. Search for Axionlike Dark Matter Using Solid-State Nuclear Magnetic Resonance. *Phys. Rev. Lett.*, 126(14):141802, 2021.

[48] Stanislav Babak, Martin Hewitson, and Antoine Petiteau. LISA Sensitivity and SNR Calculations. *arXiv e-prints*, page arXiv:2108.01167, August 2021.

[49] K. M. Backes et al. A quantum-enhanced search for dark matter axions. *Nature*, 590(7845):238–242, 2021.

[50] Howard Baer, Ki-Young Choi, Jihn E. Kim, and Leszek Roszkowski. Dark matter production in the early universe: Beyond the thermal wimp paradigm. *Physics Reports*, 555:1–60, 2015. Dark matter production in the early Universe: Beyond the thermal WIMP paradigm.

[51] K.G. Balasi, K. Langanke, and G. Martínez-Pinedo. Neutrino–nucleus reactions and their role for supernova dynamics and nucleosynthesis. *Progress in Particle and Nuclear Physics*, 85:33–81, Nov 2015.

[52] Gopalakrishnan Balasubramanian, IY Chan, Roman Kolesov, Mohannad Al-Hmoud, Julia Tisler, Chang Shin, Changdong Kim, Aleksander Wojcik, Philip R Hemmer, Anke Krueger, et al. Nanoscale imaging magnetometry with diamond spins under ambient conditions. *Nature*, 455(7213):648–651, 2008.

[53] Gopalakrishnan Balasubramanian, Philipp Neumann, Daniel Twitchen, Matthew Markham, Roman Kolesov, Norikazu Mizuochi, Junichi Isoya, Jocelyn Achard, Johannes Beck, Julia Tissler, et al. Ultralong spin coherence time in isotopically engineered diamond. *Nature materials*, 8(5):383–387, 2009.

[54] Guillermo Ballesteros, Javier Redondo, Andreas Ringwald, and Carlos Tamarit. Unifying inflation with the axion, dark matter, baryogenesis and the seesaw mechanism. *Phys. Rev. Lett.*, 118(7):071802, 2017.

[55] E. Baracchini et al. CYGNO: a gaseous TPC with optical readout for dark matter directional search. *JINST*, 15(07):C07036, 2020.

[56] A. Barfuss, M. Kasperczyk, J. Kölbl, and P. Maletinsky. Spin-stress and spin-strain coupling in diamond-based hybrid spin oscillator systems. *Physical Review B*, 99(17), May 2019.

[57] J. Barranco, O. G. Miranda, and T. I. Rashba. Sensitivity of low energy neutrino experiments to physics beyond the standard model. *Physical Review D*, 76(7), Oct 2007.

[58] John F. Barry, Jennifer M. Schloss, Erik Bauch, Matthew J. Turner, Connor A. Hart, Linh M. Pham, and Ronald L. Walsworth. Sensitivity optimization for NV-diamond magnetometry. *Reviews of Modern Physics*, 92(1):015004, March 2020.

[59] John F. Barry, Matthew J. Turner, Jennifer M. Schloss, David R. Glenn, Yuyu Song, Mikhail D. Lukin, Hongkun Park, and Ronald L. Walsworth. Optical magnetic detection of single-neuron action potentials using quantum defects in diamond. *Proceedings of the National Academy of Sciences*, 113(49):14133–14138, Nov 2016.

[60] C. Bartram et al. Search for Invisible Axion Dark Matter in the 3.3–4.2 μeV Mass Range. *Phys. Rev. Lett.*, 127(26):261803, 2021.

[61] J. A. Bartz, S. Kodaira, M. Kurano, N. Yasuda, and M. S. Akselrod. High resolution charge spectroscopy of heavy ions with fntd technology. *Nuclear Instruments and Methods in Physics Research Section B: Beam Interactions with Materials and Atoms*, 335:24–30, Sep 2014.

[62] J. B. R. Battat et al. Radon in the DRIFT-II directional dark matter TPC: emanation, detection and mitigation. *JINST*, 9(11):P11004, 2014.

[63] Sebastian Baum, Andrzej K. Drukier, Katherine Freese, Maciej Górski, and Patrick Stengel. Searching for Dark Matter with Paleo-Detectors. *Phys. Lett. B*, 803:135325, 2020.

[64] Sebastian Baum, Thomas D. P. Edwards, Bradley J. Kavanagh, Patrick Stengel, Andrzej K. Drukier, Katherine Freese, Maciej Górski, and Christoph Weniger. Paleodetectors for Galactic supernova neutrinos. *Phys. Rev. D*, 101(10):103017, 2020.

[65] JL Baxter, SA Wilde, RT Pidgeon, and IR Fletcher. The jack hills metasedimentary belt: an extension of the early archaean terrain in the yilgarn block, western australia. *Australian Geol. Conv., Macquarie University, North Ryde*, pages 56–57, 1984.

[66] P. Belli et al. Measurements of $ZnWO_4$ anisotropic response to nuclear recoils for the ADAMO project. *Eur. Phys. J. A*, 56(3):83, 2020.

[67] Matthew Benacquista and K. Holley-Bockelmann. Consequences of disk scale height on LISA confusion noise from close white dwarf binaries. *Astrophys. J.*, 645:589–596, 2006.

[68] Morgan Bennett and Jo Bovy. Vertical waves in the solar neighbourhood in Gaia DR2. *Mon. Not. R. Astron. Soc.*, 482:1417–1425, January 2019.

[69] Johannes Bergstrom, M. C. Gonzalez-Garcia, Michele Maltoni, Carlos Pena-Garay, Aldo M. Serenelli, and Ningqiang Song. Updated determination of the solar neutrino fluxes from solar neutrino data. *JHEP*, 03:132, 2016.

[70] Evan Berkowitz, Michael I. Buchoff, and Enrico Rinaldi. Lattice QCD input for axion cosmology. *Phys. Rev. D*, 92(3):034507, 2015.

[71] Asher Berlin, Raffaele Tito D'Agnolo, Sebastian A. R. Ellis, Christopher Nantista, Jeffrey Neilson, Philip Schuster, Sami Tantawi, Natalia Toro, and Kevin Zhou. Axion Dark Matter Detection by Superconducting Resonant Frequency Conversion. *JHEP*, 07(07):088, 2020.

[72] Asher Berlin and Kevin Zhou. Discovering QCD-Coupled Axion Dark Matter with Polarization Haloscopes. 9 2022.

[73] Marc Beutter, Andreas Pargner, Thomas Schwetz, and Elisa Todarello. Axion-electrodynamics: a quantum field calculation. *JCAP*, 02:026, 2019.

[74] Amit Bhoonah, Joseph Bramante, Sarah Schon, and Ningqiang Song. Detecting composite dark matter with long range and contact interactions in gas clouds. 10 2020.

[75] E Bielejec, J A Seamons, and M S Carroll. Single ion implantation for single donor devices using geiger mode detectors. *Nanotechnology*, 21(8):085201, jan 2010.

[76] J. Billard, E. Figueroa-Feliciano, and L. Strigari. Implication of neutrino backgrounds on the reach of next generation dark matter direct detection experiments. *Physical Review D*, 89(2), Jan 2014.

[77] James Binney. Dynamics for galactic archaeology. , 57(3-4):29–51, September 2013.

[78] Joss Bland-Hawthorn and Ortwin Gerhard. The Galaxy in Context: Structural, Kinematic, and Integrated Properties. , 54:529–596, September 2016.

[79] S. Bodenstedt, I. Jakobi, J. Michl, I. Gerhardt, P. Neumann, and J. Wrachtrup. Nanoscale spin manipulation with pulsed magnetic gradient fields from a hard disc drive writer. *Nano Letters*, 18(9):5389–5395, Sep 2018.

[80] Claudio Bonati, Massimo D'Elia, Marco Mariti, Guido Martinelli, Michele Mesiti, Francesco Negro, Francesco Sanfilippo, and Giovanni Villadoro. Axion phenomenology and θ-dependence from $N_f = 2+1$ lattice QCD. *JHEP*, 03:155, 2016.

[81] Camille Bonvin, Chiara Caprini, Riccardo Sturani, and Nicola Tamanini. Effect of matter structure on the gravitational waveform. *Phys. Rev. D*, 95(4):044029, 2017.

[82] Albert Boretti and Stefania Castelletto. Nanometric resolution magnetic resonance imaging methods for mapping functional activity in neuronal networks. *MethodsX*, 3:297–306, Jan 2016.

[83] Alberto Boretti, Lorenzo Rosa, Jonathan Blackledge, and Stefania Castelletto. Nitrogen-vacancy centers in diamond for nanoscale magnetic resonance imaging applications. *Beilstein Journal of Nanotechnology*, 10:2128–2151, Nov 2019.

[84] Sz. Borsanyi et al. Calculation of the axion mass based on high-temperature lattice quantum chromodynamics. *Nature*, 539(7627):69–71, 2016.

[85] Salvatore Bottaro, Dario Buttazzo, Marco Costa, Roberto Franceschini, Paolo Panci, Diego Redigolo, and Ludovico Vittorio. Closing the window on WIMP Dark Matter. *Eur. Phys. J. C*, 82(1):31, 2022.

[86] Adrien Bourgoin, Christophe Le Poncin-Lafitte, Stéphane Mathis, and Marie-Christine Angonin. Dipolar magnetic fields in binaries and gravitational waves. In *Semaine de l'astrophysique française 2021*, 9 2021.

[87] Jo Bovy. galpy: A python Library for Galactic Dynamics. , 216(2):29, February 2015.

[88] Jo Bovy and Hans-Walter Rix. A Direct Dynamical Measurement of the Milky Way's Disk Surface Density Profile, Disk Scale Length, and Dark Matter Profile at 4 kpc $\lesssim$ R $\lesssim$ 9 kpc. *Astrophys. J.*, 779:115, 2013.

[89] William R. Bower, Richard A.D. Pattrick, Carolyn I. Pearce, Giles T.R. Droop, and Sarah J. Haigh. Radiation damage haloes in biotite investigated using high-resolution transmission electron microscopy. *American Mineralogist*, 101(1):105 – 110, 01 Jan. 2016.

[90] James Bradbury, Roy Frostig, Peter Hawkins, Matthew James Johnson, Chris Leary, Dougal Maclaurin, George Necula, Adam Paszke, Jake VanderPlas, Skye Wanderman-Milne, and Qiao Zhang. JAX: composable transformations of Python+NumPy programs, 2018.

[91] V. B. Braginsky, M. L. Gorodetsky, and S. P. Vyatchanin. Thermodynamical fluctuations and photothermal shot noise in gravitational wave antennae. *Phys. Lett. A*, 264:1, 1999.

[92] V.B. Braginsky, M.L. Gorodetsky, and S.P. Vyatchanin. Thermo-refractive noise in gravitational wave antennae. *Physics Letters A*, 271(5-6):303–307, jul 2000.

[93] Katelyn Breivik, Kyle Kremer, Michael Bueno, Shane L. Larson, Scott Coughlin, and Vassiliki Kalogera. Characterizing Accreting Double White Dwarf Binaries with the Laser Interferometer Space Antenna and Gaia. *Astrophys. J. Lett.*, 854(1):L1, 2018.

[94] Katelyn Breivik, Chiara M. F. Mingarelli, and Shane L. Larson. Constraining Galactic Structure with the LISA White Dwarf Foreground. *Astrophys. J.*, 901(1):4, 2020.

[95] D. A. Broadway, B. C. Johnson, M. S. J. Barson, S. E. Lillie, N. Dontschuk, D. J. McCloskey, A. Tsai, T. Teraji, D. A. Simpson, A. Stacey, J. C. McCallum, J. E. Bradby, M. W. Doherty, L. C. L. Hollenberg, and J.-P. Tetienne. Microscopic imaging of the stress tensor in diamond using in situ quantum sensors. *Nano Letters*, 19(7):4543–4550, May 2019.

[96] A. Broniatowski, X. Defay, E. Armengaud, L. Bergé, A. Benoit, O. Besida, J. Blümer, A. Chantelauze, M. Chapellier, G. Chardin, and et al. A new high-background-rejection dark matter ge cryogenic detector. *Physics Letters B*, 681(4):305–309, Nov 2009.

[97] L. Brouwer et al. Projected sensitivity of DMRadio-m3: A search for the QCD axion below 1 μeV. *Phys. Rev. D*, 106(10):103008, 2022.

[98] Phil Buckley, Natasha Hargreaves, and Sharon Cooper. Nucleation of quartz under ambient conditions. *Communications Chemistry*, 1(1):1–10, 2018.

[99] Dmitry Budker, Peter W. Graham, Micah Ledbetter, Surjeet Rajendran, and Alex Sushkov. Proposal for a Cosmic Axion Spin Precession Experiment (CASPEr). *Phys. Rev. X*, 4(2):021030, 2014.

[100] James S. Bullock and Michael Boylan-Kolchin. Small-Scale Challenges to the ΛCDM Paradigm. *Ann. Rev. Astron. Astrophys.*, 55:343–387, 2017.

[101] Malte Buschmann, Joshua W. Foster, Anson Hook, Adam Peterson, Don E. Willcox, Weiqun Zhang, and Benjamin R. Safdi. Dark matter from axion strings with adaptive mesh refinement. *Nature Commun.*, 13(1):1049, 2022.

[102] Malte Buschmann, Joshua W. Foster, and Benjamin R. Safdi. Early-Universe Simulations of the Cosmological Axion. *Phys. Rev. Lett.*, 124(16):161103, 2020.

[103] Malte Buschmann, Benjamin R. Safdi, and Katelin Schutz. Galactic Potential and Dark Matter Density from Angular Stellar Accelerations. *Phys. Rev. Lett.*, 127(24):241104, 2021.

[104] Craig Cahillane and Georgia Mansell. Review of the Advanced LIGO Gravitational Wave Observatories Leading to Observing Run Four. *Galaxies*, 10(1):36, 2022.

[105] Craig Cahillane, Georgia Mansell, and Daniel Sigg. Laser frequency noise in next generation gravitational-wave detectors. *Opt. Express*, 29(25):42144–42161, 2021.

[106] Craig Russell Cahillane. *Controlling and calibrating interferometric gravitational wave detectors*. PhD thesis, California Institute of Technology, 2021.

[107] Allen Caldwell, Gia Dvali, Béla Majorovits, Alexander Millar, Georg Raffelt, Javier Redondo, Olaf Reimann, Frank Simon, and Frank Steffen. Dielectric Haloscopes: A New Way to Detect Axion Dark Matter. *Phys. Rev. Lett.*, 118(9):091801, 2017.

[108] L. Canonica, A. H. Abdelhameed, P. Bauer, A. Bento, E. Bertoldo, N. Ferreiro Iachellini, D. Fuchs, D. Hauf, M. Mancuso, F. Petricca, F. Pröbst, and J. Rothe. Operation of a Diamond Cryogenic Detector for Low-Mass Dark Matter Searches. *J. Low Temp. Phys.*, 199(3-4):606–613, 2020.

[109] H. Cao et al. Measurement of Scintillation and Ionization Yield and Scintillation Pulse Shape from Nuclear Recoils in Liquid Argon. *Phys. Rev. D*, 91:092007, 2015.

[110] F. Cappella et al. On the potentiality of the $ZnWO_4$ anisotropic detectors to measure the directionality of Dark Matter. *Eur. Phys. J. C*, 73(1):2276, 2013.

[111] Andrea Caputo, Alexander J. Millar, Ciaran A. J. O'Hare, and Edoardo Vitagliano. Dark photon limits: A handbook. *Phys. Rev. D*, 104(9):095029, 2021.

[112] Andrea Caputo, Laura Sberna, Alexandre Toubiana, Stanislav Babak, Enrico Barausse, Sylvain Marsat, and Paolo Pani. Gravitational-wave detection and parameter estimation for accreting black-hole binaries and their electromagnetic counterpart. *Astrophys. J.*, 892(2):90, 2020.

[113] V. Caracciolo et al. The ADAMO Project and developments. *J. Phys. Conf. Ser.*, 718(4):042011, 2016.

[114] Jeffrey L. Carlin, James DeLaunay, Heidi Jo Newberg, Licai Deng, Daniel Gole, Kathleen Grabowski, Ge Jin, Chao Liu, Xiaowei Liu, A.-Li Luo, et al. SUBSTRUCTURE IN BULK VELOCITIES OF MILKY WAY DISK STARS. *Astrophys. J. Lett.*, 777(1):L5, October 2013.

[115] I. Carrillo, I. Minchev, G. Kordopatis, M. Steinmetz, J. Binney, F. Anders, O. Bienaymé, J. Bland-Hawthorn, B. Famaey, K. C. Freeman, et al. Is the Milky Way still breathing? RAVE–Gaia streaming motions. *Mon. Not. R. Astron. Soc.*, 475(2):2679–2696, April 2018.

[116] G. A. Carvalho, R. C. dos Anjos, J. G. Coelho, R. V. Lobato, M. Malheiro, R. M. Marinho, J. F. Rodriguez, J. A. Rueda, and R. Ruffini. Orbital Decay of Double White Dwarfs: Beyond Gravitational-wave Radiation Effects. *Astrophys. J.*, 940(1):90, 2022.

[117] Carlton M. Caves. Quantum-mechanical noise in an interferometer. *Phys. Rev. D*, 23:1693–1708, Apr 1981.

[118] Aaron J Cavosie, Simon A Wilde, Dunyi Liu, Paul W Weiblen, and John W Valley. Internal zoning and u–th–pb chemistry of jack hills detrital zircons: a mineral record of early archean to mesoproterozoic (4348–1576 ma) magmatism. *Precambrian Research*, 135(4):251–279, 2004.

[119] Raphael Cervantes, Caterina Braggio, Bianca Giaccone, Daniil Frolov, Anna Grassellino, Roni Harnik, Oleksandr Melnychuk, Roman Pilipenko, Sam Posen, and Alexander Romanenko. Deepest Sensitivity to Wavelike Dark Photon Dark Matter with SRF Cavities. 8 2022.

[120] Sukanya Chakrabarti, Philip Chang, Michael T. Lam, Sarah J. Vigeland, and Alice C. Quillen. A Measurement of the Galactic Plane Mass Density from Binary Pulsar Accelerations. , 907(2):L26, February 2021.

[121] Sukanya Chakrabarti, Daniel J. Stevens, Jason Wright, Roman R. Rafikov, Philip Chang, Thomas Beatty, and Daniel Huber. Eclipse Timing the Milky Way's Gravitational Potential. , 928(2):L17, April 2022.

[122] Srivatsa Chakravarthi, Chris Moore, April Opsvig, Christian Pederson, Emma Hunt, Andrew Ivanov, Ian Christen, Scott Dunham, and Kai-Mei C. Fu. Window into nv center kinetics via repeated annealing and spatial tracking of thousands of individual nv centers. *Phys. Rev. Materials*, 4:023402, Feb 2020.

[123] Hsin Chang et al. First Results from the Taiwan Axion Search Experiment with a Haloscope at 19.6 μeV. *Phys. Rev. Lett.*, 129(11):111802, 2022.

[124] Seung Pyo Chang, Selcuk Haciomeroglu, On Kim, Soohyung Lee, Seongtae Park, and Yannis K. Semertzidis. Axionlike dark matter search using the storage ring EDM method. *Phys. Rev. D*, 99(8):083002, 2019.

[125] F. Chasles, B. Dubertret, and A. C. Boccara. Full-field optical sectioning and three-dimensional localization of fluorescent particles using focal plane modulation. *Opt. Lett.*, 31(9):1274–1276, May 2006.

[126] Chuan-Ren Chen, Ming-Che Lee, and Ho-Chin Tsai. Implications of the little higgs dark matter and t-odd fermions. *Journal of High Energy Physics*, 2014(6):1–16, 2014.

[127] Edward H. Chen, Ophir Gaathon, Matthew E. Trusheim, and Dirk Englund. Wide-field multispectral super-resolution imaging using spin-dependent fluorescence in nanodiamonds. *Nano Letters*, 13(5):2073–2077, May 2013.

[128] Liangchao Chen, Xinyuan Miao, Hongan Ma, Longsuo Guo, Zhanke Wang, Zhiqiang Yang, Chao Fang, and XiaoPeng Jia. Synthesis and characterization of diamonds with different nitrogen concentrations under high pressure and high temperature conditions. *CrystEngComm*, 20(44):7164–7169, Nov 2018.

[129] Xian Chen, Ze-Yuan Xuan, and Peng Peng. Fake massive black holes in the milli-Hertz gravitational-wave band. *Astrophys. J.*, 896(2):171, 2020.

[130] Xiang-Dong Chen, Deng-Feng Li, Yu Zheng, Shen Li, Bo Du, Yang Dong, Chun-Hua Dong, Guang-Can Guo, and Fang-Wen Sun. Superresolution multifunctional sensing with the nitrogen-vacancy center in diamond. *Physical Review Applied*, 12(4):044039, Oct 2019.

[131] Xiangdong Chen, Changling Zou, Zhaojun Gong, Chunhua Dong, Guangcan Guo, and Fangwen Sun. Subdiffraction optical manipulation of the charge state of nitrogen vacancy center in diamond. *Light: Science & Applications*, 4(11):e230–e230, Jan 2015.

[132] L. Childress, J. M. Taylor, A. S. Sørensen, and M. D. Lukin. Fault-tolerant quantum communication based on solid-state photon emitters. *Physical Review Letters*, 96(7), Feb 2006.

[133] Lilian Childress and Ronald Hanson. Diamond nv centers for quantum computing and quantum networks. *MRS Bulletin*, 38(2):134–138, 2013.

[134] J.I. Collar and III Avignone, F.T. Nuclear tracks from cold dark matter interactions in mineral crystals: A Computational study. *Nucl. Instrum. Meth. B*, 95:349, 1995.

[135] Jeffrey D. Crane, Steven R. Majewski, Helio J. Rocha-Pinto, Peter M. Frinchaboy, Michael F. Skrutskie, and David R. Law. Exploring halo substructure with giant stars: Spectroscopy of stars in the Galactic anti-center stellar structure. *Astrophys. J. Lett.*, 594:L119–L122, 2003.

[136] Alexandre Crisci, Francis Baillet, Michel Mermoux, Ganna Bogdan, Milos Nesládek, and Ken Haenen. Residual strain around grown-in defects in cvd diamond single crystals: A 2d and 3d raman imaging study. *physica status solidi (a)*, 208(9):2038–2044, 2011.

[137] N. Crisosto, P. Sikivie, N. S. Sullivan, D. B. Tanner, J. Yang, and G. Rybka. ADMX SLIC: Results from a Superconducting *LC* Circuit Investigating Cold Axions. *Phys. Rev. Lett.*, 124(24):241101, 2020.

[138] Gavin Dalton et al. Project overview and update on WEAVE: the next generation wide-field spectroscopy facility for the William Herschel Telescope. In Suzanne K. Ramsay, Ian S. McLean, and Hideki Takami, editors, *Ground-based and Airborne Instrumentation for Astronomy V*, volume 9147 of *Society of Photo-Optical Instrumentation Engineers (SPIE) Conference Series*, page 91470L, July 2014.

[139] F.A. Danevich, V.V. Kobychev, S.S. Nagorny, D.V. Poda, V.I. Tretyak, S.S. Yurchenko, and Yu.G. Zdesenko. $ZnWO_4$ crystals as detectors for 2β decay and dark matter experiments. *Nucl. Instrum. Meth. A*, 544(3):553–564, 2005.

[140] Jonathan H. Davis. Dark matter vs. neutrinos: the effect of astrophysical uncertainties and timing information on the neutrino floor. *Journal of Cosmology and Astroparticle Physics*, 2015(03):012–012, Mar 2015.

[141] R. S. de Jong et al. 4MOST: Project overview and information for the First Call for Proposals. *The Messenger*, 175:3–11, March 2019.

[142] AM De Riva, G Zavattini, S Marigo, C Rizzo, G Ruoso, G Carugno, R Onofrio, S Carusotto, M Papa, F Perrone, et al. Very high q frequency-locked fabry–perot cavity. *Review of scientific instruments*, 67(8):2680–2684, 1996.

[143] Peter Deák, Bálint Aradi, Moloud Kaviani, Thomas Frauenheim, and Adam Gali. Formation of nv centers in diamond: A theoretical study based on calculated transitions and migration of nitrogen and vacancy related defects. *Physical Review B*, 89(7):075203, Feb 2014.

[144] C. L. Degen. Scanning magnetic field microscope with a diamond single-spin sensor. *Applied Physics Letters*, 92(24):243111, Jun 2008.

[145] Federico Della Valle, Aldo Ejlli, Ugo Gastaldi, Giuseppe Messineo, Edoardo Milotti, Ruggero Pengo, Giuseppe Ruoso, and Guido Zavattini. The pvlas experiment: measuring vacuum magnetic birefringence and dichroism with a birefringent fabry–perot cavity. *The European Physical Journal C*, 76:1–15, 2016.

[146] Federico Della Valle, Edoardo Milotti, A Ejlli, U Gastaldi, G Messineo, L Piemontese, G Zavattini, R Pengo, and G Ruoso. Extremely long decay time optical cavity. *Optics Express*, 22(10):11570–11577, 2014.

[147] Patrick deNiverville, Maxim Pospelov, and Adam Ritz. Light new physics in coherent neutrino-nucleus scattering experiments. *Physical Review D*, 92(9), Nov 2015.

[148] William DeRocco, Peter W. Graham, and Surjeet Rajendran. Exploring the robustness of stellar cooling constraints on light particles. *Phys. Rev. D*, 102(7):075015, 2020.

[149] William DeRocco and Anson Hook. Axion interferometry. *Phys. Rev. D*, 98(3):035021, 2018.

[150] Michael Dine, Patrick Draper, Laurel Stephenson-Haskins, and Di Xu. Axions, Instantons, and the Lattice. *Phys. Rev. D*, 96(9):095001, 2017.

[151] Michael Dine and Willy Fischler. The Not So Harmless Axion. *Phys. Lett. B*, 120:137–141, 1983.

[152] A. C. Dodd, E. Papageorgiu, and S. Ranfone. The Effect of a neutrino magnetic moment on nuclear excitation processes. *Phys. Lett. B*, 266:434–438, 1991.

[153] Marcus W. Doherty, Neil B. Manson, Paul Delaney, Fedor Jelezko, Jörg Wrachtrup, and Lloyd C.L. Hollenberg. The nitrogen-vacancy colour centre in diamond. *Physics Reports*, 528(1):1–45, 2013.

[154] Elena D'Onghia and J. Alfonso L. Aguerri. Trojans in the Solar Neighborhood. , 890(2):117, February 2020.

[155] Andrzej K. Drukier et al. Paleo-detectors: Searching for dark matter with ancient minerals. *Phys. Rev. D*, 99(4):043014, 2019.

[156] Bhaskar Dutta, Yu Gao, Andrew Kubik, Rupak Mahapatra, Nader Mirabolfathi, Louis E. Strigari, and Joel W. Walker. Sensitivity to oscillation with a sterile fourth generation neutrino from ultralow threshold neutrino-nucleus coherent scattering. *Phys. Rev. D*, 94:093002, Nov 2016.

[157] Bhaskar Dutta, Rupak Mahapatra, Louis E. Strigari, and Joel W. Walker. Sensitivity to z-prime and nonstandard neutrino interactions from ultralow threshold neutrino-nucleus coherent scattering. *Physical Review D*, 93(1), Jan 2016.

[158] Cora Dvorkin, Kfir Blum, and Marc Kamionkowski. Constraining Dark Matter-Baryon Scattering with Linear Cosmology. *Phys. Rev. D*, 89(2):023519, 2014.

[159] Sheila Dwyer and Stefan W. Ballmer. Radiative Thermal Noise for Transmissive Optics in Gravitational-Wave Detectors. *Phys. Rev. D*, 90(4):043013, 2014.

[160] Martin J. Dyer et al. The Gravitational-wave Optical Transient Observer (GOTO). *Proc. SPIE Int. Soc. Opt. Eng.*, 11445:114457G, 2020.

[161] Reza Ebadi et al. Ultraheavy dark matter search with electron microscopy of geological quartz. *Phys. Rev. D*, 104(1):015041, 2021.

[162] Reza Ebadi et al. Directional Detection of Dark Matter Using Solid-State Quantum Sensing. In *Snowmass 2021*, 3 2022.

[163] Reza Ebadi, David E. Kaplan, Surjeet Rajendran, and Ronald L. Walsworth. GALILEO: Galactic Axion Laser Interferometer Leveraging Electro-Optics. *Phys. Rev. Lett.*, 132(10):101001, 2024.

[164] Reza Ebadi, Vladimir Strokov, Erwin H. Tanin, Emanuele Berti, and Ronald L. Walsworth. LISA double white dwarf binaries as Galactic accelerometers. *Phys. Rev. D*, 111(4):044023, 2025.

[165] Philippe H. Eberhard, Ronald R. Ross, Luis W. Alvarez, and Robert D. Watt. Search for magnetic monopoles in lunar material. *Phys. Rev. D*, 4:3260–3272, Dec 1971.

[166] Andrew M. Edmonds, Connor A. Hart, Matthew J. Turner, Pierre-Olivier Colard, Jennifer M. Schloss, Kevin Olsson, Raisa Trubko, Matthew L. Markham, Adam Rathmill, Ben Horne-Smith, Wilbur Lew, Arul Manickam, Scott Bruce, Peter G. Kaup, Jon C. Russo, Michael J. DiMario, Joseph T. South, Jay T. Hansen, Daniel J. Twitchen, and Ronald L. Walsworth. Generation of nitrogen-vacancy ensembles in diamond for quantum sensors: Optimization and scalability of cvd processes. 2020.

[167] Russell T. Edwards, G. B. Hobbs, and R. N. Manchester. Tempo2, a new pulsar timing package. 2. The timing model and precision estimates. *Mon. Not. Roy. Astron. Soc.*, 372:1549–1574, 2006.

[168] Thomas D.P. Edwards et al. Digging for dark matter: Spectral analysis and discovery potential of paleo-detectors. *Phys. Rev. D*, 99(4):043541, 2019.

[169] A Ejlli, F Della Valle, U Gastaldi, G Messineo, R Pengo, G Ruoso, and G Zavattini. The pvlas experiment: A 25 year effort to measure vacuum magnetic birefringence. *Physics Reports*, 871:1–74, 2020.

[170] Felix Eltes, Christian Mai, Daniele Caimi, Marcel Kroh, Youri Popoff, Georg Winzer, Despoina Petousi, Stefan Lischke, J Elliott Ortmann, Lukas Czornomaz, et al. A batio 3-based electro-optic pockels modulator monolithically integrated on an advanced silicon photonics platform. *Journal of Lightwave Technology*, 37(5):1456–1462, 2019.

[171] J. Engel, M. T. Ressell, I. S. Towner, and W. E. Ormand. Response of mica to weakly interacting massive particles. *Phys. Rev. C*, 52:2216–2221, Oct 1995.

[172] JD Eshelby. Distortion of a crystal by point imperfections. *Journal of Applied Physics*, 25(2):255–261, 1954.

[173] M. Evans, S. Ballmer, M. Fejer, P. Fritschel, G. Harry, and G. Ogin. Thermo-optic noise in coated mirrors for high-precision optical measurements. *Phys. Rev. D*, 78:102003, 2008.

[174] Marco Fabbrichesi, Emidio Gabrielli, and Gaia Lanfranchi. The Dark Photon. 5 2020.

[175] D. Farfurnik, N. Alfasi, S. Masis, Y. Kauffmann, E. Farchi, Y. Romach, Y. Hovav, E. Buks, and N. Bar-Gill. Enhanced concentrations of nitrogen-vacancy centers in diamond through tem irradiation. *Applied Physics Letters*, 111(12):123101, Sep 2017.

[176] Michael A. Fedderke, Jedidiah O. Thompson, Raphael Cervantes, Bianca Giaccone, Roni Harnik, David E. Kaplan, Sam Posen, and Surjeet Rajendran. MAGPI: Measurement of Axion Gradients with Photon Interferometry. 4 2023.

[177] Maxwell Finan-Jenkin and Richard Easther. Inside MOND: Testing Gravity with Stellar Accelerations. 6 2023.

[178] Eliot Finch, Giorgia Bartolucci, Daniel Chucherko, Ben G. Patterson, Valeriya Korol, Antoine Klein, Diganta Bandopadhyay, Hannah Middleton, Christopher J. Moore, and Alberto Vecchio. Identifying LISA verification binaries among the Galactic population of double white dwarfs. *Mon. Not. Roy. Astron. Soc.*, 522(4):5358–5373, 2023.

[179] R. L. Fleischer, H. R. Hart, I. S. Jacobs, P. B. Price, W. M. Schwarz, and F. Aumento. Search for magnetic monopoles in deep ocean deposits. *Phys. Rev.*, 184:1393–1397, Aug 1969.

[180] R. L. Fleischer, I. S. Jacobs, W. M. Schwarz, P. B. Price, and H. G. Goodell. Search for multiply charged dirac magnetic poles. *Phys. Rev.*, 177:2029–2035, Jan 1969.

[181] R L Fleischer, P B Price, and R M Walker. Solid-state track detectors: Applications to nuclear science and geophysics. *Annual Review of Nuclear Science*, 15(1):1–28, 1965.

[182] R. L. Fleischer, P. B. Price, and R. M. Walker. Tracks of charged particles in solids. *Science*, 149(3682):383–393, 1965.

[183] R. L. Fleischer, P. B. Price, R. M. Walker, and E. L. Hubbard. Track registration in various solid-state nuclear track detectors. *Phys. Rev.*, 133:A1443–A1449, Mar 1964.

[184] R. L. Fleischer, P. B. Price, and R. T. Woods. Search for tracks of massive, multiply charged magnetic poles. *Phys. Rev.*, 184:1398–1401, Aug 1969.

[185] V. Fomenko, B. Moreno, M. Million, J. Harrison, and M. Akselrod. Energy response of fluorescent nuclear track detectors of various colorations to monoenergetic neutrons. *Radiation Protection Dosimetry*, 180(1–4):215–219, Aug 2018.

[186] Joshua W. Foster, Yonatan Kahn, Rachel Nguyen, Nicholas L. Rodd, and Benjamin R. Safdi. Dark Matter Interferometry. *Phys. Rev. D*, 103(7):076018, 2021.

[187] D Z Freedman, D N Schramm, and D L Tubbs. The weak neutral current and its effects in stellar collapse. *Annual Review of Nuclear Science*, 27(1):167–207, 1977.

[188] Daniel Z. Freedman. Coherent effects of a weak neutral current. *Phys. Rev. D*, 9:1389–1392, Mar 1974.

[189] I. Friel, S.L. Clewes, H.K. Dhillon, N. Perkins, D.J. Twitchen, and G.A. Scarsbrook. Control of surface and bulk crystalline quality in single crystal diamond grown by chemical vapour deposition. *Diamond and Related Materials*, 18(5):808–815,

2009. Proceedings of Diamond 2008, the 19th European Conference on Diamond, Diamond-Like Materials, Carbon Nanotubes, Nitrides and Silicon Carbide.

[190] Susan Gardner, Samuel D. McDermott, and Brian Yanny. The milky way, coming into focus: Precision astrometry probes its evolution and its dark matter. *Progress in Particle and Nuclear Physics*, 121:103904, Nov 2021.

[191] Andrea Gaspert, Pietro Giampa, and David E. Morrissey. Neutrino backgrounds in future liquid noble element dark matter direct detection experiments. *Phys. Rev. D*, 105(3):035020, 2022.

[192] M.P. Gaukroger, P.M. Martineau, M.J. Crowder, I. Friel, S.D. Williams, and D.J. Twitchen. X-ray topography studies of dislocations in single crystal cvd diamond. *Diamond and Related Materials*, 17(3):262–269, 2008.

[193] Graciela B. Gelmini, Volodymyr Takhistov, and Samuel J. Witte. Casting a Wide Signal Net with Future Direct Dark Matter Detection Experiments. *JCAP*, 07:009, 2018. [Erratum: JCAP 02, E02 (2019)].

[194] Maria Georgousi, Nikolaos Karnesis, Valeriya Korol, Mauro Pieroni, and Nikolaos Stergioulas. Gravitational waves from double white dwarfs as probes of the milky way. *Mon. Not. Roy. Astron. Soc.*, 519(2):2552–2566, 2022.

[195] A Ghiorso, SG Thompson, GH Higgins, GT Seaborg, MH Studier, PR Fields, SM Fried, H Diamond, JF Mech, GL Pyle, et al. New elements einsteinium and fermium, atomic numbers 99 and 100. *Physical Review*, 99(3):1048, 1955.

[196] A. Gianninas, Mukremin Kilic, Warren R. Brown, Paul Canton, and Scott J. Kenyon. The ELM Survey. VI. Eleven New Double Degenerates. , 812(2):167, October 2015.

[197] Artem Golovatiuk, Andrey Ustyuzhanin, Andrey Alexandrov, and Giovanni De Lellis. Deep Learning for direct Dark Matter search with nuclear emulsions. *Comput. Phys. Commun.*, 275:108312, 2022.

[198] Facundo A Gómez, Ivan Minchev, Brian W O'Shea, Timothy C Beers, James S Bullock, and Chris W Purcell. Vertical density waves in the milky way disc induced by the sagittarius dwarf galaxy. *Monthly Notices of the Royal Astronomical Society*, 429(1):159–164, 2013.

[199] Facundo A Gómez, Ivan Minchev, Brian W O'Shea, Young Sun Lee, Timothy C Beers, Deokkeun An, James S Bullock, Chris W Purcell, and Álvaro Villalobos. Signatures of minor mergers in the milky way disc–i. the segue stellar sample. *Monthly Notices of the Royal Astronomical Society*, 423(4):3727–3739, 2012.

[200] L. Gabriel Gómez and J. A. Rueda. Dark matter dynamical friction versus gravitational wave emission in the evolution of compact-star binaries. , 96(6):063001, September 2017.

[201] SA Gorbunov and NS Konovalova. New experiment newsdm for direct searches for heavy dark matter particles. *Physics of Atomic Nuclei*, 83(1):83–91, 2020.

[202] Jens Götze. Application of cathodoluminescence microscopy and spectroscopy in geosciences. *Microscopy and Microanalysis*, 18(6):1270–1284, 2012.

[203] Dorota M. Grabowska, Tom Melia, and Surjeet Rajendran. Detecting Dark Blobs. *Phys. Rev. D*, 98(11):115020, 2018.

[204] Peter W. Graham and Surjeet Rajendran. Axion Dark Matter Detection with Cold Molecules. *Phys. Rev. D*, 84:055013, 2011.

[205] Alexander V. Gramolin, Deniz Aybas, Dorian Johnson, Janos Adam, and Alexander O. Sushkov. Search for axion-like dark matter with ferromagnets. *Nature Phys.*, 17(1):79–84, 2021.

[206] GRAVITY Collaboration, R. Abuter, et al. Detection of the gravitational redshift in the orbit of the star S2 near the Galactic centre massive black hole. , 615:L15, July 2018.

[207] Daniel Green and Surjeet Rajendran. The Cosmology of Sub-MeV Dark Matter. *JHEP*, 10:013, 2017.

[208] Moira I. Gresham, Hou Keong Lou, and Kathryn M. Zurek. Early Universe synthesis of asymmetric dark matter nuggets. *Phys. Rev. D*, 97(3):036003, 2018.

[209] C. Grezes, B. Julsgaard, Y. Kubo, W. L. Ma, M. Stern, A. Bienfait, K. Nakamura, J. Isoya, S. Onoda, T. Ohshima, V. Jacques, D. Vion, D. Esteve, R. B. Liu, K. Mølmer, and P. Bertet. Storage and retrieval of microwave fields at the single-photon level in a spin ensemble. *Physical Review A*, 92(2), Aug 2015.

[210] Sinéad M. Griffin, Yonit Hochberg, Katherine Inzani, Noah Kurinsky, Tongyan Lin, and To Chin. Silicon carbide detectors for sub-GeV dark matter. *Phys. Rev. D*, 103(7):075002, 2021.

[211] Philipp Grothaus, Malcolm Fairbairn, and Jocelyn Monroe. Directional dark matter detection beyond the neutrino bound. *Physical Review D*, 90(5), Sep 2014.

[212] Shi-Lun Guo, Bao-Liu Chen, and S.A. Durrani. *Chapter 4 - Solid-State Nuclear Track Detectors*. Academic Press, Amsterdam, third edition edition, 2012.

[213] A. Gütlein, C. Ciemniak, F. von Feilitzsch, N. Haag, M. Hofmann, C. Isaila, T. Lachenmaier, J.-C. Lanfranchi, L. Oberauer, and S. Pfister. Solar and atmospheric neutrinos: Background sources for the direct dark matter searches. *Astroparticle Physics*, 34(2):90–96, Sep 2010.

[214] MF Hamers, GM Pennock, and MR Drury. Scanning electron microscope cathodoluminescence imaging of subgrain boundaries, twins and planar deformation features in quartz. *Physics and Chemistry of Minerals*, 44(4):263–275, 2017.

[215] Kyu Young Han, Katrin I. Willig, Eva Rittweger, Fedor Jelezko, Christian Eggeling, and Stefan W. Hell. Three-dimensional stimulated emission depletion microscopy of nitrogen-vacancy centers in diamond using continuous-wave light. *Nano Letters*, 9(9):3323–3329, Sep 2009.

[216] Ariful Haque and Sharaf Sumaiya. An overview on the formation and processing of nitrogen-vacancy photonic centers in diamond by ion implantation. *Journal of Manufacturing and Materials Processing*, 1(11):6, Sep 2017.

[217] Edward Hardy, Robert Lasenby, John March-Russell, and Stephen M. West. Big Bang Synthesis of Nuclear Dark Matter. *JHEP*, 06:011, 2015.

[218] F. J. Hasert et al. Observation of Neutrino Like Interactions Without Muon Or Electron in the Gargamelle Neutrino Experiment. *Phys. Lett. B*, 46:138–140, 1973.

[219] K. Heflin and R. Lieu. Galactic orbital effects on pulsar timing. , 504(1):166–171, June 2021.

[220] Lars Hernquist. An Analytical Model for Spherical Galaxies and Bulges. , 356:359, June 1990.

[221] Marie-Laure Hicks, Alexander C. Pakpour-Tabrizi, and Richard B. Jackman. Diamond etching beyond 10 μm with near-zero micromasking. *Scientific Reports*, 9(11):15619, Oct 2019.

[222] M.O. Hill, I. Calvo-Almazan, M. Allain, M.V. Holt, A. Ulvestad, J. Treu, G. Koblmüller, C. Huang, X. Huang, H. Yan, E. Nazaretski, Y.S. Chu, G.B. Stephenson, V. Chamard, L.J. Lauhon, and S.O. Hruszkewycz. Measuring three-dimensional strain and structural defects in a single ingaas nanowire using coherent x-ray multi-angle bragg projection ptychography. *Nano Letters*, 18(2):811–819, Feb 2018.

[223] Junji Hisano, Koji Ishiwata, Natsumi Nagata, and Tomohiro Takesako. Direct Detection of Electroweak-Interacting Dark Matter. *JHEP*, 07:005, 2011.

[224] Le Thi Mai Hoa, T Ouisse, D Chaussende, M Naamoun, A Tallaire, and J Achard. Birefringence microscopy of unit dislocations in diamond. *Crystal growth & design*, 14(11):5761–5766, 2014.

[225] M. A. Hollands, P. E. Tremblay, B. T. Gänsicke, N. P. Gentile-Fusillo, and S. Toonen. The Gaia 20 pc white dwarf sample. , 480(3):3942–3961, November 2018.

[226] Jennifer L Holmes, Kent N Bachus, and Roy D Bloebaum. Thermal effects of the electron beam and implications of surface damage in the analysis of bone tissue. *Scanning*, 22(4):243–248, 2000.

[227] Martin Holt, Ross Harder, Robert Winarski, and Volker Rose. Nanoscale hard x-ray microscopy methods for materials studies. *Annual Review of Materials Research*, 43(1):183–211, 2013.

[228] Anson Hook. TASI Lectures on the Strong CP Problem and Axions. *PoS*, TASI2018:004, 2019.

[229] Dan Hooper and Stefano Profumo. Dark Matter and Collider Phenomenology of Universal Extra Dimensions. *Phys. Rept.*, 453:29–115, 2007.

[230] C. J. Horowitz, K. J. Coakley, and D. N. McKinsey. Supernova observation via neutrino-nucleus elastic scattering in the clean detector. *Phys. Rev. D*, 68:023005, Jul 2003.

[231] Andrew Horsley, Patrick Appel, Janik Wolters, Jocelyn Achard, Alexandre Tallaire, Patrick Maletinsky, and Philipp Treutlein. Microwave device characterization using a widefield diamond microscope. *Phys. Rev. Applied*, 10:044039, Oct 2018.

[232] S. O. Hruszkewycz, M. Allain, M. V. Holt, C. E. Murray, J. R. Holt, P. H. Fuoss, and V. Chamard. High-resolution three-dimensional structural microscopy by single-angle bragg ptychography. *Nature Materials*, 16(22):244–251, Feb 2017.

[233] Kohei Inayoshi, Nicola Tamanini, Chiara Caprini, and Zoltán Haiman. Probing stellar binary black hole formation in galactic nuclei via the imprint of their center of mass acceleration on their gravitational wave signal. *Phys. Rev. D*, 96(6):063014, 2017.

[234] John B. Irwin. The Determination of a Light-Time Orbit. , 116:211, July 1952.

[235] John B. Irwin. Standard light-time curves. , 64:149, May 1959.

[236] Jan Isberg, Johan Hammersberg, Erik Johansson, Tobias Wikstrom, Daniel J. Twitchen, Andrew J. Whitehead, Steven E. Coe, and Geoffrey A. Scarsbrook. High Carrier Mobility in Single-Crystal Plasma-Deposited Diamond. *Science*, 297:1670–1673, 2002.

[237] David M. Jacobs, Glenn D. Starkman, and Bryan W. Lynn. Macro dark matter. *Monthly Notices of the Royal Astronomical Society*, 450(4):3418–3430, May 2015.

[238] David Norman Jamieson, C Yang, T Hopf, SM Hearne, Christopher Ian Pakes, S Prawer, M Mitic, E Gauja, SE Andresen, FE Hudson, et al. Controlled shallow single-ion implantation in silicon using an active substrate for sub-20-kev ions. *Applied Physics Letters*, 86(20):202101, 2005.

[239] A. Jarmola, V. M. Acosta, K. Jensen, S. Chemerisov, and D. Budker. Temperature- and magnetic-field-dependent longitudinal spin relaxation in nitrogen-vacancy ensembles in diamond. *Phys. Rev. Lett.*, 108:197601, May 2012.

[240] Jean-Christophe Jaskula, Erik Bauch, Silvia Arroyo-Camejo, Mikhail D. Lukin, Stefan W. Hell, Alexei S. Trifonov, and Ronald L. Walsworth. Superresolution optical magnetic imaging and spectroscopy using individual electronic spins in diamond. *Optics Express*, 25(10):11048–11064, May 2017.

[241] Hunmoo Jeon and Michael J. Longo. Search for magnetic monopoles trapped in matter. *Phys. Rev. Lett.*, 75:1443–1446, 1995. [Erratum: Phys.Rev.Lett. 76, 159 (1996)].

[242] Junu Jeong, SungWoo Youn, Sungjae Bae, Jihngeun Kim, Taehyeon Seong, Jihn E. Kim, and Yannis K. Semertzidis. Search for Invisible Axion Dark Matter with a Multiple-Cell Haloscope. *Phys. Rev. Lett.*, 125(22):221302, 2020.

[243] U. Johansson, D. Carbone, S. Kalbfleisch, A. Bjorling, A. Rodriguez-Frenandez, T. Stankevic, M. Liebi, B. Bring, A. Mikkelsen, U. Vogt, and et al. Initial operation of the nanomax beamline at max iv. *Microscopy and Microanalysis*, 24(S2):250–251, 2018.

[244] Johnathon R. Jordan, Sebastian Baum, Patrick Stengel, Alfredo Ferrari, Maria Cristina Morone, Paola Sala, and Joshua Spitz. Measuring Changes in the Atmospheric Neutrino Rate Over Gigayear Timescales. *Phys. Rev. Lett.*, 125(23):231802, 2020.

[245] S. Karanth et al. First Search for Axion-Like Particles in a Storage Ring Using a Polarized Deuteron Beam. 8 2022.

[246] P. Kehayias, M. J. Turner, R. Trubko, J. M. Schloss, C. A. Hart, M. Wesson, D. R. Glenn, and R. L. Walsworth. Imaging crystal stress in diamond using ensembles of nitrogen-vacancy centers. *Physical Review B*, 100(17), Nov 2019.

[247] Michael A. Keim, Valeriya Korol, and Elena M. Rossi. The large magellanic cloud revealed in gravitational waves with LISA. *Mon. Not. Roy. Astron. Soc.*, 521(1):1088–1098, 2023.

[248] Philipp J Keller and Misha B Ahrens. Visualizing whole-brain activity and development at the single-cell level using light-sheet microscopy. *Neuron*, 85(3):462–483, 2015.

[249] Hyungjin Kim and Gilad Perez. Oscillations of atomic energy levels induced by QCD axion dark matter. 5 2022.

[250] On Kim and Yannis K. Semertzidis. New method of probing an oscillating EDM induced by axionlike dark matter using an rf Wien filter in storage rings. *Phys. Rev. D*, 104(9):096006, 2021.

[251] Vincent B. . Klaer and Guy D. Moore. The dark-matter axion mass. *JCAP*, 11:049, 2017.

[252] Archil Kobakhidze and Matthew Talia. Supersymmetric Naturalness Beyond MSSM. *JHEP*, 08:105, 2019.

[253] Juna A. Kollmeier et al. SDSS-V: Pioneering Panoptic Spectroscopy. *arXiv e-prints*, page arXiv:1711.03234, November 2017.

[254] Philipp Konzelmann, Torsten Rendler, Ville Bergholm, Andrea Zappe, Veronika Pfannenstill, Marwa Garsi, Florestan Ziem, Matthias Niethammer, Matthias Widmann, Sang-Yun Lee, Philipp Neumann, and Jörg Wrachtrup. Robust and efficient quantum optimal control of spin probes in a complex (biological) environment. towards sensing of fast temperature fluctuations. *New Journal of Physics*, 20(12):123013, Dec 2018.

[255] V. Korol et al. Populations of double white dwarfs in Milky Way satellites and their detectability with LISA. *Astron. Astrophys.*, 638:A153, 2020.

[256] Valeriya Korol, Vasily Belokurov, Christopher J. Moore, and Silvia Toonen. Weighing Milky Way Satellites with LISA. *Mon. Not. Roy. Astron. Soc.*, 502(1):L55–L60, 2021.

[257] Valeriya Korol, Na'ama Hallakoun, Silvia Toonen, and Nikolaos Karnesis. Observationally driven Galactic double white dwarf population for LISA. *Mon. Not. Roy. Astron. Soc.*, 511(4):5936–5947, 2022.

[258] Valeriya Korol, Elena M. Rossi, and Enrico Barausse. A multimessenger study of the Milky Way's stellar disc and bulge with LISA, Gaia, and LSST. *Mon. Not. Roy. Astron. Soc.*, 483(4):5518–5533, 2019.

[259] Valeriya Korol, Elena M. Rossi, Paul J. Groot, Gijs Nelemans, Silvia Toonen, and Anthony G. A. Brown. Prospects for detection of detached double white dwarf binaries with Gaia, LSST and LISA. *Mon. Not. Roy. Astron. Soc.*, 470(2):1894–1910, 2017.

[260] T. S. Kosmas, O. G. Miranda, D. K. Papoulias, M. Tórtola, and J. W. F. Valle. Probing neutrino magnetic moments at the spallation neutron source facility. *Phys. Rev. D*, 92:013011, Jul 2015.

[261] T. S. Kosmas, D. K. Papoulias, M. Tórtola, and J. W. F. Valle. Probing light sterile neutrino signatures at reactor and spallation neutron source neutrino experiments. *Physical Review D*, 96(6), Sep 2017.

[262] J. J. M. Kouwenberg, H. T. Wolterbeek, A. G. Denkova, and A. J. J. Bos. Fluorescent nuclear track detectors for alpha radiation microdosimetry. *Radiation Oncology (London, England)*, 13, Jun 2018.

[263] Joseph M. Kovalik and Joseph L. Kirschvink. New superconducting-quantum-interference-device-based constraints on the abundance of magnetic monopoles trapped in matter: An investigation of deeply buried rocks. *Phys. Rev. A*, 33:1183–1187, Feb 1986.

[264] Lawrence M. Krauss. Low-energy neutrino detection and precision tests of the standard model. *Physics Letters B*, 269(3-4):407–411, October 1991.

[265] G. Kucsko, P. C. Maurer, N. Y. Yao, M. Kubo, H. J. Noh, P. K. Lo, H. Park, and M. D. Lukin. Nanometre-scale thermometry in a living cell. *Nature*, 500(74607460):54–58, Aug 2013.

[266] Michael Kuhlen, Mariangela Lisanti, and David N. Spergel. Direct detection of dark matter debris flows. *Physical Review D*, 86(6), Sep 2012.

[267] Michael Kuhlen, Mark Vogelsberger, and Raul Angulo. Numerical Simulations of the Dark Universe: State of the Art and the Next Decade. *Phys. Dark Univ.*, 1:50–93, 2012.

[268] T. Kupfer, V. Korol, S. Shah, G. Nelemans, T. R. Marsh, G. Ramsay, P. J. Groot, D. T. H. Steeghs, and E. M. Rossi. LISA verification binaries with updated distances from Gaia Data Release 2. , 480(1):302–309, October 2018.

[269] Thomas Kupfer et al. LISA Galactic binaries with astrometry from Gaia DR3. 2 2023.

[270] Noah Alexander Kurinsky, To Chin Yu, Yonit Hochberg, and Blas Cabrera. Diamond Detectors for Direct Detection of Sub-GeV Dark Matter. *Phys. Rev. D*, 99(12):123005, 2019.

[271] Alexander Kusenko and Mikhail E. Shaposhnikov. Supersymmetric Q balls as dark matter. *Phys. Lett. B*, 418:46–54, 1998.

[272] Ohjoon Kwon et al. First Results from an Axion Haloscope at CAPP around 10.7 μeV. *Phys. Rev. Lett.*, 126(19):191802, 2021.

[273] A. B. Lahanas. LSP as a Candidate for Dark Matter. *Lect. Notes Phys.*, 720:35–68, 2007.

[274] Astrid Lamberts, Sarah Blunt, Tyson B. Littenberg, Shea Garrison-Kimmel, Thomas Kupfer, and Robyn E. Sanderson. Predicting the LISA white dwarf binary population in the Milky Way with cosmological simulations. *Mon. Not. Roy. Astron. Soc.*, 490(4):5888–5903, 2019.

[275] Astrid Lamberts, Sarah Blunt, Tyson B. Littenberg, Shea Garrison-Kimmel, Thomas Kupfer, and Robyn E. Sanderson. Predicting the LISA white dwarf binary population in the Milky Way with cosmological simulations. , 490(4):5888–5903, December 2019.

[276] Chervin FP Laporte, Ivan Minchev, Kathryn V Johnston, and Facundo A Gómez. Footprints of the sagittarius dwarf galaxy in the gaia data set. *Monthly Notices of the Royal Astronomical Society*, 485(3):3134–3152, 2019.

[277] William P. Leeman, Colin M. MacRae, Nick C. Wilson, Aaron Torpy, Cin-Ty A. Lee, James J. Student, Jay B. Thomas, and Edward P. Vicenzi. A study of cathodoluminescence and trace element compositional zoning in natural quartz from volcanic rocks: Mapping titanium content in quartz. *Microscopy and Microanalysis*, 18(6):1322–1341, 2012.

[278] Benjamin V. Lehmann, Christian Johnson, Stefano Profumo, and Thomas Schwemberger. Direct detection of primordial black hole relics as dark matter. *JCAP*, 10:046, 2019.

[279] Markus Leidinger, Stephan Fieberg, Niklas Waasem, Frank Kühnemann, Karsten Buse, and Ingo Breunig. Comparative study on three highly sensitive absorption measurement techniques characterizing lithium niobate over its entire transparent spectral range. *Optics express*, 23(17):21690–21705, 2015.

[280] Hugues Leroux, Wolf Uwe Reimold, and Jean-Claude Doukhan. A tem investigation of shock metamorphism in quartz from the vredefort dome, south africa. *Tectonophysics*, 230(3-4):223–239, 1994.

[281] Yu. Levin. Internal thermal noise in the LIGO test masses: A Direct approach. *Phys. Rev. D*, 57:659–663, 1998.

[282] Edlyn V Levine, Matthew J Turner, Pauli Kehayias, Connor A Hart, Nicholas Langellier, Raisa Trubko, David R Glenn, Roger R Fu, and Ronald L Walsworth. Principles and techniques of the quantum diamond microscope. *Nanophotonics*, 8(11):1945–1973, 9 2019.

[283] S Lischke, A Peczek, JS Morgan, K Sun, D Steckler, Y Yamamoto, F Korndörfer, C Mai, S Marschmeyer, M Fraschke, et al. Ultra-fast germanium photodiode with 3-db bandwidth of 265 ghz. *Nature Photonics*, 15(12):925–931, 2021.

[284] Tyson B. Littenberg and Ananthu K. Lali. Have any LISA verification binaries been found? 4 2024.

[285] Tyson B. Littenberg, Shane L. Larson, Gijs Nelemans, and Neil J. Cornish. Prospects for observing ultra-compact binaries with space-based gravitational wave interferometers and optical telescopes. *Mon. Not. Roy. Astron. Soc.*, 429:2361, 2013.

[286] Tyson B. Littenberg and Nicolas Yunes. Binary White Dwarfs as Laboratories for Extreme Gravity with LISA. *Class. Quant. Grav.*, 36(9):095017, 2019.

[287] Hongwan Liu, Brodi D. Elwood, Matthew Evans, and Jesse Thaler. Searching for Axion Dark Matter with Birefringent Cavities. *Phys. Rev. D*, 100(2):023548, 2019.

[288] Jesse Liu et al. Broadband Solenoidal Haloscope for Terahertz Axion Detection. *Phys. Rev. Lett.*, 128(13):131801, 2022.

[289] Abraham Loeb and Neal Weiner. Cores in Dwarf Galaxies from Dark Matter with a Yukawa Potential. *Phys. Rev. Lett.*, 106:171302, 2011.

[290] E. Lopez Asamar. SuperCDMS SNOLAB: status and prospects for measuring the coherent neutrino scattering. *J. Phys. Conf. Ser.*, 1216(1):012020, 2019.

[291] LSST Science Collaboration, Paul A. Abell, et al. LSST Science Book, Version 2.0. *arXiv e-prints*, page arXiv:0912.0201, December 2009.

[292] CM MacRae, NC Wilson, and A Torpy. Hyperspectral cathodoluminescence. *Mineralogy and Petrology*, 107(3):429–440, 2013.

[293] David J. E. Marsh. Axion Cosmology. *Phys. Rept.*, 643:1–79, 2016.

[294] Thomas Richard Marsh and G. Nelemans. Period changes in ultracompact double white dwarfs. *Mon. Not. Roy. Astron. Soc.*, 363:581–585, 2005.

[295] Mason C. Marshall, Reza Ebadi, Connor Hart, Matthew J. Turner, Mark J. H. Ku, David F. Phillips, and Ronald L. Walsworth. High-Precision Mapping of Diamond Crystal Strain Using Quantum Interferometry. *Phys. Rev. Applied*, 17(2):024041, 2022.

[296] Mason C. Marshall, David F. Phillips, Matthew J. Turner, Mark J. H. Ku, Tao Zhou, Nazar Delegan, F. Joseph Heremans, Martin V. Holt, and Ronald L. Walsworth. Scanning x-ray diffraction microscopy for diamond quantum sensing. *Phys. Rev. Applied*, 16:054032, Nov 2021.

[297] Mason C. Marshall, Matthew J. Turner, Mark J. H. Ku, David F. Phillips, and Ronald L. Walsworth. Directional detection of dark matter with diamond. *Quantum Sci. Technol.*, 6(2):024011, 2021.

[298] P M Martineau, M P Gaukroger, K B Guy, S C Lawson, D J Twitchen, I Friel, J O Hansen, G C Summerton, T P G Addison, and R Burns. High crystalline quality single crystal chemical vapour deposition diamond. *Journal of Physics: Condensed Matter*, 21(36):364205, aug 2009.

[299] Philip M Martineau, Simon C Lawson, Andy J Taylor, Samantha J Quinn, David JF Evans, and Michael J Crowder. Identification of synthetic diamond grown using chemical vapor deposition (cvd). *Gems & Gemology*, 40(1):2–25, 2004.

[300] Denis Martynov and Haixing Miao. Quantum-enhanced interferometry for axion searches. *Phys. Rev. D*, 101(9):095034, 2020.

[301] Allison M. Matthews et al. The NANOGrav Nine-year Data Set: Astrometric Measurements of 37 Millisecond Pulsars. *Astrophys. J.*, 818(1):92, 2016.

[302] P.C. Maurer, J.R. Maze, P.L. Stanwix, L. Jiang, A.V. Gorshkov, A.A. Zibrov, B. Harke, J.S. Hodges, A.S. Zibrov, A. Yacoby, D. Twitchen, S.W. Hell, R.L. Walsworth, and M.D. Lukin. Far-field optical imaging and manipulation of individual spins with nanoscale resolution. *Nature Physics*, 6(1111):912–918, Nov 2010.

[303] F. Mayet et al. A review of the discovery reach of directional Dark Matter detection. *Phys. Rept.*, 627:1–49, 2016.

[304] Jeronimo R Maze, Paul L Stanwix, James S Hodges, Seungpyo Hong, Jacob M Taylor, Paola Cappellaro, Liang Jiang, MV Gurudev Dutt, Emre Togan, AS Zibrov, et al. Nanoscale magnetic sensing with an individual electronic spin in diamond. *Nature*, 455(7213):644–647, 2008.

[305] Ben T. McAllister, Graeme Flower, Justin Kruger, Eugene N. Ivanov, Maxim Goryachev, Jeremy Bourhill, and Michael E. Tobar. The ORGAN Experiment: An axion haloscope above 15 GHz. *Phys. Dark Univ.*, 18:67–72, 2017.

[306] Srujan Meesala, Young-Ik Sohn, Benjamin Pingault, Linbo Shao, Haig A. Atikian, Jeffrey Holzgrafe, Mustafa Gündoğan, Camille Stavrakas, Alp Sipahigil, Cleaven Chia, and et al. Strain engineering of the silicon-vacancy center in diamond. *Physical Review B*, 97(20), May 2018.

[307] Yohai Meiron, Bence Kocsis, and Abraham Loeb. Detecting triple systems with gravitational wave observations. *Astrophys. J.*, 834(2):200, 2017.

[308] A. Álvarez Melcón et al. First results of the CAST-RADES haloscope search for axions at 34.67 μeV. *JHEP*, 21:075, 2020.

[309] Adrian C. Melissinos. Search for Cosmic Axions using an Optical Interferometer. *Phys. Rev. Lett.*, 102:202001, 2009.

[310] Kentaro Miuchi, Hironobu Nishimura, Kaori Hattori, Naoki Higashi, Chihiro Ida, Satoshi Iwaki, Shigeto Kabuki, Hidetoshi Kubo, Shunsuke Kurosawa, Kiseki Nakamura, and et al. First underground results with newage-0.3a direction-sensitive dark matter detector. *Physics Letters B*, 686(1):11–17, Mar 2010.

[311] M. Miyamoto and R. Nagai. Three-dimensional models for the distribution of mass in galaxies. , 27:533–543, January 1975.

[312] Istvan Mohacsi, Ismo Vartiainen, Benedikt Rosner, Manuel Guizar-Sicairos, Vitaliy A. Guzenko, Ian McNulty, Robert Winarski, Martin V. Holt, and Christian David. Interlaced zone plate optics for hard x-ray imaging in the 10 nm range. *Scientific Reports*, 7(11):43624, Mar 2017.

[313] Jocelyn Monroe and Peter Fisher. Neutrino backgrounds to dark matter searches. *Physical Review D*, 76(3), Aug 2007.

[314] Moreton Moore. Imaging diamond with x-rays. *Journal of Physics: Condensed Matter*, 21(36):364217, aug 2009.

[315] Abigail Moran, Chiara M. F. Mingarelli, Ken Van Tilburg, and Deborah Good. A Pulsar-Based Map of Galactic Acceleration. *arXiv e-prints*, page arXiv:2306.13137, June 2023.

[316] Andreas Muller, Edward B Flagg, John R Lawall, and Glenn S Solomon. Ultrahigh-finesse, low-mode-volume fabry–perot microcavity. *Optics letters*, 35(13):2293–2295, 2010.

[317] James Munday et al. Two decades of optical timing of the shortest-period binary star system HM Cancri. *Mon. Not. Roy. Astron. Soc.*, 518(4):5123–5139, 2022.

[318] Masatsugu Nagai, Kazuhiro Nakanishi, Hiraku Takahashi, Hiromitsu Kato, Toshiharu Makino, Satoshi Yamasaki, Tsubasa Matsumoto, Takao Inokuma, and Norio Tokuda. Anisotropic diamond etching through thermochemical reaction between ni and diamond in high-temperature water vapour. *Scientific Reports*, 8(11):6687, Apr 2018.

[319] Koji Nagano, Tomohiro Fujita, Yuta Michimura, and Ippei Obata. Axion Dark Matter Search with Interferometric Gravitational Wave Detectors. *Phys. Rev. Lett.*, 123(11):111301, 2019.

[320] Julio F. Navarro, Carlos S. Frenk, and Simon D. M. White. The Structure of Cold Dark Matter Halos. , 462:563, May 1996.

[321] E Nazaretski, H Yan, K Lauer, N Bouet, X Huang, W Xu, J Zhou, D Shu, Y Hwu, and YS Chu. Design and performance of an x-ray scanning microscope at the hard x-ray nanoprobe beamline of nsls-ii. *Journal of Synchrotron Radiation*, 24(6):1113–1119, 2017.

[322] Lina Necib, Mariangela Lisanti, and Vasily Belokurov. Inferred evidence for dark matter kinematic substructure with SDSS–gaia. *Astrophys. J.*, 874(1):3, mar 2019.

[323] Lina Necib, Bryan Ostdiek, Mariangela Lisanti, Timothy Cohen, Marat Freytsis, and Shea Garrison-Kimmel. Chasing accreted structures within gaia dr2 using deep learning. *The Astrophysical Journal*, 903(1):25, Oct 2020.

[324] G. Nelemans, L. R. Yungelson, S. F. Portegies Zwart, and F. Verbunt. Population synthesis for double white dwarfs . I. Close detached systems. , 365:491–507, January 2001.

[325] P. Neumann, I. Jakobi, F. Dolde, C. Burk, R. Reuter, G. Waldherr, J. Honert, T. Wolf, A. Brunner, J.H. Shim, D. Suter, H. Sumiya, J. Isoya, and J. Wrachtrup. High-precision nanoscale temperature sensing using single defects in diamond. *Nano Letters*, 13(6):2738–2742, Jun 2013.

[326] Heidi Jo Newberg et al. The Ghost of Sagittarius and Lumps in the Halo of the Milky Way. *Astrophys. J.*, 569:245–274, 2002.

[327] D Nicolodi, WF McGrew, RJ Fasano, X Zhang, M Schioppo, K Beloy, and AD Ludlow. A cryogenic high-finesse optical cavity to improve the stability of yb optical lattice clocks. In *2018 IEEE International Frequency Control Symposium (IFCS)*, pages 1–2. IEEE, 2018.

[328] M. Niklas, J. A. Bartz, M. S. Akselrod, A. Abollahi, O. Jäkel, and S. Greilich. Ion track reconstruction in 3d using alumina-based fluorescent nuclear track detectors. *Physics in Medicine and Biology*, 58(18):N251–N266, Aug 2013.

[329] Martin Niklas, Steffen Greilich, Claudius Melzig, Mark S. Akselrod, Jürgen Debus, Oliver Jäkel, and Amir Abdollahi. Engineering cell-fluorescent ion track hybrid detectors. *Radiation Oncology*, 8(1):141, Jun 2013.

[330] D R Nygren. Columnar recombination: a tool for nuclear recoil directional sensitivity in a xenon-based direct detection WIMP search. *Journal of Physics: Conference Series*, 460:012006, oct 2013.

[331] Ippei Obata, Tomohiro Fujita, and Yuta Michimura. Optical Ring Cavity Search for Axion Dark Matter. *Phys. Rev. Lett.*, 121(16):161301, 2018.

[332] A. Oh. Diamond particle detectors systems in high energy physics. *Journal of Instrumentation*, 10(04):C04038–C04038, apr 2015.

[333] Ciaran O'Hare. cajohare/axionlimits: Axionlimits. https://cajohare.github.io/AxionLimits/, July 2020.

[334] Ciaran A. J. O'Hare. Can we overcome the neutrino floor at high masses? *Physical Review D*, 102(6), Sep 2020.

[335] Ciaran A. J. O'Hare, Anne M. Green, Julien Billard, Enectali Figueroa-Feliciano, and Louis E. Strigari. Readout strategies for directional dark matter detection beyond the neutrino background. *Physical Review D*, 92(6), Sep 2015.

[336] Ciaran A. J. O'Hare, Christopher McCabe, N. Wyn Evans, GyuChul Myeong, and Vasily Belokurov. Dark matter hurricane: Measuring the S1 stream with dark matter detectors. *Phys. Rev. D*, 98(10):103006, 2018.

[337] Shinobu Onoda, Moriyoshi Haruyama, Tokuyuki Teraji, Junichi Isoya, Wataru Kada, Osamu Hanaizumi, and Takeshi Ohshima. New application of nv centers in cvd diamonds as a fluorescent nuclear track detector. *physica status solidi (a)*, 212(11):2641–2644, 2015.

[338] Shinobu Onoda, Kazumasa Tatsumi, Moriyoshi Haruyama, Tokuyuki Teraji, Junichi Isoya, Wataru Kada, Takeshi Ohshima, and Osamu Hanaizumi. Diffusion of vacancies created by high-energy heavy ion strike into diamond. *physica status solidi (a)*, 214(11):1700160, 2017.

[339] M. Diaz Ortiz et al. Design of the ALPS II optical system. *Phys. Dark Univ.*, 35:100968, 2022.

[340] Yuka Oshima, Hiroki Fujimoto, Jun'ya Kume, Soichiro Morisaki, Koji Nagano, Tomohiro Fujita, Ippei Obata, Atsushi Nishizawa, Yuta Michimura, and Masaki Ando. First Results of Axion Dark Matter Search with DANCE. 3 2023.

[341] Jonathan Ouellet and Zachary Bogorad. Solutions to Axion Electrodynamics in Various Geometries. *Phys. Rev. D*, 99(5):055010, 2019.

[342] Ciaran A. J. O'Hare. New definition of the neutrino floor for direct dark matter searches. *Physical Review Letters*, 127(25), Dec 2021.

[343] JL Pacheco, M Singh, DL Perry, JR Wendt, G Ten Eyck, RP Manginell, T Pluym, DR Luhman, MP Lilly, MS Carroll, et al. Ion implantation for deterministic single atom devices. *Review of Scientific Instruments*, 88(12):123301, 2017.

[344] Paolo Pani. Binary pulsars as dark-matter probes. *Phys. Rev. D*, 92(12):123530, 2015.

[345] Kelly Patton, Jonathan Engel, Gail C. McLaughlin, and Nicolas Schunck. Neutrino-nucleus coherent scattering as a probe of neutron density distributions. *Phys. Rev. C*, 86:024612, Aug 2012.

[346] R. D. Peccei and Helen R. Quinn. CP Conservation in the Presence of Instantons. *Phys. Rev. Lett.*, 38:1440–1443, 1977.

[347] Michael E Peskin. Supersymmetric dark matter in the harsh light of the large hadron collider. *Proceedings of the National Academy of Sciences*, 112(40):12256–12263, 2015.

[348] P. C. Peters. Gravitational Radiation and the Motion of Two Point Masses. *Phys. Rev.*, 136:B1224–B1232, 1964.

[349] P. C. Peters and J. Mathews. Gravitational radiation from point masses in a Keplerian orbit. *Phys. Rev.*, 131:435–439, 1963.

[350] Franz Pfeiffer. X-ray ptychography. *Nature Photonics*, 12(1):9–17, Jan 2018.

[351] Matthias Pfender, Nabeel Aslam, Gerald Waldherr, Philipp Neumann, and Jörg Wrachtrup. Single-spin stochastic optical reconstruction microscopy. *Proceedings of the National Academy of Sciences*, 111(41):14669–14674, Oct 2014.

[352] David F. Phillips, Aakash Ravi, Reza Ebadi, and Ronald L. Walsworth. Milky Way Accelerometry via Millisecond Pulsar Timing. *Phys. Rev. Lett.*, 126(14):141103, 2021.

[353] H. Pinto, R. Jones, J. P. Goss, and P. R. Briddon. Point and extended defects in chemical vapour deposited diamond. *Journal of Physics: Conference Series*, 281:012023, Feb 2011.

[354] Peter E Powers and Joseph W Haus. *Fundamentals of nonlinear optics*. CRC press, 2017.

[355] John Preskill, Mark B. Wise, and Frank Wilczek. Cosmology of the Invisible Axion. *Phys. Lett. B*, 120:127–132, 1983.

[356] Jörg Pretz, Swathi Karanth, E. Stephenson, Seung Pyo Chang, Volker Hejny, Seongtae Park, Yannis Semertzidis, and Hans Ströher. Statistical sensitivity estimates for oscillating electric dipole moment measurements in storage rings. *Eur. Phys. J. C*, 80(2):107, 2020.

[357] P. B. Price, Shi-lun Guo, S. P. Ahlen, and R. L. Fleischer. Search for grand-unified-theory magnetic monopoles at a flux level below the parker limit. *Phys. Rev. Lett.*, 52:1265–1268, Apr 1984.

[358] P. B. Price and M. H. Salamon. Search for supermassive magnetic monopoles using mica crystals. *Phys. Rev. Lett.*, 56:1226–1229, Mar 1986.

[359] T. Prusti et al. The Gaia Mission. *Astron. Astrophys.*, 595(Gaia Data Release 1):A1, 2016.

[360] Sarika Pugla. *Ultrastable high finesse cavities for laser frequency stabilization*. PhD thesis, Imperial College London, 2008.

[361] Claudia Quercellini, Luca Amendola, and Amedeo Balbi. Mapping the galactic gravitational potential with peculiar acceleration. *Mon. Not. Roy. Astron. Soc.*, 391:1308–1314, 2008.

[362] Aaron P. Quiskamp, Ben T. McAllister, Paul Altin, Eugene N. Ivanov, Maxim Goryachev, and Michael E. Tobar. Direct search for dark matter axions excluding ALP cogenesis in the 63- to 67-μeV range with the ORGAN experiment. *Sci. Adv.*, 8(27):abq3765, 2022.

[363] I. I. Rabi. Space quantization in a gyrating magnetic field. *Phys. Rev.*, 51:652–654, Apr 1937.

[364] Roberto Raddi, Santiago Torres, Alberto Rebassa-Mansergas, Jesús Maldonado, María E. Camisassa, Detlev Koester, Nicola Pietro Gentile Fusillo, Pier-Emmanuel Tremblay, Markus Dimpel, Ulrich Heber, Tim Cunningham, and Juan-Juan Ren. Kinematic properties of white dwarfs. Galactic orbital parameters and age-velocity dispersion relation. , 658:A22, February 2022.

[365] A. T. M. Anishur Rahman. Ultrawideband axion search using a faraday haloscope. *Phys. Rev. D*, 106:115017, Dec 2022.

[366] Surjeet Rajendran. New directions in the search for dark matter. *SciPost Phys. Lect. Notes*, 56:1, 2022.

[367] Surjeet Rajendran, Nicholas Zobrist, Alexander O. Sushkov, Ronald Walsworth, and Mikhail Lukin. A method for directional detection of dark matter using spectroscopy of crystal defects. *Phys. Rev. D*, 96(3):035009, 2017.

[368] Norman F. Ramsey. A molecular beam resonance method with separated oscillating fields. *Phys. Rev.*, 78:695–699, Jun 1950.

[369] Lisa Randall and Zhong-Zhi Xianyu. A Direct Probe of Mass Density Near Inspiraling Binary Black Holes. *Astrophys. J.*, 878(2):75, 2019.

[370] Birger Rasmussen, Ian R Fletcher, Janet R Muhling, and Simon A Wilde. In situ u–th–pb geochronology of monazite and xenotime from the jack hills belt: Implications for the age of deposition and metamorphism of hadean zircons. *Precambrian Research*, 180(1-2):26–46, 2010.

[371] W. Rau. SuperCDMS SNOLAB - Status and Plans. *J. Phys. Conf. Ser.*, 1342(1):012077, 2020.

[372] Aakash Ravi, Nicholas Langellier, David F. Phillips, Malte Buschmann, Benjamin R. Safdi, and Ronald L. Walsworth. Probing Dark Matter Using Precision Measurements of Stellar Accelerations. *Phys. Rev. Lett.*, 123(9):091101, 2019.

[373] Steven Rieck, Alexander W. Criswell, Valeriya Korol, Michael A. Keim, Malachy Bloom, and Vuk Mandic. LISA Detectability of a Stochastic Gravitational Wave Background from Unresolved White Dwarf Binaries in the LMC. 8 2023.

[374] Eva Rittweger, Kyu Young Han, Scott E. Irvine, Christian Eggeling, and Stefan W. Hell. Sted microscopy reveals crystal colour centres with nanometric resolution. *Nature Photonics*, 3(33):144–147, Mar 2009.

[375] Travis Robson, Neil J. Cornish, and Chang Liu. The construction and use of LISA sensitivity curves. *Class. Quant. Grav.*, 36(10):105011, 2019.

[376] Travis Robson, Neil J. Cornish, Nicola Tamanini, and Silvia Toonen. Detecting hierarchical stellar systems with LISA. *Phys. Rev. D*, 98(6):064012, 2018.

[377] Elinore Roebber et al. Milky Way Satellites Shining Bright in Gravitational Waves. *Astrophys. J. Lett.*, 894(2):L15, 2020.

[378] A. Romanenko et al. New Exclusion Limit for Dark Photons from an SRF Cavity-Based Search (Dark SRF). 1 2023.

[379] Sanaea C. Rose, Smadar Naoz, Abhimat K. Gautam, Andrea M. Ghez, Tuan Do, Devin Chu, and Eric Becklin. On Socially Distant Neighbors: Using Binaries to Constrain the Density of Objects in the Galactic Center. , 904(2):113, December 2020.

[380] T. Rosskopf, A. Dussaux, K. Ohashi, M. Loretz, R. Schirhagl, H. Watanabe, S. Shikata, K. M. Itoh, and C. L. Degen. Investigation of surface magnetic noise by shallow spins in diamond. *Phys. Rev. Lett.*, 112:147602, Apr 2014.

[381] Leszek Roszkowski, Enrico Maria Sessolo, and Sebastian Trojanowski. Wimp dark matter candidates and searches—current status and future prospects. *Reports on Progress in Physics*, 81(6):066201, May 2018.

[382] Leszek Roszkowski, Enrico Maria Sessolo, and Andrew J. Williams. Prospects for dark matter searches in the pMSSM. *JHEP*, 02:014, 2015.

[383] Tanya S. Roussy et al. Experimental Constraint on Axionlike Particles over Seven Orders of Magnitude in Mass. *Phys. Rev. Lett.*, 126(17):171301, 2021.

[384] F. Ruppin, J. Billard, E. Figueroa-Feliciano, and L. Strigari. Complementarity of dark matter detectors in light of the neutrino background. *Physical Review D*, 90(8), Oct 2014.

[385] Brian G Rusk, Heather A Lowers, and Mark H Reed. Trace elements in hydrothermal quartz: Relationships to cathodoluminescent textures and insights into vein formation. *Geology*, 36(7):547–550, 2008.

[386] Chiara P. Salemi et al. Search for Low-Mass Axion Dark Matter with ABRACADABRA-10 cm. *Phys. Rev. Lett.*, 127(8):081801, 2021.

[387] D. Santos, J. Billard, G. Bosson, J. L. Bouly, O. Bourrion, Ch. Fourel, O. Guillaudin, F. Mayet, J. P. Richer, A. Delbart, E. Ferrer, I. Giomataris, F. J. Iguaz, J. P. Mols, C. Golabek, and L. Lebreton. Mimac: A micro-tpc matrix project for directional detection of dark matter. 2011.

[388] Sebastian Sassi, Abolfazl Dinmohammadi, Matti Heikinheimo, Nader Mirabolfathi, Kai Nordlund, Hossein Safari, and Kimmo Tuominen. Solar neutrinos and dark matter detection with diurnal modulation. *Physical Review D*, 104(6), Sep 2021.

[389] Laura Sberna et al. Observing GW190521-like binary black holes and their environment with LISA. *Phys. Rev. D*, 106(6):064056, 2022.

[390] Romana Schirhagl, Kevin Chang, Michael Loretz, and Christian L. Degen. Nitrogen-vacancy centers in diamond: Nanoscale sensors for physics and biology. *Annual Review of Physical Chemistry*, 65(1):83–105, 2014.

[391] Jennifer M. Schloss, John F. Barry, Matthew J. Turner, and Ronald L. Walsworth. Simultaneous broadband vector magnetometry using solid-state spins. *Phys. Rev. Applied*, 10:034044, Sep 2018.

[392] Richard W. Schnee et al. The SuperCDMS Experiment. In *5th International Heidelberg Conference on Dark Matter in Astro and Particle Physics*, 2 2005.

[393] B. J. Scholz, A. E. Chavarria, J. I. Collar, P. Privitera, and A. E. Robinson. Measurement of the low-energy quenching factor in germanium using an ^{88}Y/Be photoneutron source. *Phys. Rev. D*, 94:122003, Dec 2016.

[394] Ralph Schönrich and Walter Dehnen. Warp, waves, and wrinkles in the milky way. *Monthly Notices of the Royal Astronomical Society*, 478(3):3809–3824, 2018.

[395] David N. Schramm and W. David Arnett. Neutral currents and supernovas. *Phys. Rev. Lett.*, 34:113–116, Jan 1975.

[396] Ivo Schulthess et al. New Limit on Axionlike Dark Matter Using Cold Neutrons. *Phys. Rev. Lett.*, 129(19):191801, 2022.

[397] Marc Schumann. Direct Detection of WIMP Dark Matter: Concepts and Status. *J. Phys. G*, 46(10):103003, 2019.

[398] JA Seamons, E Bielejec, Malcolm S Carroll, and Kenton D Childs. Room temperature single ion detection with geiger mode avalanche diode detectors. *Applied Physics Letters*, 93(4):043124, 2008.

[399] Hiroyuki Sekiya, M. Minowa, Y. Shimizu, Y. Inoue, and W. Suganuma. Measurements of anisotropic scintillation efficiency for carbon recoils in a stilbene crystal for dark matter detection. *Phys. Lett. B*, 571:132–138, 2003.

[400] Yannis K. Semertzidis and SungWoo Youn. Axion dark matter: How to see it? *Sci. Adv.*, 8(8):abm9928, 2022.

[401] Naoki Seto. Long term operation of LISA and galactic close white dwarf binaries. *Mon. Not. Roy. Astron. Soc.*, 333:469, 2002.

[402] Naoki Seto. Detecting Planets around Compact Binaries with Gravitational Wave Detectors in Space. *Astrophys. J. Lett.*, 677:L55–L58, 2008.

[403] Naoki Seto. Potential tertiary effects on the LISA verification binary HM Cancri. *Mon. Not. Roy. Astron. Soc.*, 524(4):5442–5445, 2023.

[404] S. Shah, M. van der Sluys, and G. Nelemans. Using electromagnetic observations to aid gravitational-wave parameter estimation of compact binaries observed with LISA. , 544:A153, August 2012.

[405] Sweta Shah and Gijs Nelemans. Measuring Tides and Binary Parameters from Gravitational Wave Data and Eclipsing Timings of Detached White Dwarf Binaries. , 791(2):76, August 2014.

[406] Sweta Shah, Gijs Nelemans, and Marc van der Sluys. Using electromagnetic observations to aid gravitational-wave parameter estimation of compact binaries observed with LISA II: The effect of knowing the sky position. *Astron. Astrophys.*, 553:A82, 2013.

[407] Brett Shapiro, Rana X. Adhikari, Odylio Aguiar, Edgard Bonilla, Danyang Fan, Litawn Gan, Ian Gomez, Sanditi Khandelwal, Brian Lantz, Tim MacDonald, and Dakota Madden-Fong. Cryogenically cooled ultra low vibration silicon mirrors for gravitational wave observatories. *Cryogenics*, 81:83–92, 2017.

[408] Sanjib Sharma et al. Fundamental relations for the velocity dispersion of stars in the Milky Way. , 506(2):1761–1776, September 2021.

[409] Yuki Shimizu, M. Minowa, H. Sekiya, and Y. Inoue. Directional scintillation detector for the detection of the wind of WIMPs. *Nucl. Instrum. Meth. A*, 496:347–352, 2003.

[410] I. S. Shklovskii. Possible Causes of the Secular Increase in Pulsar Periods. , 13:562, February 1970.

[411] Jagjit Singh Sidhu, Glenn Starkman, and Ralph Harvey. Counter-top search for macroscopic dark matter. *Phys. Rev. D*, 100(10):103015, 2019.

[412] Pierre Sikivie. Invisible Axion Search Methods. *Rev. Mod. Phys.*, 93(1):015004, 2021.

[413] Hamish Silverwood and Richard Easther. Stellar Accelerations and the Galactic Gravitational Field. *Publ. Astron. Soc. Austral.*, 36:e038, 2019.

[414] Jagjit Singh Sidhu, Robert J. Scherrer, and Glenn Starkman. Death and serious injury from dark matter. *Phys. Lett. B*, 803:135300, 2020.

[415] D. P. Snowden-Ifft, E. S. Freeman, and P. B. Price. Limits on dark matter using ancient mica. *Phys. Rev. Lett.*, 74:4133–4136, May 1995.

[416] Daniel P. Snowden-Ifft and Andrew J. Westphal. Unique signature of dark matter in ancient mica. *Phys. Rev. Lett.*, 78:1628–1631, 1997.

[417] Catherine V Spaggiari. The jack hills greenstone belt, western australia: part 1: structural and tectonic evolution over¿ 1.5 ga. *Precambrian Research*, 155(3-4):204–228, 2007.

[418] Catherine V Spaggiari, Robert T Pidgeon, and Simon A Wilde. The jack hills greenstone belt, western australia: part 2: lithological relationships and implications for the deposition of 4.0 ga detrital zircons. *Precambrian Research*, 155(3-4):261–286, 2007.

[419] FS Spear and DA Wark. Cathodoluminescence imaging and titanium thermometry in metamorphic quartz. *Journal of Metamorphic Geology*, 27(3):187–205, 2009.

[420] D. Speller. Dark matter direct detection with SuperCDMS Soudan. *J. Phys. Conf. Ser.*, 606(1):012003, 2015.

[421] David N. Spergel. Motion of the earth and the detection of weakly interacting massive particles. *Phys. Rev. D*, 37:1353–1355, Mar 1988.

[422] David N. Spergel and Paul J. Steinhardt. Observational evidence for selfinteracting cold dark matter. *Phys. Rev. Lett.*, 84:3760–3763, 2000.

[423] M. Stevens-Kalceff. Cathodoluminescence microcharacterization of point defects in α-quartz. *Mineralogical Magazine - MINER MAG*, 73:585–605, 08 2009.

[424] Marion A Stevens-Kalceff. Cathodoluminescence microanalysis of silica and amorphized quartz. *Mineralogy and Petrology*, 107(3):455–469, 2013.

[425] Louis E Strigari. Neutrino coherent scattering rates at direct dark matter detectors. *New Journal of Physics*, 11(10):105011, Oct 2009.

[426] Vladimir Strokov and Emanuele Berti. Quasimonochromatic LISA Sources in the Frequency Domain. *arXiv e-prints*, page arXiv:2312.00121, November 2023.

[427] Vladimir Strokov, Giacomo Fragione, Kaze W. K. Wong, Thomas Helfer, and Emanuele Berti. Hunting for intermediate-mass black holes with LISA binary radial velocity measurements. *Phys. Rev. D*, 105(12):124048, 2022.

[428] Alexander O. Sushkov. Quantum Science and the Search for Axion Dark Matter. 4 2023.

[429] Nicholas D. Tailby, Daniele J. Cherniak, and E. Bruce Watson. Al diffusion in quartz. *American Mineralogist*, 103(6):839–847, 06 2018.

[430] Ryuichi Takahashi and Naoki Seto. Parameter estimation for galactic binaries by LISA. *Astrophys. J.*, 575:1030–1036, 2002.

[431] Ryuichi Takahashi and Naoki Seto. Parameter Estimation for Galactic Binaries by the Laser Interferometer Space Antenna. , 575(2):1030–1036, August 2002.

[432] Nicola Tamanini and Camilla Danielski. The gravitational-wave detection of exoplanets orbiting white dwarf binaries using LISA. *Nature Astron.*, 3(9):858–866, 2019.

[433] Nicola Tamanini, Antoine Klein, Camille Bonvin, Enrico Barausse, and Chiara Caprini. Peculiar acceleration of stellar-origin black hole binaries: Measurement and biases with LISA. *Phys. Rev. D*, 101(6):063002, 2020.

[434] M. Tanabashi et al. Review of particle physics. *Phys. Rev. D*, 98:030001, Aug 2018.

[435] Zhenxing Tang et al. SRF Cavity Searches for Dark Photon Dark Matter: First Scan Results. 5 2023.

[436] A. Tarun, S.J. Lee, C.M. Yap, K.D. Finkelstein, and D.S. Misra. Impact of impurities and crystal defects on the performance of cvd diamond detectors. *Diamond and Related Materials*, 63:169–174, 2016. 9th International Conference on New Diamond and Nano Carbons – NDNC 2015.

[437] J. M. Taylor, P. Cappellaro, L. Childress, L. Jiang, D. Budker, P. R. Hemmer, A. Yacoby, R. Walsworth, and M. D. Lukin. High-sensitivity diamond magnetometer with nanoscale resolution. *Nature Physics*, 4(10):810–816, Sep 2008.

[438] Sarah Thiele, Katelyn Breivik, Robyn E. Sanderson, and Rodrigo Luger. Applying the metallicity-dependent binary fraction to double white dwarf formation: Implications for lisa. *The Astrophysical Journal*, 945(2):162, mar 2023.

[439] M. Titze, H. Byeon, A. R. Flores, J. Henshaw, C. T. Harris, A. M. Mounce, and E. S. Bielejec. Towards Deterministic Creation of Single Photon Sources in Diamond using In-Situ Ion Counting. 12 2021.

[440] J. L. Tonry, L. Denneau, A. N. Heinze, B. Stalder, K. W. Smith, S. J. Smartt, C. W. Stubbs, H. J. Weiland, and A. Rest. ATLAS: A High-cadence All-sky Survey System. , 130(988):064505, June 2018.

[441] S. Toonen, M. Hollands, B. T. Gänsicke, and T. Boekholt. The binarity of the local white dwarf population. , 602:A16, June 2017.

[442] David M. Toyli, Charles F. de las Casas, David J. Christle, Viatcheslav V. Dobrovitski, and David D. Awschalom. Fluorescence thermometry enhanced by the quantum coherence of single spins in diamond. *Proceedings of the National Academy of Sciences*, 110(21):8417–8421, May 2013.

[443] Dustin Trail, Daniele J Cherniak, E Bruce Watson, T Mark Harrison, Benjamin P Weiss, and Ian Szumila. Li zoning in zircon as a potential geospeedometer and peak temperature indicator. *Contributions to Mineralogy and Petrology*, 171(3):25, 2016.

[444] Michelangelo Traina et al. Results on low-mass weakly interacting massive particles from a 11 kg d target exposure of DAMIC at SNOLAB. *PoS*, ICRC2021:539, 2021.

[445] M. Tse, Haocun Yu, N. Kijbunchoo, A. Fernandez-Galiana, P. Dupej, L. Barsotti, C. D. Blair, D. D. Brown, S. E. Dwyer, A. Effler, M. Evans, et al. Quantum-enhanced advanced ligo detectors in the era of gravitational-wave astronomy. *Phys. Rev. Lett.*, 123:231107, Dec 2019.

[446] D.J. Twitchen, C.S.J. Pickles, S.E. Coe, R.S. Sussmann, and C.E. Hall. Thermal conductivity measurements on cvd diamond. *Diamond and Related Materials*, 10(3):731–735, 2001. 11th European Conference on Diamond, Diamond-like Materials, Carbon Nanotubes, Nitrides and Silicon Carbide.

[447] Péter Udvarhelyi and Adam Gali. Ab initio spin-strain coupling parameters of divacancy qubits in silicon carbide. *Physical Review Applied*, 10(5), Nov 2018.

[448] Atsuhiro Umemoto, Tatsuhiro Naka, Andrey Alexandrov, and Masahiro Yoshimoto. Super-resolution plasmonic imaging microscopy for a submicron tracking emulsion detector. *PTEP*, 2019(6):063H02, 2019.

[449] T. S. A. Underwood, W. Sung, C. H. McFadden, S. J. McMahon, D. C. Hall, A. L. McNamara, H. Paganetti, G. O. Sawakuchi, and J. Schuemann. Comparing stochastic proton interactions simulated using topas-nbio to experimental data from fluorescent nuclear track detectors. *Physics in Medicine and Biology*, 62(8):3237–3249, Mar 2017.

[450] Henning Vahlbruch, Moritz Mehmet, Simon Chelkowski, Boris Hage, Alexander Franzen, Nico Lastzka, Stefan Goßler, Karsten Danzmann, and Roman Schnabel. Observation of squeezed light with 10-db quantum-noise reduction. *Phys. Rev. Lett.*, 100:033602, Jan 2008.

[451] S. E. Vahsen et al. CYGNUS: Feasibility of a nuclear recoil observatory with directional sensitivity to dark matter and neutrinos. 8 2020.

[452] S.E. Vahsen, H. Feng, M. Garcia-Sciveres, I. Jaegle, J. Kadyk, Y. Nguyen, M. Rosen, S. Ross, T. Thorpe, and J. Yamaoka. The directional dark matter detector (d3). *EAS Publications Series*, 53:43–50, 2012.

[453] Sven E. Vahsen, Ciaran A. J. O'Hare, and Dinesh Loomba. Directional Recoil Detection. *Ann. Rev. Nucl. Part. Sci.*, 71:189–224, 2021.

[454] Michele Vallisneri. Use and abuse of the Fisher information matrix in the assessment of gravitational-wave parameter-estimation prospects. *Phys. Rev. D*, 77:042001, 2008.

[455] O.V. Vasyukova, K. Goemann, V.S. Kamenetsky, C.M. MacRae, and N.C. Wilson. Cathodoluminescence properties of quartz eyes from porphyry-type deposits: Implications for the origin of quartz. *American Mineralogist*, 98(1):98–109, 01 2013.

[456] Milad Gholipour Vazimali and Sasan Fathpour. Applications of thin-film lithium niobate in nonlinear integrated photonics. *Advanced Photonics*, 4(3):034001–034001, 2022.

[457] Aditya Vijaykumar, Avinash Tiwari, Shasvath J. Kapadia, K. G. Arun, and Parameswaran Ajith. Waltzing Binaries: Probing the Line-of-sight Acceleration of Merging Compact Objects with Gravitational Waves. *Astrophys. J.*, 954(1):105, 2023.

[458] T. Wagg, F. S. Broekgaarden, S. E. de Mink, N. Frankel, L. A. C. van Son, and S. Justham. Gravitational Wave Sources in Our Galactic Backyard: Predictions for BHBH, BHNS, and NSNS Binaries Detectable with LISA. , 937(2):118, October 2022.

[459] Huiyi Wang, Alexander P. Stephan, Smadar Naoz, Bao-Minh Hoang, and Katelyn Breivik. Gravitational-wave Signatures from Compact Object Binaries in the Galactic Center. *Astrophys. J.*, 917(2):76, 2021.

[460] Jie-Shuang Wang, Fang-Kun Peng, Kinwah Wu, and Zi-Gao Dai. Pre-merger Electromagnetic Counterparts of Binary Compact Stars. , 868(1):19, November 2018.

[461] Junfeng Wang, Fupan Feng, Jian Zhang, Jihong Chen, Zhongcheng Zheng, Liping Guo, Wenlong Zhang, Xuerui Song, Guoping Guo, Lele Fan, Chongwen Zou, Liren Lou, Wei Zhu, and Guanzhong Wang. High-sensitivity temperature sensing using an implanted single nitrogen-vacancy center array in diamond. *Physical Review B*, 91(15):155404, Apr 2015.

[462] Zhenhai Wang, Lijiang Gui, Danhong Han, Zhuang Xu, Li Han, and Shengyong Xu. Measurement and evaluation of local surface temperature induced by irradiation of nanoscaled or microscaled electron beams. *Nanoscale research letters*, 14(1):1–11, 2019.

[463] Bertram Eugene Warren. *X-ray Diffraction*. Courier Corporation, Jan 1990. Google-Books-ID: wfLBhAbEYAsC.

[464] EB Watson, DJ Cherniak, JB Thomas, JM Hanchar, and R Wirth. Crystal surface integrity and diffusion measurements on earth and planetary materials. *Earth and Planetary Science Letters*, 450:346–354, 2016.

[465] Christopher Wegg and E. Sterl Phinney. White dwarf kinematics versus mass. , 426(1):427–439, October 2012.

[466] Steven Weinberg. A New Light Boson? *Phys. Rev. Lett.*, 40:223–226, 1978.

[467] RS Weis and TK Gaylord. Lithium niobate: Summary of physical properties and crystal structure. *Applied Physics A*, 37:191–203, 1985.

[468] Benjamin P. Weiss, Joseph L. Kirschvink, Franz J. Baudenbacher, Hojatollah Vali, Nick T. Peters, Francis A. Macdonald, and John P. Wikswo. A low temperature transfer of alh84001 from mars to earth. *Science*, 290(5492):791–795, 2000.

[469] Lawrence M. Widrow, Susan Gardner, Brian Yanny, Scott Dodelson, and Hsin-Yu Chen. Galactoseismology: Discovery of vertical waves in the galactic disk. *Astrophys. J. Lett.*, 750:L41, May 2012.

[470] Frank Wilczek. Problem of Strong P and T Invariance in the Presence of Instantons. *Phys. Rev. Lett.*, 40:279–282, 1978.

[471] D. Wildanger, B.R. Patton, H. Schill, L. Marseglia, J.P. Hadden, S. Knauer, A. Schönle, J.G. Rarity, J.L. O'Brien, S.W. Hell, and J.M. Smith. *Advanced Materials*, (44):OP309–OP313, 2012.

[472] Martijn J. C. Wilhelm, Valeriya Korol, Elena M. Rossi, and Elena D'Onghia. The Milky Way's bar structural properties from gravitational waves. , 500(4):4958–4971, January 2021.

[473] B. Willems, A. Vecchio, and V. Kalogera. Probing white dwarf interiors with LISA: periastron precession in eccentric double white dwarfs. *Phys. Rev. Lett.*, 100:041102, 2008. [Erratum: Phys.Rev.Lett. 101, 219903 (2008)].

[474] Mary EK Williams, Matthias Steinmetz, J Binney, Arnaud Siebert, Harry Enke, Benoit Famaey, Ivan Minchev, Roelof S De Jong, Corrado Boeche, Ken C Freeman, et al. The wobbly galaxy: kinematics north and south with rave red-clump giants. *Monthly Notices of the Royal Astronomical Society*, 436(1):101–121, 2013.

[475] James R. Wilson. Coherent neutrino scattering and stellar collapse. *Phys. Rev. Lett.*, 32:849–852, Apr 1974.

[476] R.P. Winarski, M.V. Holt, V. Rose, P. Fuesz, D. Carbaugh, C. Benson, D. Shu, D. Kline, G.B. Stephenson, I. McNulty, and J. Maser. A hard x-ray nanoprobe beamline for nanoscale microscopy. *Journal of Synchrotron Radiation*, 19(66):1056–1060, Nov 2012.

[477] Mark B. Wise and Yue Zhang. Yukawa Bound States of a Large Number of Fermions. *JHEP*, 02:023, 2015. [Erratum: JHEP 10, 165 (2015)].

[478] Thomas Wolf, Philipp Neumann, Kazuo Nakamura, Hitoshi Sumiya, Takeshi Ohshima, Junichi Isoya, and Jörg Wrachtrup. Subpicotesla diamond magnetometry. *Physical Review X*, 5(4), Oct 2015.

[479] G. Wolfowicz, S. J. Whiteley, and D. D. Awschalom. Electrometry by optical charge conversion of deep defects in 4h-sic. *Proceedings of the National Academy of Sciences*, 115(31):7879–7883, Jul 2018.

[480] Anna Wolz, Kent Yagi, Nick Anderson, and Andrew J. Taylor. Measuring Individual Masses of Binary White Dwarfs with Space-based Gravitational-wave Interferometers. *Mon. Not. Roy. Astron. Soc.*, 500(1):L52–L56, 2020.

[481] Kaze W. K. Wong, Vishal Baibhav, and Emanuele Berti. Binary radial velocity measurements with space-based gravitational-wave detectors. *Mon. Not. Roy. Astron. Soc.*, 488(4):5665–5670, 2019.

[482] Chris J.H. Wort and Richard S. Balmer. Diamond as an electronic material. *Materials Today*, 11(1):22–28, 2008.

[483] Yan Xu, Heidi Jo Newberg, Jeffrey L Carlin, Chao Liu, Licai Deng, Jing Li, Ralph Schönrich, and Brian Yanny. Rings and radial waves in the disk of the milky way. *The Astrophysical Journal*, 801(2):105, 2015.

[484] Zeyuan Xuan, Peng Peng, and Xian Chen. Degeneracy between mass and peculiar acceleration for the double white dwarfs in the LISA band. *Mon. Not. Roy. Astron. Soc.*, 502(3):4199–4209, 2021.

[485] Yu Xue, Ziliang Ruan, and Liu Liu. Electrode-free photonic electric field sensor on thin film lithium niobate with high sensitivity. *Opt. Lett.*, 47(8):2097–2100, Apr 2022.

[486] Xusan Yang, Yan-Kai Tzeng, Zhouyang Zhu, Zhihong Huang, Xuanze Chen, Yujia Liu, Huan-Cheng Chang, Lei Huang, Wen-Di Li, and Peng Xi. Sub-diffraction imaging of nitrogen-vacancy centers in diamond by stimulated emission depletion and structured illumination. *Rsc Advances*, 4(22):11305–11310, 2014.

[487] Xusan Yang, Hao Xie, Eric Alonas, Yujia Liu, Xuanze Chen, Philip J. Santangelo, Qiushi Ren, Peng Xi, and Dayong Jin. Mirror-enhanced super-resolution microscopy. *Light: Science & Applications*, 5(66):e16134–e16134, Jun 2016.

[488] Sophia Yi, Shu Yan Lau, Kent Yagi, and Phil Arras. Astrophysical Parameter Inference on Accreting White Dwarf Binaries using Gravitational Waves. 10 2023.

[489] Jianbo Yin, Zhenjun Tan, Hao Hong, Jinxiong Wu, Hongtao Yuan, Yujing Liu, Cheng Chen, Congwei Tan, Fengrui Yao, Tianran Li, et al. Ultrafast and highly sensitive infrared photodetectors based on two-dimensional oxyselenide crystals. *Nature communications*, 9(1):3311, 2018.

[490] Shenghua Yu and C. S. Jeffery. The influence of star formation history on the gravitational wave signal from close double degenerates in the thin disc. , 429(2):1602–1608, February 2013.

[491] Tien-Tien Yu. 2024 TASI Lectures: A Dark Matter Primer. 6 2025.

[492] Nicolas Yunes, M. Coleman Miller, and Jonathan Thornburg. The Effect of Massive Perturbers on Extreme Mass-Ratio Inspiral Waveforms. *Phys. Rev. D*, 83:044030, 2011.

[493] Jascha Zander, Christian Rembe, and Roman Schnabel. 10 dB interferometer enhancement by squeezing of photon shot noise with sub-femtometer resolution and eye-safe optical power. *Quantum Sci. Technol.*, 8(1):01LT01, 2023.

[494] G Zavattini, Federico Della Valle, A Ejlli, and G Ruoso. A polarisation modulation scheme for measuring vacuum magnetic birefringence with static fields. *The European Physical Journal C*, 76:1–5, 2016.

[495] Oleg Zgadzai, Lazar Shtirberg, Yaron Artzi, and Aharon Blank. Selective addressing and readout of optically detected electron spins. *EPL (Europhysics Letters)*, 117(1):10001, Jan 2017.

[496] H. Zhang, K. Arai, C. Belthangady, J.-C. Jaskula, and R. L. Walsworth. Selective addressing of solid-state spins at the nanoscale via magnetic resonance frequency encoding. *npj Quantum Information*, 3(11):1–8, Aug 2017.

[497] Gang Zhao, Yongheng Zhao, Yaoquan Chu, Yipeng Jing, and Licai Deng. LAMOST Spectral Survey. *arXiv e-prints*, page arXiv:1206.3569, June 2012.

[498] Huijie Zheng, Jingyan Xu, Geoffrey Z. Iwata, Till Lenz, Julia Michl, Boris Yavkin, Kazuo Nakamura, Hitoshi Sumiya, Takeshi Ohshima, Junichi Isoya, Jörg Wrachtrup, Arne Wickenbrock, and Dmitry Budker. Zero-field magnetometry based on nitrogen-vacancy ensembles in diamond. *Phys. Rev. Applied*, 11:064068, Jun 2019.

[499] James F. Ziegler, M. D. Ziegler, and J. P. Biersack. Srim - the stopping and range of ions in matter (2010). *Nuclear Instruments and Methods in Physics Research Section B: Beam Interactions with Materials and Atoms*, 268(11):1818–1823, Jun 2010.

[500] Florestan Ziem, Marwa Garsi, Helmut Fedder, and Jörg Wrachtrup. Quantitative nanoscale mri with a wide field of view. *Scientific reports*, 9(1):1–9, 2019.

[501] P.A. Zyla et al. Review of Particle Physics. *PTEP*, 2020(8):083C01, 2020.